Title
Probing Nanostructures for Photovoltaics: Using atomic force microscopy and other tools to characterize nanoscale materials for harvesting solar energy

Author
Zaniewski, Anna Monro

Publication Date
2012

Peer reviewed|Thesis/dissertation

Probing Nanostructures for Photovoltaics: Using atomic force microscopy and other tools to characterize nanoscale materials for harvesting solar energy

by

Anna Monro Zaniewski

A dissertation submitted in partial satisfaction of the

requirements for the degree of

Doctor of Philosophy

in

Physics

in the

Graduate Division

of the

University of California, Berkeley

Committee in charge:

Alex Zettl, Chair

Michael Crommie

Lydia Sohn

Fall 2012

Probing Nanostructures for Photovoltaics: Using atomic force microscopy and other tools to characterize nanoscale materials for harvesting solar energy

Anna Monro Zaniewski

Abstract

Probing Nanostructures for Photovoltaics: Using atomic force microscopy and other tools to characterize nanoscale materials for harvesting solar energy

by

Anna Monro Zaniewski

Doctor of Philosophy in Physics

University of California, Berkeley

Alex Zettl, Chair

The ability to make materials with nanoscale dimensions opens vast opportunities for creating custom materials with unique properties. The properties of materials on the nanoscale are distinct from their larger counterparts, and can be tuned in ways that are not otherwise possible. In this work, various nanoscale materials are synthesized and characterized, with an emphasis on materials with photovoltaics applications. Graphene, an atomically thin sheet of carbon, is combined with metal nanoparticles, and the electronic and optical properties of this material are studied. Heterostructured nanocrystals of CdS-Cu_2S are characterized as a potential solar cell active layer. Improvement of the performance of organic solar cells is achieved with the application of large electric fields. In all of these studies, the atomic force microscope is used to characterize the surface topography and electronic properties of these systems.

To the students - Gina and Gloria, and others, who refreshed my love of science,
to my family who always supported me
to my friends and my dear A.C.

Contents

List of Figures

List of Tables

Acknowledgments

I would like to thank the committee, and Alex Zettl for their guidance and insights.

The work in Chapter 2 was supported in part by the Director, Office of Energy Research, Materials Sciences and Engineering Division, of the US Department of Energy under contract No. DE-AC02-05CH11231, which provided for synthesis of the graphene membranes and SEM characterization, the National Science Foundation under grants DMR-1206512 and EEC-0832812 which provided for optical and AFM characterization, respectively, and the Office of Naval Research under Grant N00014-09-1066 which provided for nanoparticle deposition and lamination.

The work in Chapter 3 was supported in part by the Director, Office of Energy Research, Materials Sciences and Engineering Division, of the U.S. Department of Energy under Contract No. DE-AC02-05CH11231. Support for EFM instrumentation was provided by the National Science Foundation under Grant No. EEC-0832819. I thank S. M. Hughes for the HRTEM assistance, and Jessy Baker for CdS NRs and useful discussions.

The work in Chapter 4 was supported by the Director, Office of Energy Research, Office of Basic Energy Sciences, Materials Sciences and Engineering Division, of the U.S. Department of Energy under Contract No. DE-AC02-05CH11231. I thank David Okawa for useful discussions and technical assistance.

I would like to thank the NSF for a graduate fellowship.

Chapter 1

Introduction

With an energy density of 1000 W/m^2, sunlight is an attractive source of energy for humanity's increasing demands. Solar energy is abundant, renewable, and clean, compared to other energy sources. Current solar technology, however, comes at a cost that makes it economically unattractive. Hence, there is a great deal of interest in new materials and techniques to reduce the cost of solar energy generation.

In this work, various nanostructures are examined for applications in solar cells. Nanotechnology gives unprecedented control over material properties. Nanoscale metals couple strongly with light, and can be used to increase absorption in solar cells, allowing them to be thinner and more efficient. Additionally, nanostructured materials can act as the light absorbing and current rectifying layer in a solar cell, as is the case with Cu_2S-CdS heterostructured nanorods, discussed in chapter 3. Organic molecules are another nanoscaled material which can be used to build solar cells. These materials are low cost and easily scaled, but suffer from poor light absorption and transport. A technique to modify organic solar cells is discussed in chapter 4, and organic solar cells are combined with graphene and metal nanostructures in chapter 2.

In many of these studies, Atomic Force Microscopy (AFM) based techniques play a large role in characterization or modification of the nanoscale structures. The AFM is a versatile instrument capable of mapping nanoscale forces, local conductivity, and work function distributions, and even can be used as a tool for modifying materials.

1.1 Photovoltaics fundamentals

Photovoltaic cells are solid-state devices which absorb light and convert that light to usable electricity. When they are intended for use as solar energy collectors, they are also referred to as solar cells. Solar cells can be made of many semiconducting materials. At present, the dominant material for commercial solar cell production is silicon, due to its favorable band gap, ability to be easily doped and wide availability [46].

The power efficiency of a solar cell is defined by [46]:

$$\eta = \frac{\text{max power output}}{\text{sunlight power}} \tag{1.1}$$

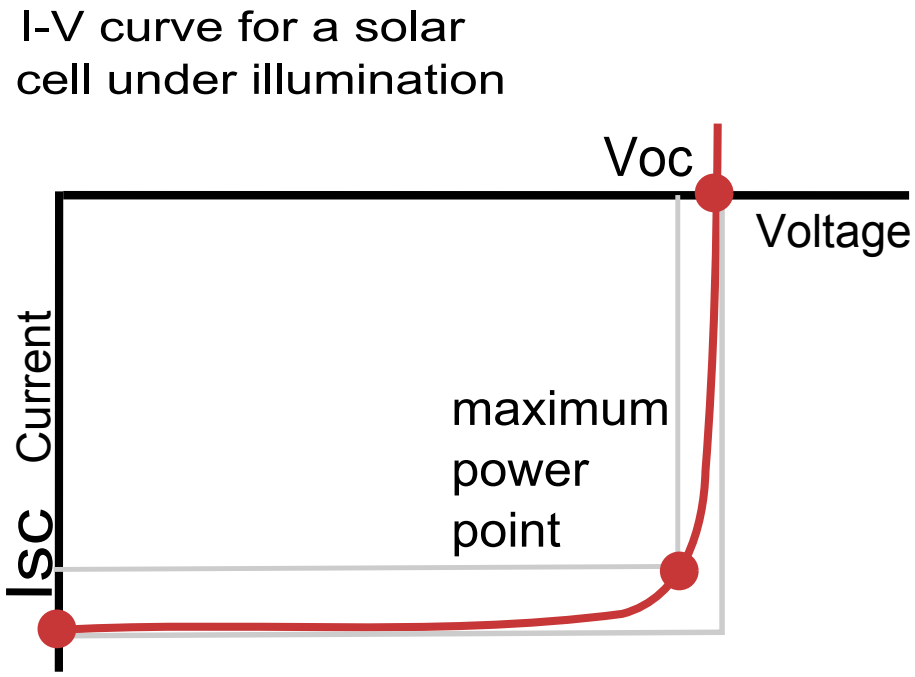

Figure 1.1: *An example of an I-V curve of a solar cell. As the applied voltage is swept over the working range of the solar cell, the current is monitored. The value of the current at zero applied voltage is called the short circuit current. The value of the voltage at which there is no current flowing through the cell is called the open circuit voltage. The ratio of the area of the two rectangles marked on this image is called the fill factor. One rectangle is defined by the current and voltage at the maximum power point, and the other is defined by the open circuit voltage and short circuit current. The fill factor is related to the diode ideality of the device, and plays a large role in device performance.*

Where "max power output" means the power output of the solar cell with the load managed such that the solar cell is operating optimally. This load dependence of the solar cell operation can be understood by considering the limiting cases of solar cell operation: in the case where the solar cell is shorted or left in an open circuit configuration the efficiency goes to zero. In the first case, there is no voltage difference between the terminals of the solar cell, so it can do no work. In the second case, there is no current. In between these two extremes, there is a maximum power output. This is the value used in equation 1.1.

How the solar cell performs under various loads is an important measurement of the solar cell. This is done by measuring the output current of an illuminated solar cell for various values of an applied voltage. This is equivalent to measuring the power output for various loads. The resulting curve is called an I-V curve, and it serves as a useful diagnostic. Figure 1.1 shows an example of this measurement, and how the important parameters of open circuit voltage (V_{OC}), short circuit current (I_{SC}) and fill factor (FF) are measured.

The efficiency in terms of the parameters V_{OC}, I_{SC} and FF is given by:

$$\eta = \frac{FFV_{OC}I_{SC}}{P_{in}} \tag{1.2}$$

Where P_{in} is the incident illumination power. The efficiency of solar cells is determined by the amount of light the solar cell can absorb, and the fraction of that absorbed light that is converted to usable electricity. The dominant mechanism for efficiency loss in nearly all solar cells is thermalization. A semiconductor can absorb light that has a greater energy than the bandgap of the semiconductor. However, any energy difference between the photon and the energy gap is lost to thermalization. Thus, there is the following trade-off. A material with a low band gap will absorb a large amount light, and output a high current. However, all the electrons will be extracted at the same low energy (less than or equal to the band gap). A material with a large band gap will absorb less light, but the electrons will each be extracted at a higher energy. These losses are called spectral losses, as they are due to the spectral mis-match between the solar cell and sunlight. Radiative recombination is another loss mechanism dictated by thermodynamics, and is equivalent to blackbody losses[46].

These two fundamental loss mechanisms set an upper limit on the efficiency of single gap solar cells. This upper limit is called the Shockley-Queisser limit [71]. For the solar spectrum, the ideal band gap size for a single-gap solar cell is 1.1eV, which would have an upper limit efficiency of 30 %. This limit can only be overcome by designing a device to absorb multiple bandgaps. This category of solar cells, called multijunction solar cells, have achieved efficiencies of up to 40.7%[37]. The production method for this type of cell involves many more steps than a single junction cell, and is prohibitively expensive for all applications except ones where space or weight are the primary concern, such as aerospace applications.

1.2 Light Management in Solar Cells for Enhanced Absorption

The above section dealt with the idealized case for solar cells: the assumption is that the cells absorb all above-gap light and that the only loss of current is due to radiative recombination. In this case, the thickness of the idealized solar cell is irrelevant. In real solar cells, however, the thickness affects the efficiency in two opposite directions. A thicker solar cell will absorb more light. For indirect gap semiconductors, such as silicon, this is especially important. In the opposite direction, a thinner solar cell will have fewer recombination events which reduce the output current. The best compromise between absorption and charge extraction would be to absorb light along the plane of the solar cell, and efficiently extract charges in the perpendicular direction. One way of redirecting the path of light is to add texturing to the surface. This is shown in figure 1.2. Texturing the surface can increase the total absorption in a solar cell by $2n^2$[82], where n is the index of refraction of the solar cell material. Briefly, this calculation includes the Planck formula for blackbody radiation intensity in a medium, which is n^2 greater than outside a medium. Additionally, randomizing the angle of the light path in the solar cell increases the intensity another two

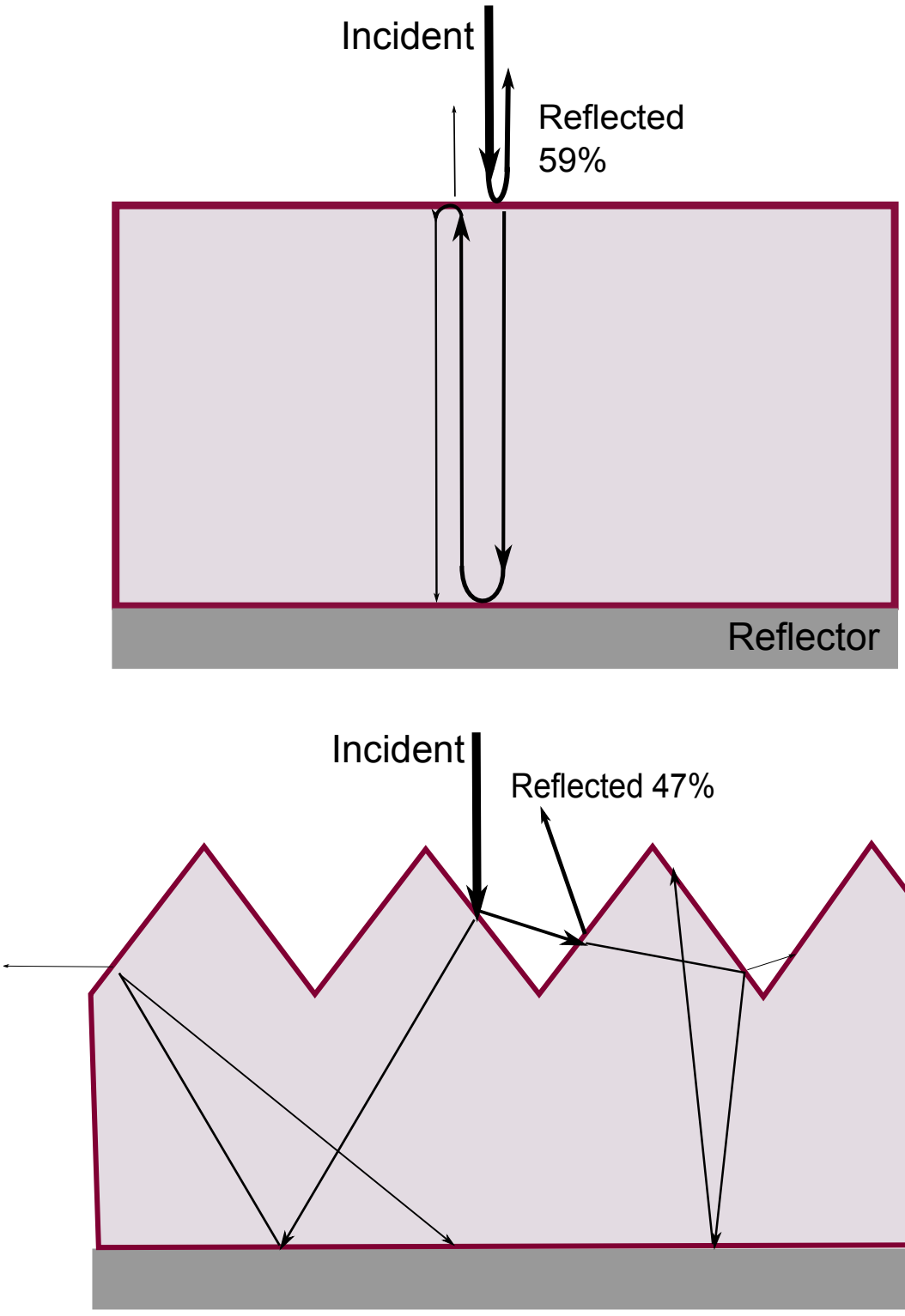

Figure 1.2: *Textured vs planar solar cells. Texturing of the surface of a solar cell increases the total amount of light available for absorption in a solar cell in three ways: reduced reflection at the surface due to multiple transmission opportunities; longer average optical path length within the active layer; and, reduced transmission losses after the first pass through the active layer due to steeper angles at the surface. Thus, the textured solar cell can be thinner than the planar one and achieve the same amount of light absorption. The diagram shown above is for silicon (n=3.96). The thickness of the arrows are proportional to the intensity of the light in each optical path. No absorption or anti-reflection layer is included in this illustration. The surface bisecting angle in the textured case is 36 °, corresponding to the geometry most commonly used in silicon solar cells. This geometry is determined by the silicon crystalline facets, and is easily produced through etching the*

times. If a reflecting backplane is added, then the total absorption enhancement is $4n^2$. For silicon, this enhancement is ~ 50.

Light trapping can thus have a dramatic effect on solar cell performance. Silicon, which is an indirect semiconductor, normally requires thick layers to absorb all incident light. However, with effective light trapping, the thickness of silicon solar cells can be reduced by 50 times without compromising absorption. Commercial silicon solar cells are typically about two hundred microns thick, and incorporate texturing for light trapping. Even with these thicknesses, light trapping is important to absorption, especially for near-gap light.

This classical picture of light trapping in solar cells is true for solar cell thicknesses greater than the wavelength of light, and does not consider nano-optics. In section 1.2.2, we show that nanoscale metal particles have interesting optical properties and how they can affect solar cell absorption beyond this picture.

1.2.1 Ideal Scattering Spectrum

Before engineering a scattering layer for solar cell efficiency enhancement, it is worthwhile to calculate the ideal scattering spectrum. Light with energy above the bandgap is thermalized, which leads to an increased operating temperature of the solar cell. The performance of solar cells tend to degrade with temperature, so one might suppose that there is a photon energy above which the thermal reduction in performance may reduce the overall energy extraction. With such a cutoff energy, it would be favorable to reflect light with energy above this cutoff. The following calculation shows that this is not the case, that absorbing light at all energies above the bandgap increase the efficiency. Energy balance equations were used to model the efficiency of the solar cell for various photon cutoff energies. The energy inputs to the solar cell are:

$$E_n = E_T + E_{sun} \tag{1.3}$$

where E_T is the blackbody radiation absorbed by the solar cell in a thermal bath at temperature T. E_{sun} is the energy absorbed from sunlight given the solar spectrum and assuming that light above the photon energy cutoff is reflected. The energy output of a solar cell is:

$$E_{out} = Work + E_{Radiated} \tag{1.4}$$

where $E_{Radiated}$ is the blackbody radiation of the solar cell as it thermalizes to a higher temperature, and the work is given by:

$$Work/t = FF * V_{OC} * I_{SC} \tag{1.5}$$

where FF is the fill-factor, related to the diode ideality, V_{OC} is the open circuit voltage, and I_{SC} is the short circuit current. The absorption is taken to follow a piece-wise defined function, that is, the absorption is 1 for $E_{BandGap} < h\nu < E_{Cutoff}$

The temperature dependence of the solar cell efficiency is dominated by a reduction in the open circuit voltage [46]. Higher temperatures increase intrinsic carrier concentration, reduce the bandgap due to thermal broadening, and increase recombination. The effect on the open circuit voltage, derived in [46]is taken to be:

$$V_{OC}(T) = \frac{1}{q}E_G(0) - \frac{kT}{q}ln(\frac{BT^\gamma}{I_{SC}}) \tag{1.6}$$

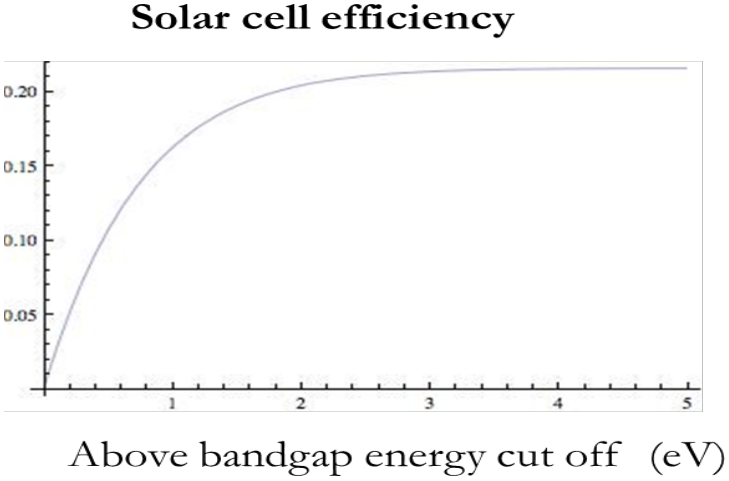

Figure 1.3: *Solar cell efficiency vs cut off absorption energy*

where γ and B are temperature-independent constants that are material specific. At non-extreme temperatures, the V_{OC} of crystalline silicon has a linear temperature dependence of -2.3 $mV/°$C, thus:

$$V_{OC} = V_{T=300} - 2.3\frac{mV}{K}T \tag{1.7}$$

The increase in temperature of the solar cell due to above-gap photons is:

$$\Delta T = \sum_{h\nu=E_{gap}}^{E_{Cutoff}} (h\nu - E_{gap})/C \tag{1.8}$$

Where C is the heat capacity of the material. The solar cell efficiency is calculated as:

$$\eta = \frac{Work}{E_{sun}} \tag{1.9}$$

Given the total energy input of the sun, and equation 1.5 and 1.7 to calculate the work at a temperature calculated with 1.8.

The calculation result is shown in Fig 1.3. As expected, for $E_{Cutoff} = E_{BandGap}$, when all the above bandgap light is reflected, the solar cell has zero efficiency. Interestingly, the efficiency increases monotonically with E_{Cutoff} indicating that it is favorable to absorb all energies of above gap light, despite the thermal effects. The calculated efficiency approaches known values for high efficiency silicon solar cells for high values of the E_{Cutoff}. In other words, the energy gained from high-energy photons outweighs the thermal reduction in efficiency. Thus, the ideal scattering spectrum would be as broad as possible, and increase absorption at all wavelengths. It should be noted that enhancing absorption near the band edge would be especially helpful.

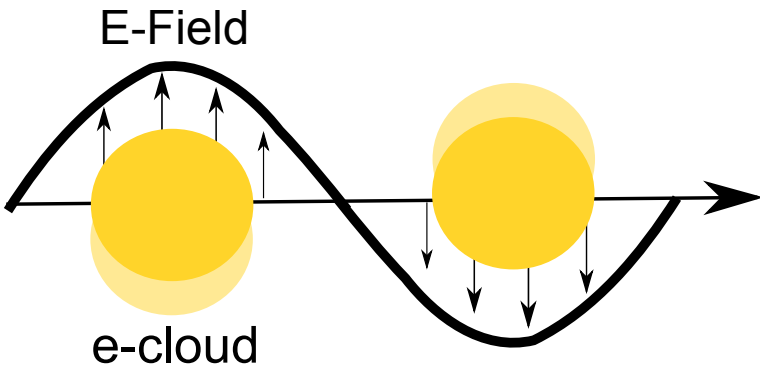

Figure 1.4: *The plasmonic effect in metal nanoparticles: the oscillating electric field from light displaces the electron cloud in the metal nanoparticle. The pull of the positive ions on the electron cloud acts as a restoring force. The electron cloud acts as a driven harmonic oscillator, and the polarization is largest for on-resonance frequencies of light.*

1.2.2 Optical properties of metallic nanoparticles

The electron cloud in a metal, when acted upon by an external electric field, will move counter to the field. If the field is turned off, a restoring force due to the ion lattice will pull the electron cloud in the opposite direction. Thus, electrons in a metal oscillate with the plasma frequency [31]:

$$\omega_p = \sqrt{\frac{n_e e^2}{m^* \epsilon_0}} \tag{1.10}$$

Where m* is the effective mass in the material. If the electric field is oscillating, such as with a propagating electromagnetic wave, when the frequency of the EM wave is less than the plasma frequency, the wave is reflected. When the frequency is greater than the plasma frequency, the wave is transmitted. The plasma frequency for metals tend to be in the ultraviolet region of the spectra, and thus, metals are shiny (reflecting) at visible frequencies.

When the dimensions of a metal are of the same order of magnitude or smaller than the wavelength of light, the optical properties of the metal change. Incoming light strongly polarizes the metal nanoparticles, which act as dipoles to strongly couple with on-resonance light, effectively acting as antennae to locally concentrate and scatter light. As an example, the scattering cross section of a polarized sphere of radius much smaller than the wavelength of light is [31]:

$$C_{scat} = \frac{1}{6\pi} \left(\frac{2\pi}{\lambda} \right)^4 |\alpha|^2 \tag{1.11}$$

Where α is the polarizability of the sphere, given by:

$$\alpha = 3V \left(\frac{\epsilon_p/\epsilon_m - 1}{\epsilon_p/\epsilon_m + 2} \right) \tag{1.12}$$

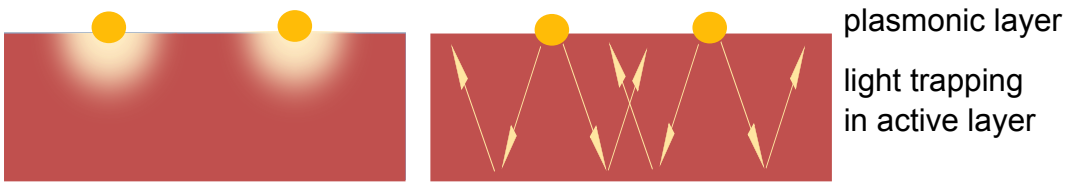

Figure 1.5: *Schematic of how the plasmonic resonance in metal nanoparticles translates into greater absorption in the solar cell active layer. both of the above processes are important. In the left process, the plasmonic resonance of the electron cloud has the effect of acting as an antenna to locally increase the field intensity, resulting in local enhancement of light absorption. In the process on the right, the polarized metal nanoparticles act as dipole scattering centers, which change the angle of light propagation. If the angle of propagation is greater than the condition for total internal reflection of the material, the light will be trapped within the solar cell until it is absorbed.*

Where ϵ_p and ϵ_m are the dielectric constants of the particle and embedding material, respectively. One can immediately see that when $\epsilon_p = -2\epsilon_m$ the polarizability of the sphere, and hence, its scattering cross section, becomes extremely large. This is called the Frohlich condition. This condition, for extreme scattering by nanoparticles, depends upon the dielectric constant. Since the dielectric constant for metals is highly dispersive, the scattering will be strongest at the frequency for which the dielectric function of the metal satisfies the Frohlich condition. Using the Drude model to approximate the dielectric function:

$$\epsilon(\omega) = 1 - \frac{\omega_p^2}{\omega^2 + i\gamma\omega} \tag{1.13}$$

and using free space as the embedding medium, one can find that the frequency of light which causes the Frohlich condition is:

$$\omega = \frac{\omega_p}{\sqrt{3}} \tag{1.14}$$

Thus, the critical frequency for light scattering is less than the bulk plasma frequency. For metals such as silver and gold, this frequency, called the plasmon frequency is in the visible region. Although bulk metals are simply reflective in the visible region, metals with nanoscale dimensions interact quite differently with light. This effect can be used to modify light pathways through solar cells and enhance their absorption, reducing materials costs and increasing efficiency.

1.2.3 Mie Scattering

For metal nanoparticles with a radius of the same order of magnitude as the wavelength of incident light, the above analysis is no longer valid. The nanoparticles studied in this work are in this regime. For these larger nanoparticles, Mie theory [50] describes the polarizability:

$$\alpha_{sphere} = \frac{1 - (1/10)(\epsilon + \epsilon_m)x^2 + O(x^4)}{(1/3 + \frac{\epsilon_m}{\epsilon - \epsilon_m}) - 1/30(\epsilon + 10\epsilon_m)x^2 - i\frac{4\pi^2\epsilon^{3/4}}{3}\frac{V}{\lambda_0} + O(x^4)}V \tag{1.15}$$

Where $x = \pi a/\lambda_0$.

This is the most sophisticated theory for finding the scattering of metal nanoparticles analytically. We can obtain some qualitative understanding from Mie theory to apply to solar applications:

1. The x^2 term is an effect of retardation of the field over the particle. Intuitively, a larger separation of charges reduces the restoring force, which lowers (redshifts) the frequency. For solar applications, we can use this shape dependence to tune the plasmon frequency.

2. The imaginary term is due to radiation damping caused by radiative decay of the electron oscillation. This has the effect of broadening the resonance. The radiation is at the plasmon excitation energy, or an energy reduced by Ohmic losses. The magnitude of the Ohmic losses depend on the conductivity of the metal species. For solar applications, the Ohmic losses constitute an overall energy loss only if the nanoparticles are radiating at energies below the bandgap. Otherwise, the broadening due to Ohmic losses can actually benefit the solar cell, by broadening the spectral response.

Thus, the factors that affect the scattering spectrum of metallic nanoparticles include the size of the particles, the local environment, and the metal type.

1.3 Organic Solar Cells

1.3.1 Organic solar cell materials

Organic solar cells are based on polymers or smaller carbon-based molecules. The main advantage of organic solar cells are their extreme low costs. The molecules which are used for organic solar cells are easy to produce on a large scale, and the device assembly is amenable to large production volumes. These two considerations mean that organic solar cells can be manufactured at costs much lower than conventional solar cells.

There are two basic kinds of organic solar cells: those which are polymer-based and can be solution processed, and those which are based on smaller molecules and typically must be deposited via an evaporation chamber. In this work we utilize solution processable materials. From a production standpoint, solution processing is preferable; and existing deposition methods for polymers can be used for this new class of photovoltaic polymers. Production-scale deposition techniques which have been successfully used for organic solar cell construction include ink jet printing[30], doctor blading[56], and silk screening[68]. In the laboratory, spin coating is the most convenient deposition method, and the method used in this work.These techniques are also compatible with a variety of substrates. In particular, organic solar cells can be constructed on flexible plastic films, resulting in completely flexible, lightweight solar cells. In addition to being a low cost production strategy, flexible substrates would greatly reduce the costs associated with installation[6]. After all, a large fraction of the installation costs for most solar systems is the bracketing required to hold heavy panels in place.

As is the case with most inorganic solar cells, organic solar cells are composed of an electron donating material and an electron accepting material. At this date, the most widely used organic solar cell materials are poly(3)hexylthiophene(P3HT) as the electron

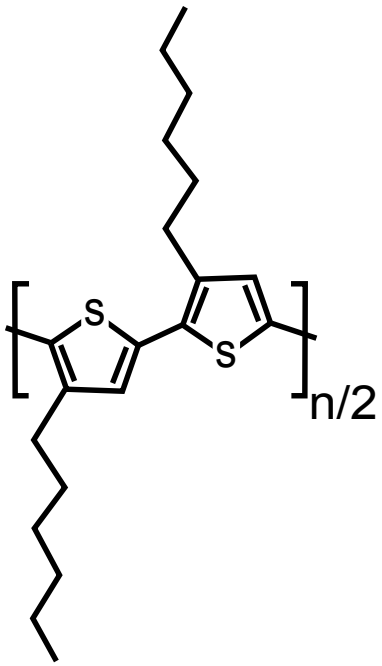

Figure 1.6: *Poly(3)hexylthiophene (P3HT), a commonly used polymer in organic solar cells. P3HT acts as the electron donating material. P3HT is responsible for most of the light absorption in organic solar cells. P3HT is soluble in many organic solvents, such as toluene and benzene.*

donator and [6,6]-phenyl-C61-butyric acid methyl ester (PCBM) as the electron acceptor. Figures 1.6 and 1.7 show the chemical structure of these molecules.

The internal structure of organics solar cells differs markedly from inorganic solar cells. Inorganic solar cells, such as silicon, are made by layering n-type silicon with p-type silicon (sometimes also with an intrinsic layer). Electron mobilities in silicon are high enough to allow this type of structure to be efficient; electrons can travel microns across the material without recombination with holes. Even more importantly, the exciton binding energy in silicon is low enough that the excitons can be thermally split, and electrons and holes can then move freely through the material. In organic solar cells, however, excitons have a high binding energy, and typically only be split at an interface. Furthermore, the exciton lifetime in organic solar cells is so low that excitons can only travel for ~ 10 nm before decaying, and the energy becomes lost to thermalization. Therefore, if the electron donating and accepting materials were simply layered on top of each other, only the light absorbed within ~ 10 nm of the interface would be extracted. Because of these differences, organic solar cells are constructed very differently- instead of a single interface between the two materials, the two materials are mixed together during deposition, forming a bulk heterojunction. See figure 1.8 for an illustration of the bilayer vs bulk heterojunction architectures.

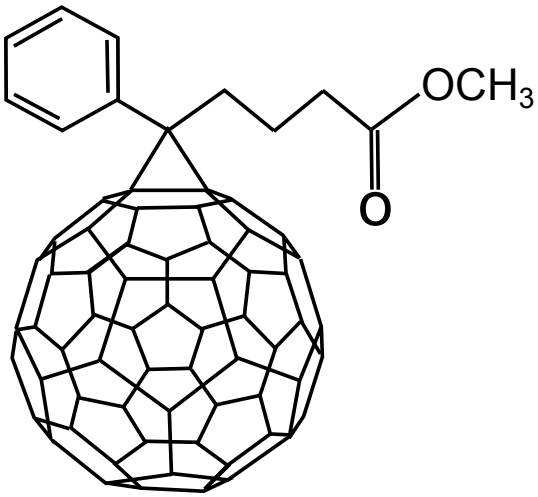

Figure 1.7: *[6,6]-phenyl-C61-butyric acid methyl ester (PCBM), a commonly used electron acceptor molecule for organic solar cells.*

1.3.2 Energy levels in organic solar cells

In crystals, such as silicon, bands exist because of the extended periodic nature of the crystals. In organic solar cells, molecular states have an analogous role to bands. There is an energy gap between the highest occupied molecular orbital (HOMO) and lowest unoccupied molecular orbital (LUMO). These levels have an important impact on the efficiency of organic solar cells. Light with energy below the HOMO-LUMO difference cannot be absorbed, and the relative positions between the energy states for the electron donor and acceptor impact the probability of exciton splitting.

Figure 1.9 shows a schematic of energy levels for materials involved in organic solar cells. The LUMO of the electron donor must be lower than the LUMO of the electron accepting material by at least the exciton binding energy. Typically, light is absorbed by the electron donor, generating an exciton. This exciton can diffuse along the polymer until it encounters an interface with the electron accepting material. If the energetics are right, the exciton will split, and the electron will jump to the acceptor. From there, the electron and hole diffuse through their respective materials until encountering the cathode or anode. The energy levels of the cathode and anode must be chosen so that the current is well rectified. For this reason, there are often blocking layers added between the electrodes and the active layer, to block charge carriers of one or another type.

1.4 Graphene

Since the discovery of single layer graphene, there has been a great deal of interest in this magnificent material. Graphene is a two-dimensional carbon-based material. It has a hexagonal lattice structure with sp2 carbon bonds. The carbon-carbon bond length is 0.14nm. The structure of graphene is shown in figure 1.10. Graphene is related to other carbon materials with sp2 bonding: graphite is a naturally occurring material which

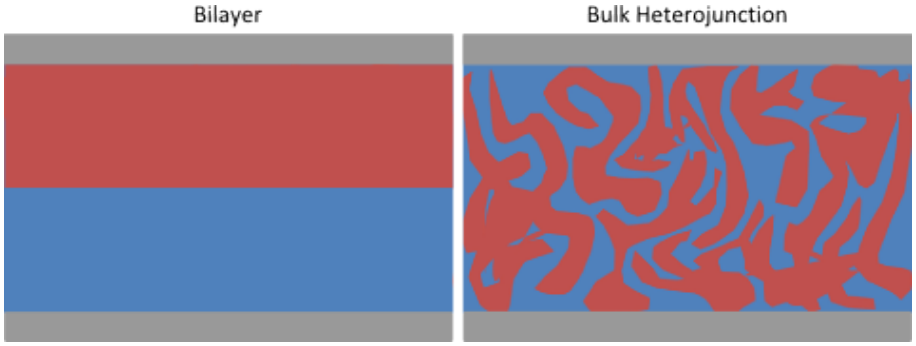

Figure 1.8: *Two examples of solar cell structures: bilayer and bulk heterojunction. The red and the blue represent n-type or p-type materials. Inorganic solar cells are often fabricated in the bilayer structure. Organic solar cells are fabricated as bulk heterojunctions. The advantage of the bulk heterojunction structure is that there is an interface between the n- and p- type materials throughout the structure. In organic solar cells, the excitons are strongly bound, and require an interface to dissociate; hence, organic solar cells are often produced as bulk heterojunctions.*

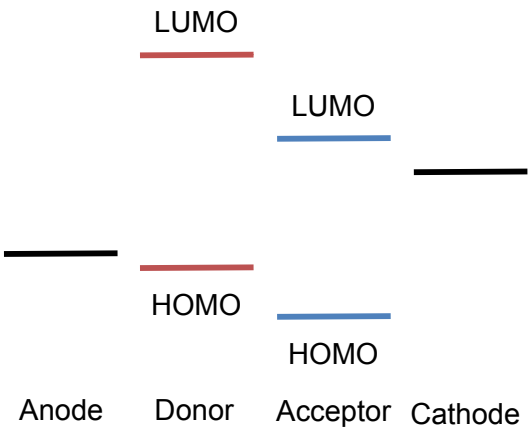

Figure 1.9: *Energy levels of organic solar cells. The highest occupied molecular orbital (HOMO) and lowest unoccupied molecular orbital (LUMO) have an analogous role to the conduction and valence band in photovoltaic crystals. The difference between the HOMO of the electron donor and the LUMO of the electron acceptor determines the upper limit of the V_{OC}. There must also be enough of an energy difference between the LUMO of the acceptor and the LUMO of the donor molecule to split the tightly bound exciton.*

resembles stacked graphene; carbon nanotubes resemble graphene which has been rolled into a tube shape; fullerenes resemble graphene folded into soccer ball shapes. Each of these materials have distinct and interesting physical properties.

Many of the unique attributes of graphene arise from its electronic structure. The energy dispersion of graphene is shown in figure 1.11 for energies near the Fermi energy. This is a remarkable electronic structure: the energy dispersion is linear near the Fermi energy, and the valence and conduction band touch with zero overlap. Thus, graphene is sometimes referred to as a 'zero gap' semiconductor. [23]

Because of this electronic structure, the density of states at the Fermi energy is zero; thus the Fermi energy can be easily shifted into the valence or conduction band, and graphene can be made n-type or p-type. Another consequence of graphene's electronic structure is graphene's optical properties. For light with $\sim$ 3eV or less, the linear nature of the energy bands dominate, and absorption for all these energies of light are equally probable, meaning that graphene has a flat absorption spectrum, and absorbs about 2% of incident light per layer.

Because of these features, graphene is widely studied [23], and the recent synthesis of large-area graphene[43] has demonstrated the scalability of graphene for use in consumer applications. There are a wide variety of potential applications for graphene. By geometric confinement to $\sim$ 10nm in one dimension, a band gap is opened, turning graphene into a semiconductor which could be used in diode applications [54] [7] [84]. Because of the aforementioned low density of states at the Fermi energy, the electronic transport of graphene is readily modified by chemical doping [45]. Graphene is also modified by the addition of nanoscale materials to the surface for chemical [25] optical or magnetic modification[81][19][60][39].

1.5 Atomic Force Microscopy

1.5.1 Basics of Atomic Force Microscopy and Imaging

The Atomic Force Microscope (AFM) is a versatile instrument capable of measuring nanoscale forces. A sharp tip at the end of a cantilever acts as a probe which is scanned line-by-line over a sample, as shown in figure 1.12. The interaction between the

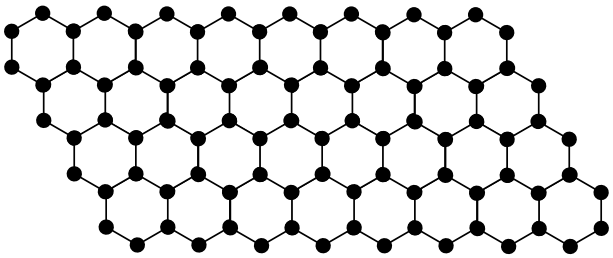

Figure 1.10: *The atomic structure of graphene. Graphene is a one-atom thick material made entirely of carbon. It is in the hexagonal structure, and has a carbon-carbon bond length of 0.14 nm.*

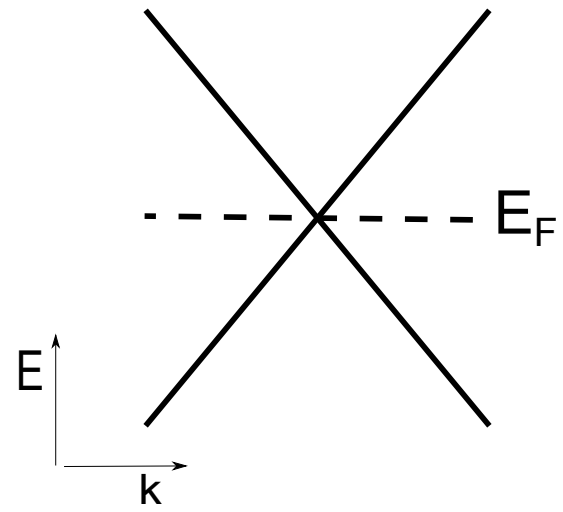

Figure 1.11: *The energy dispersion of graphene: near the Fermi energy, the energy bands are linear. This is called the Dirac cone.*

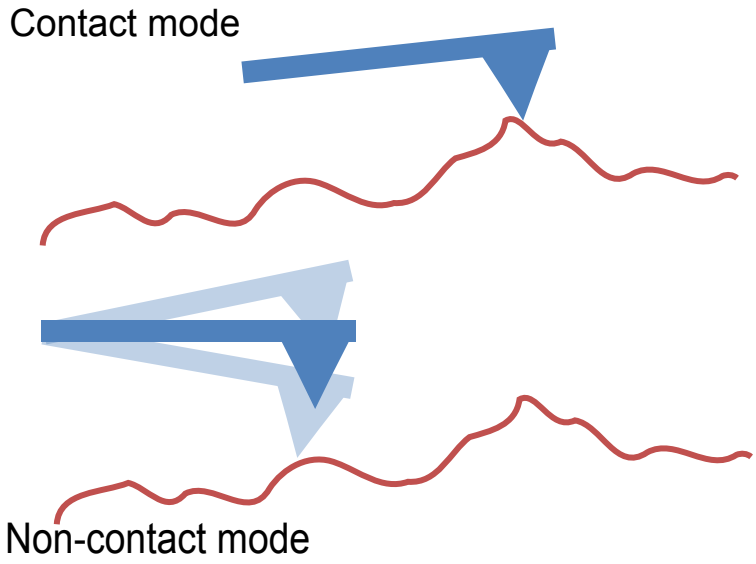

Figure 1.12: *A sharp tip at the end of a cantilever is used as a probe in the Atomic Force Microscope. In contact mode, the tip is dragged across the surface, and the deflection is used to measure the height of the surface. In non-contact mode, the probe is driven at close to its resonant frequency and scanned across the surface. The force on the probe is used to determine the surface height.*

surface of the sample and the sharp tip results in a force on the cantilever. In the most basic operation, the force is due to the van der Waals interaction, which is two uncharged atoms exerting a force on each other when in close proximity. The van der Waals interaction is well modeled by the Lennard-Jones potential:

$$V = 4\epsilon[(\sigma/r)^{12} - (\sigma/r)^{6}] \tag{1.16}$$

where ϵ is a constant that describes how strongly the two atomic species interact, and σ is the distance at which the interatomic potential is zero. Figure 1.13 shows a plot of the Lennard-Jones potential. As can be seen in the figure, for large distances, the interatomic force is attractive, and for short separations, the interatomic force is repulsive. The AFM can used in either regime; a feedback loop is used to modify the distance between the tip and the surface such that the force on the tip is constant. However, since the force is strongest in the repulsive regime, the greatest resolution is obtained in this regime. The distance at which the force is zero should be avoided.

The AFM can be used in either contact or non-contact mode. When the AFM is used in non-contact mode, the cantilever is driven at close to the resonant frequency, and its motion can be modeled as a simple harmonic oscillator. A frequency close to but less than the resonant frequency by $\sim 10\%$ is chosen to drive the cantilever. The force gradient of the cantilever is greater at this frequency than the resonant frequency, making the cantilever more sensitive. The drive of the cantilever can be more finely adjusted than the cantilever deflection, making non-contact AFM more sensitive, in general. In addition, non-contact mode is less likely to result in tip wear and contamination, which can distort imaging of the surface. For some soft samples, contact mode may damage the surface, giving further reason to prefer non-contact mode imaging. For these reasons, non-contact mode imaging is used in this work, with the exception of chapter 4, which uses contact mode to map electrical current through a sample.

1.5.2 Theory of Kelvin Probe Force Microscopy for Surface Potential Measurements

In chapter 2, Kelvin Probe Force Microscopy is used to measure the work function shift between unfilled graphene sandwiches and graphene sandwiches filled with gold nanoparticles. Monitoring the work function of samples has many other applications as well, and the technique is straightforward. The theory of this technique is introduced in this chapter, and a detailed users guide is included in Appendix B.

Figure 1.14 shows the origin of the electrostatic force which the AFM monitors. This electrostatic force is a result of a difference in work function between the probe and the sample[64]. In Figure 1.14a the probe and the sample are two unconnected materials with different work functions. Figure 1.14b shows the the result of connecting the sample and probe; charge flows between them until the Fermi energies align. In this example, the tip becomes negatively charged and the sample becomes positively charged. There is then an electrostatic force between the probe and the surface. In Figure 1.14c A feedback loop is used to zero the force on the probe, and restore the probe and sample to a neutral state by applying a voltage between probe and the sample. This is possible due to the extreme force

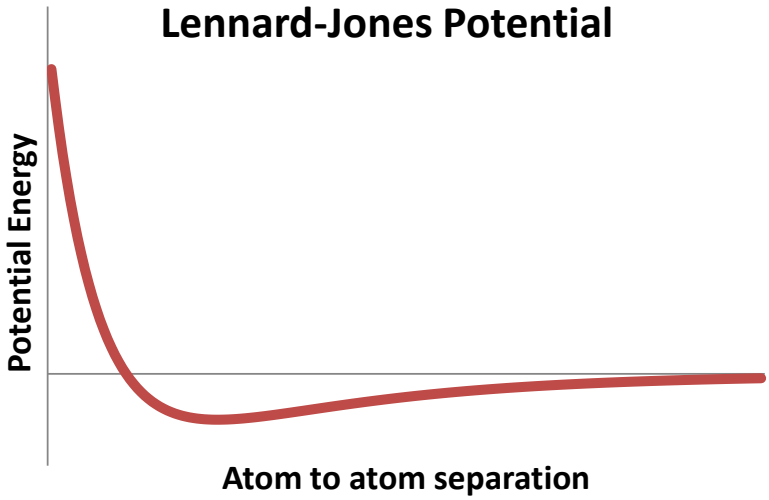

Figure 1.13: *The Lennard-Jones potential which describes the potential energy of two uncharged atoms as a function of atomic separation.*

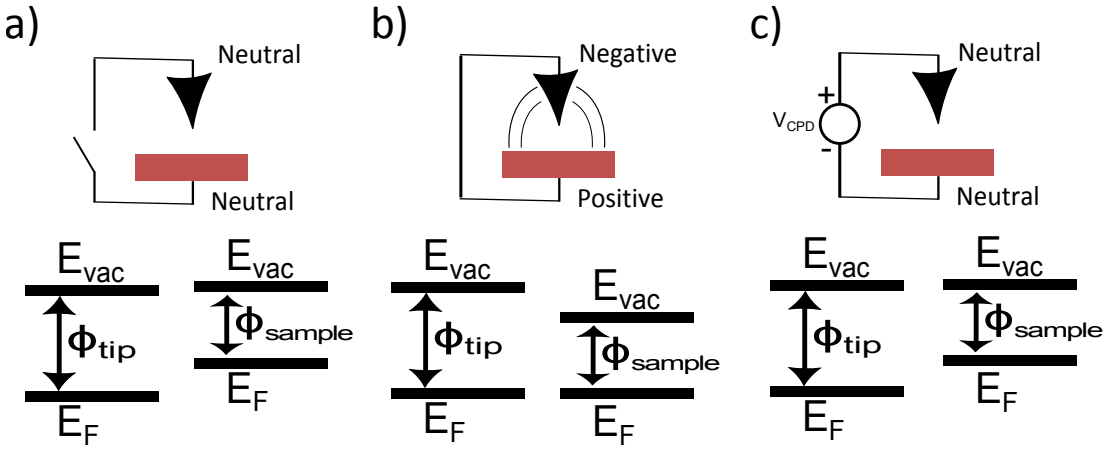

Figure 1.14: *The mechanism of Kelvin Probe Force Microscopy (KPFM). .*

sensitivity of the microscope. The KPFM measurement is typically done by alternating topography and KPFM scans. This enables the probe to be kept at a constant distance from the surface despite surface height variability. Thus, KPFM enables high-precision mapping of work function variability of a surface

1.5.3 Interpreting KPFM Results

The relationship between the measured contact potential difference with the AFM and the work function of the tip and the sample are given by:

$$CPD = \phi_{sample} - \phi_{tip} \tag{1.17}$$

Where ϕ_{sample} and ϕ_{tip} are the work function of the sample and tip, respectively. Thus, the work function of the tip must be known in order to determine the work function of the sample. Caution must be used, however, as the work function of the tip can drift due to tip wear or contamination. For that reason, relative shifts in surface potential are more reliable than attempts to measure the absolute value of the work function.

Sources of error in KPFM operation are discussed in more detail in Appendix B.

1.5.4 KPFM Operation Basics

Each line of the sample is scanned twice: in the first scan, the height profile of the sample is determined. The second scan, which Asylum calls a 'nap' scan, uses this height profile to hold the cantilever at a constant height above the sample. This is shown in figure 1.15.

In operation, an AC voltage signal is applied to the cantilever, at the resonant frequency of the cantilever, while the probe is scanning above the surface during the nap scan. If this signal were applied to a tip with the same work function as a conducting sample, the force between the tip and sample will always be attractive, due to the formation of image charges at the surface of the sample. This force will be at twice the resonant frequency of

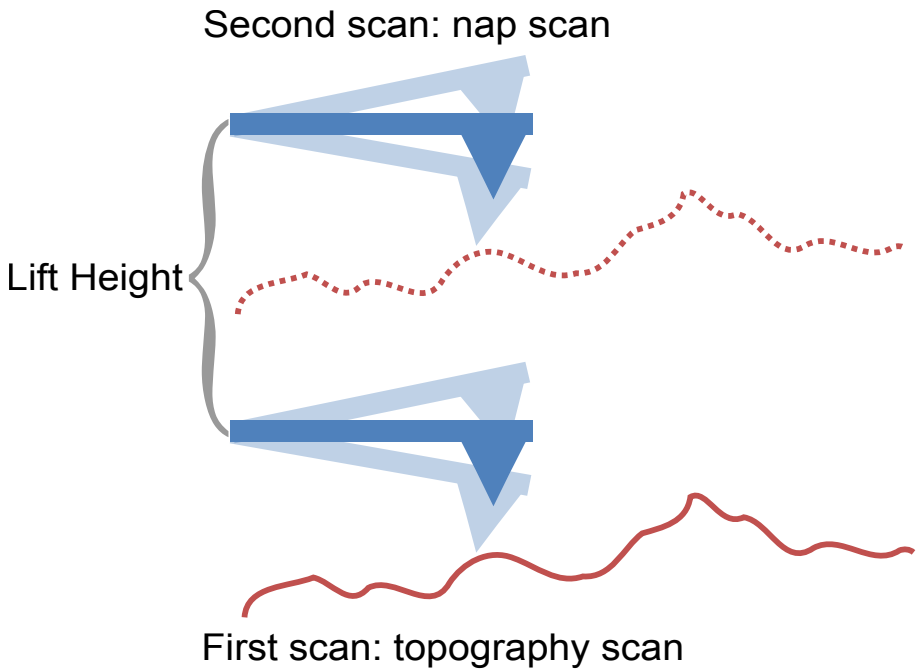

Figure 1.15: *The two-scan method which is used in KPFM and EFM measurements. In the first scan, a topography map of the surface is recorded. The second scan uses the height profile measurements to track the surface at a constant lift height above the surface.*

the cantilever, and the cantilever does not oscillate. If there is a work function difference between the tip and sample, this acts as a DC bias between the tip and the surface: in this case, the cantilever will oscillate. This can be understood by modeling the cantilever and sample as a parallel plate capacitor with an applied DC and AC voltage. The total energy of the capacitor is:

$$E = 1/2C[V]^2 \tag{1.18}$$

$$E = 1/2C[V_{DC} + V_{AC}sin(\omega_o t)]^2 \tag{1.19}$$

$$E = 1/2C[2V_{DC}V_{AC}sin(\omega_o t) - 1/2V_{AC}^2cos(2\omega_o t))] \tag{1.20}$$

Thus, only the cross terms with both a DC and AC component will produce a resonant force on the cantilever.

1.5.5 Electrostatic Force Microscopy and Kelvin Probe Force Microscopy: Similarities and Differences

Electrostatic Force Microscopy (EFM) is another technique which uses the AFM's force sensitivity to measure electrostatic forces. With EFM, the deflection of the cantilever due to the electrostatic force on the probe from the sample is measured. With KPFM, a voltage is applied to the probe to zero the electrostatic force. Thus, KPFM gives a direct measurement of the contact potential difference between the probe and the sample. EFM is a more sensitive technique, and more appropriate for nanoscale features and measuring

nanoscale charging. With detailed modeling, it is possible to use EFM to extract values for the surface potential, as is discussed in chapter 3, but this is a much more involved technique, as is described in that chapter.

Chapter 2

Optical and Electronic Properties of Metal Nanoparticle and Graphene Superstructures, and Their Use as Organic Solar Cell Electrodes

2.1 Introduction

In this experiment, we measure the electronic and optical properties of graphene and gold nanoparticle structures. The studied geometries include: single layer graphene, graphene with gold nanoparticles on the surface, and a sandwich of single layers of graphene with a gold nanoparticle filling. Figure 2.1.1 shows a schematic of the studied structures. In this chapter, we also describe various experimental methods for producing metal nanoparticles and the effect of the choice of nanoparticle fabrication on the optical properties of the nanoparticles. We demonstrate the use of these materials as an electrode for solar cells.

These graphene- metal nanoparticle structures have many interesting electronic and optical properties. Though laboratory grown graphene tends to be imperfect, with grain boundaries and cracks that arise during the transfer process, our proposed architecture reduces the spoiling of the electrode due to these imperfections. The sandwich structure offers a route to a low resistance electrode, as the metal nanoparticles provide conduits through imperfect graphene. We observe that the graphene sandwiches have nearly half the sheet resistance of single layer graphene with gold nanoparticles, which in turn is also roughly a factor of two lower than single layer graphene without gold nanoparticles.

As discussed in section 1.2.2, metal nanoparticles couple strongly with light due to a large polarization at resonant frequencies. The optical properties of metallic nanoparticles are also heavily influenced by their local environment. Incorporating the metal nanoparticles into a graphene sandwich results in a dramatic effect on the optical properties. In particular, the wavelength-dependent scattering cross section of gold nanoparticles is redshifted and

broadened. We discuss the optical measurements of graphene-metal nanoparticle structures, and compare the experimental results with theoretical modeling.

Our experiments also show that the presence of gold nanoparticles shifts the work function. This has important implications for solar cells: the open circuit voltage of solar cells can only be optimized with a finely-tuned work function for the anode and cathode.

Finally, graphene-metal nanoparticle-graphene sandwiches are used as electrodes for organic solar cells. Graphene based electrodes have a number of advantages for solar cells. They are carbon based, which is Earth abundant. Furthermore, the optical properties are favorable to solar cell enhancement. The thin nature of graphene (only one atom thick) allows for transference of near field amplification to the active layer. These effects should increase the light absorption in the active layer. The tunable nature of the work function is also a favorable feature of these electrodes. Hence, these sandwiches are a powerful material that could be used on a variety of solar cell designs.

2.1.1 Graphene and metal nanoparticles in the literature

The combination of metal nanoparticles with graphene is the subject of several recent studies [81][19][60][39]. One study shows that when assembled on top of single or few layered graphene, the plasmonic resonance of the nanoparticles redshifts with respect to metal nanoparticles without graphene[81]. In a related study, gated graphene with metal nanoparticles is shown to have a tunable plasmonic resonance[19]. Graphene can also be used as an encapsulent to protect silver nanoparticles against degradation[60], preserving their plasmonic properties.

In addition to modification of graphene by adding materials to the surface, graphene can be used to make sandwich structures. The sandwich structure is the nanoscale analogy of intercalating graphite with various materials to tune graphite's properties, which is a rich field of research [85][86][18]. More recently, some work has been done to investigate the properties of intercalated few-layer graphite and reduced graphene oxide [79] [72].

In a related approach, reduced graphene oxide layered with tin films has been shown to be a promising material for battery applications[33]. Recently, chemical vapor deposition (CVD) grown graphene sandwich structures have been demonstrated as a route to produce novel hybrid materials, and the structure and mass transport of such sandwich structures were investigated[83]. This method for making graphene sandwiches was recently used in conjunction with lithographically-defined nanoscale antennas to construct wavelength-specific photodetectors [21]. In this work, we explore the electronic and optical properties of an example of such a graphene sandwich structure: a graphene sandwich with a plasmonic nanoparticle filling.

We demonstrate the effect of the graphene structures on absorption in organic solar cells, though this electrode could also be used with other materials. We find that the absorption of solar cells fabricated with these sandwich structures is broadened compared to solar cells fabricated without the plasmonic layer.

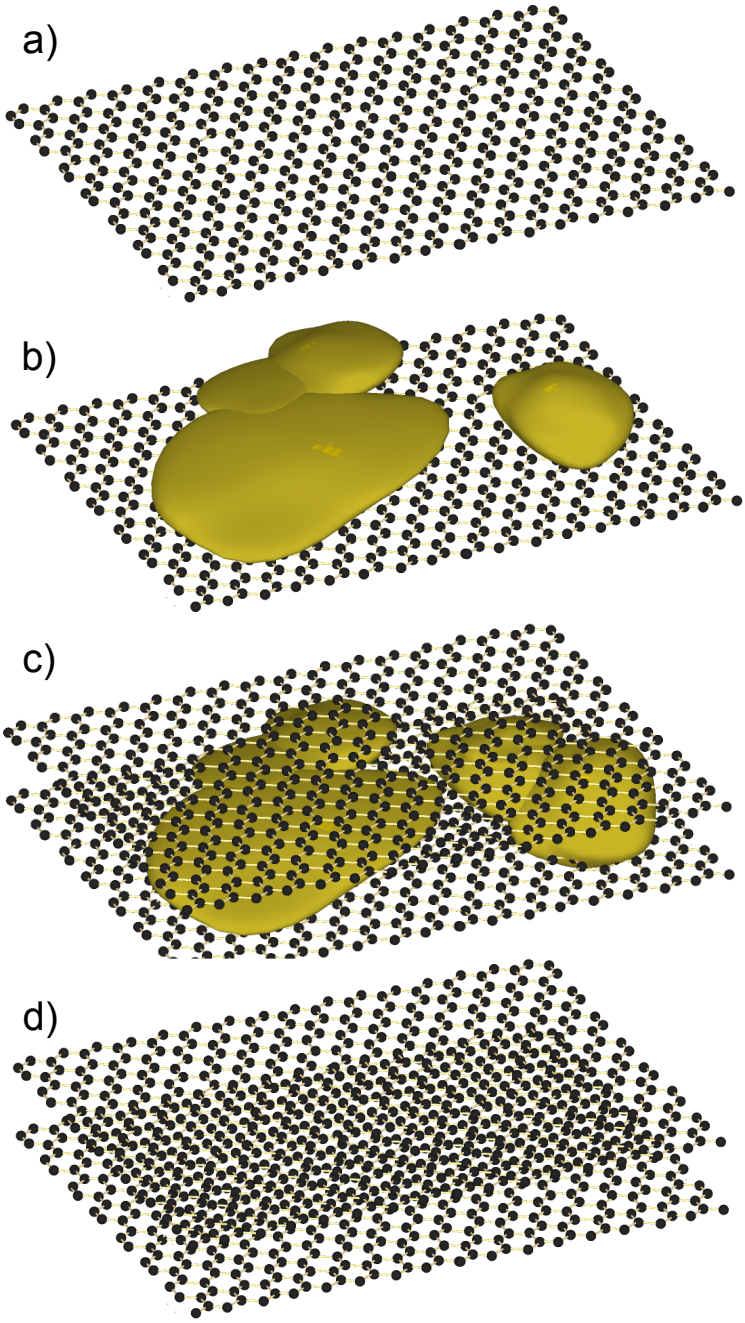

Figure 2.1: *Schematic representation of the graphene-based structures studied in this section: a) single layer graphene b) single layer graphene with gold nanoparticles c) graphene-gold nanoparticle-graphene sandwich d) unfilled double-layer graphene.*

2.2 Experimental methods for fabricating metal nanoparticles and achieving broadband scattering

One way of broadening the plasmonic response is to use nanoparticles with a range of sizes. Monodispersed nanoparticle sizes will have a sharp plasmonic response, whereas

nanoparticles with a substantial size distribution will show more broadband behavior. Two different large-scale nanoparticle production methods are attempted as part of this work to illustrate this difference: annealed metal films to produce nanoparticle islands, and nanoparticles defined using nanosphere lithography. One could also use electron beam lithography to define nanoscale patterns. Electron beam lithography method would have the advantage of having the finest control on the shape of the nanostructure. However, in practice electron beam lithography is a slow process for covering large areas, so is not considered for this work.

2.2.1 Nanosphere lithography

Nanosphere lithography is an inexpensive fabrication tool to pattern large areas with nanostructures [27]. In nanosphere lithography, a monolayer of polystyrene nanoscale spheres are assembled on a substrate. Next, a metal film is evaporated on the sample, and the spheres act as a mask. Only the spaces between the spheres are covered in the metal film. The spheres are then removed via solvent or mechanical exfoliation, and the metal film remains in the areas defined by the spaces between the spheres. Figure 2.2 shows a monolayer of such spheres and the result of using the nanospheres as a mask. The size of the resulting nanoparticles are fairly monodispersed, although imperfections in the sphere packing translate to size dispersion in the nanoparticles. Furthermore, the boundaries between nanosphere packing orientations produce extended linear features. The extinction spectrum for nanoparticles produced in this way is shown in Figure 2.4. The plasmonic response of these nanoparticles peak around 225nm, and is fairly sharp. In principle, the location of this peak could be tuned by choosing larger or smaller nanospheres. Using this technique, nanostructures from 20nm to 1000nm have been patterned[27].

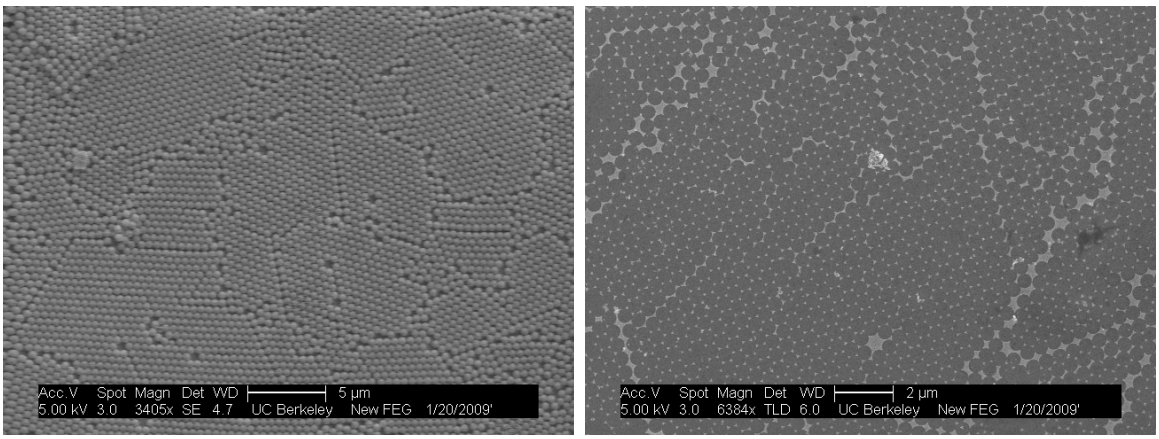

Figure 2.2: *Scanning electron microscope images of polystyrene nanospheres used in nanosphere lithography (left), and silver nanoparticles defined by nanosphere lithography (right). After coating the substrate with a monolayer of nanospheres, a metal film is evaporated on the sample. The spheres are then removed, and a metal film patterned in the voids of the spheres remains.*

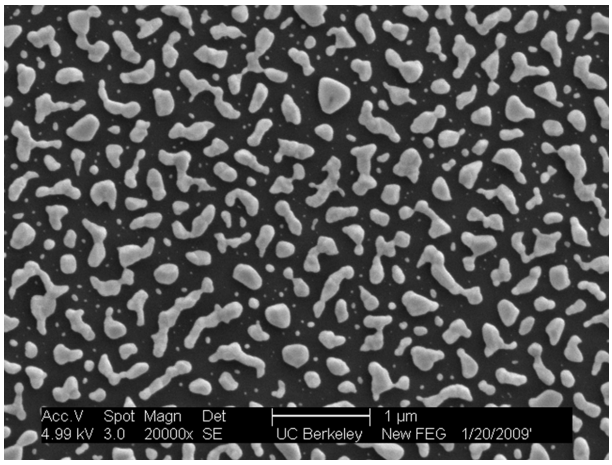

Figure 2.3: *Silver islands produced by evaporating a 16 nm thick film of silver onto a substrate (in this case, a silicon wafer). The film is then annealed in an oven in an inert environment at 300C. The thickness of the film can be adjusted to roughly control the size of the islands, though the islands always show significant size dispersion.*

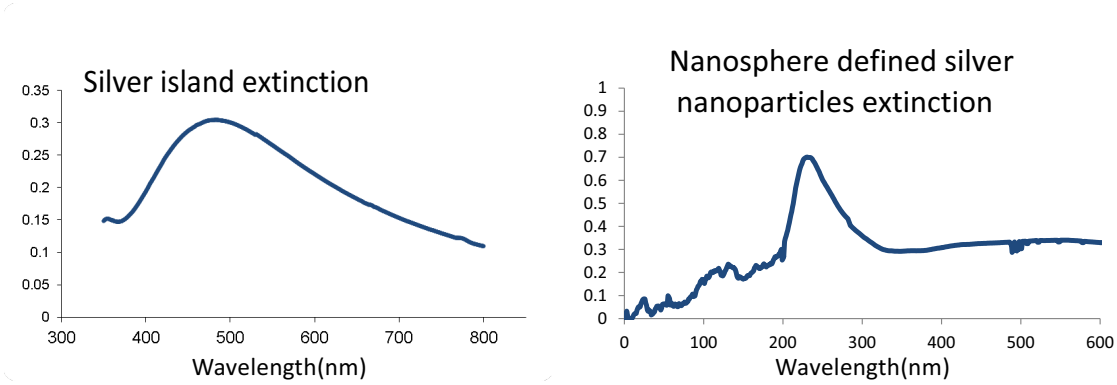

Figure 2.4: *Extinction spectrum of silver nanoparticles produced using the island method (left) and defined using nanosphere lithography (right). The plasmonic response of the patterned nanoparticles is much more well defined than the nanoparticles produced via the island method.*

2.2.2 Metal island formation by annealing thin films

The second fabrication method studied is self-assembly of metal islands. In this method, a thin film of metal (5 to 16 nm) is evaporated onto a substrate. The substrate is then annealed at 200 to 350 C, and the film dewets from the surface to form islands. The size of the islands is roughly controlled by the thickness of the film. However, in this case, there is a much broader distribution of nanoparticle sizes. This is reflected in the extinction spectrum shown in Figure 2.4. The plasmonic response of these nanoparticles peak around 475nm, and is much broader than the plasmonic response of the nanosphere-

defined particles. This technique works on a variety of substrates for both silver and gold, the most widely utilized plasmonic materials.

Because of the success of the island method for producing a broadly scattering plasmonic layer, it is the method chosen for the remainder of this work. Metal island fabrication also has the advantage of being an easily scalable technique.

2.3 Fabrication of graphene-metal nanoparticle sandwiches

Graphene and metal nanoparticle sandwiches are fabricated according to the following steps:

1. Grow CVD graphene on copper foil
2. Use PMMA method to transfer graphene to glass
3. Evaporate a thin film of silver (5nm) on graphene
4. Anneal sample at 350 C under Ar
5. Repeat graphene transfer onto glass/graphene/metal island sample.

2.3.1 Graphene growth and transfer

Large sheets of graphene are essential for making solar cells, which inherently are large-area devices. Of the various techniques for obtaining single-sheet graphene, chemical vapor deposition(CVD) is currently the most reliable and scalable, and thus, is the method used in this work. The CVD method is amenable to roll-to-roll processing, and has been demonstrated as a viable production technique for sheets up to 30 inches wide[1].

The method for single sheet graphene growth was developed by Ruoff[43], and is adapted for this work. In this method, a hydrocarbon source is introduced to a copper substrate at a high enough temperature to liberate the carbon from the hydrocarbon molecule. Copper is chosen for its low carbon solubility, which ensures that the carbon adsorbs on the surface of the copper and graphitizes. Because multiple sites on the copper surface simultaneously act as seed sites, CVD graphene is composed of variously oriented grains, a few microns in size[36].

In this work, the hydrocarbon source is chosen to be methane, for its wide availability and compatibility with the CVD oven setup. A two-stage graphene growth process is used to produce high quality graphene. In the two-stage process, a low methane flow is initially used to sparsely seed graphene growth on the surface of the copper foil. Next, a higher flow of methane ensures continuous coverage.

The growth recipe is as follows: copper foil is cut to shape and placed in the middle of a tube furnace. After establishing a vacuum of $\leq$ 15 mTorr, using a method of hydrogen flushing, the chamber is heated to 1020 C with 10 sccm of hydrogen gas flowing. The sample is annealed at this temperature and with the hydrogen gas for 40 minutes to ensure a clean surface. Next, 20 sccm of methane and 10 sccm of hydrogen are flowed over the copper for five minutes. The resulting pressure in the CVD chamber is 50-70 Torr. In

the next stage of growth, the methane flow rate is increased to 120 sccm for 5 minutes. The oven lid is then opened, and the sample allowed to cool under flowing hydrogen (10sccm) and methane (120sccm).

The result is monolayer graphene on the surface of the copper foil. The graphene is then transferred with the PMMA method[44]. The entire transfer process is illustrated in Figure 2.5. First, a thin film of PMMA is applied to the graphene coated copper by spin coating (2000 RPM), followed by annealing for 20 minutes at 150C on a hotplate. Next, the copper foil is etched away by floating the foil on a Na_2SO_8 solution (mixed 1:8 Na_2SO_8 powder: DI water by weight) for several hours. At this point, the copper is dissolved into the Na_2SO_8 solution, which turns blue. The thin PMMA/graphene film remains floating on the solution.

With care, the PMMA/graphene film can be picked up with a clean, flat piece of silicon wafer, by submerging the wafer and gently lifting the film out of the solution at approximately a 45deg. angle onto the wafer surface. To rinse the Na_2SO_8 from the PMMA/graphene film, the film can be transfered to a beaker of DI water. To do this, the wafer with the PMMA/graphene film can then be slowly submerged, also at a 45deg angle, into a beaker of DI water. The PMMA/graphene film will slide off the wafer, and onto the surface of the DI water. This process is similar to the one described by Ruoff [44].

The PMMA/graphene film is then picked out of the DI water onto the final device substrate. For the purposes of making solar cells, glass substrates are used. A drop of PMMA is added to the surface: this partially dissolves the PMMA film, and allows for a relaxation of the graphene, to achieve flatter films. Next, the sample is heated at 60C overnight. This allows for evaporation of the water through the graphene edges or cracks. Note, that when shorter time periods, such as 2 hours at 60C are tried, there is significantly less adhesion of the graphene to the substrate surface, indicating that the water had not yet evaporated.

The next step in the preparation of the samples is to remove the PMMA from the dried sample. To achieve this, a drop of PMMA is added to the dried sample, allowed to rest for 30 minutes, and then the sample is submerged in acetone for several hours to completely dissolve the PMMA. Attempts to speed the dissolution of PMMA by warming the acetone to 60C resulted in large areas of the graphene missing from the substrate, suggesting that the graphene ripped off with the PMMA. Removal at room temperature typically produced better performing samples.

Raman spectroscopy is used to characterize the graphene on glass; a Raman spectra taken with the 514 nm laser can be seen in Fig 2.6. The sample shows peaks at 1580 and 2700 cm-1 characteristic of graphene.

2.3.2 Modified transfer for flatness

Because the graphene sandwiches will ultimately be used as electrodes in solar cell devices, it is preferable that the films be flat, or at least, not have any features that would penetrate the active layer of the device and cause shorts. However, large folds in transfered graphene are common, and transferring a second layer of graphene on the first compounds the problem. To address this issue, modifications to the transfer process as described in detail by reference [75] are incorporated. The first modification is that instead of lifting the

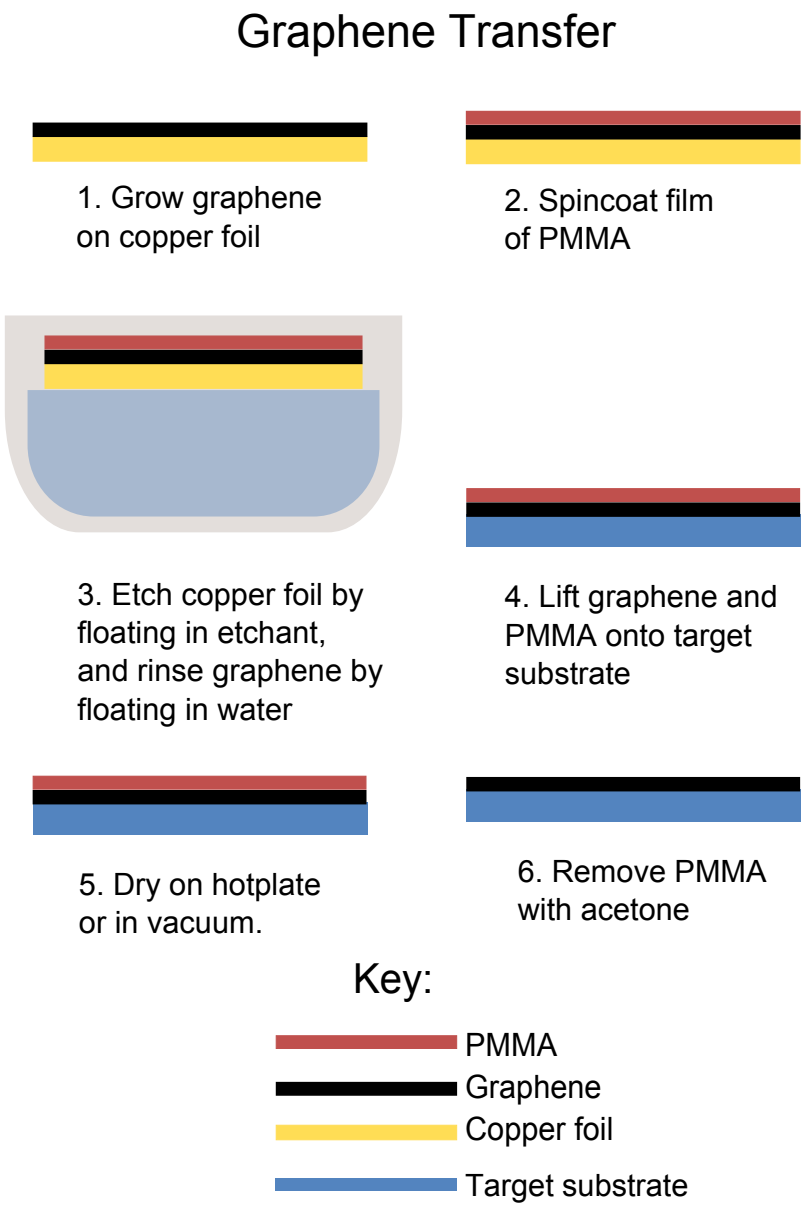

Figure 2.5: *The graphene transfer process. Graphene is first grown on copper foil via chemical vapor deposition, then a thin film of PMMA is spincoated onto the surface. Next, the copper foil is removed by floating the copper on an etch bath. The graphene is then rinsed by transferring the graphene/PMMA film onto a water bath. The graphene/PMMA film is then lifted out of the water bath and onto the target substrate. Next, the film is dried on a hotplate or in a vacuum for several hours. Next, the PMMA is removed with acetone.*

substrate out of the water bath to transfer the graphene to the final substrate, the substrate is submerged at a $\sim 30^{\circ}$ angle in the bath. The graphene, which is floating on the water bath, is positioned with the aid of a needle. Next, the water level is lowered by use of a

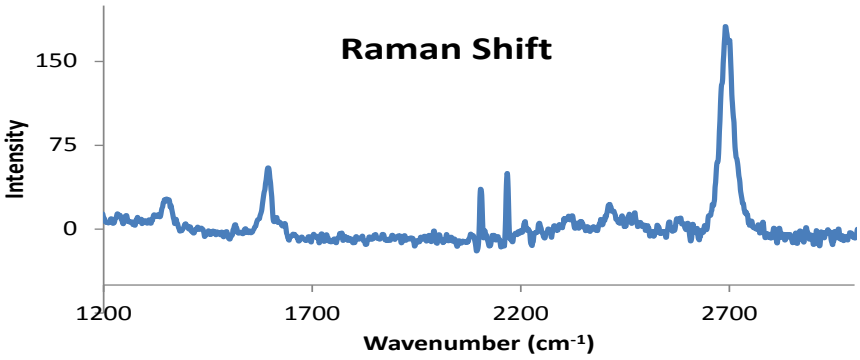

Figure 2.6: *Raman spectra measured with a 514nm laser of graphene showing charactaristic peaks at 1580 and 2700 cm^{-1}*

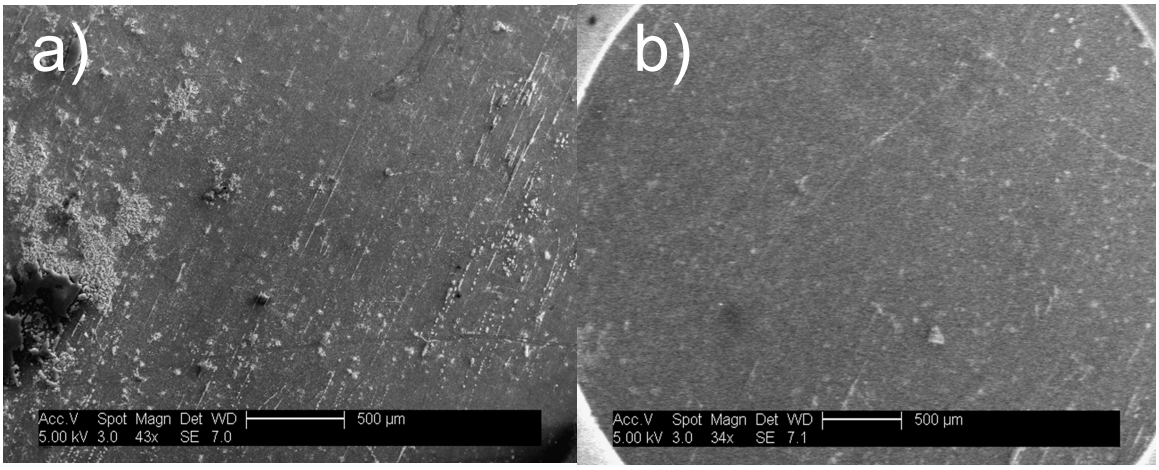

Figure 2.7: *SEM image of graphene transfered using a) the hotplate drying method and b) the vacuum drying method. Vacuum drying results in a much flatter film.*

pipette. Following the transfer onto the substrate, the graphene coated substrate is dried in a vacuum overnight, which replaces the step of drying on a hotplate for several hours. As with the original transfer process, a drop of wet PMMA is placed on the dried, transfered graphene to relax and dissolve the PMMA film prior to acetone removal.

The transfered films using these modifications are much more flat than with the hotplate method. The improved flatness is visible even to the unaided eye. Figure 2.7 shows the SEM images of graphene transferred using the two methods. AFM measurements show that large ($\geq$ 100nm in height) features are more common in the hotplate dried samples than with the vacuum dried samples; however, vacuum dried samples still show some tall features.

2.3.3 Graphene Sandwich Fabrication

For this work, gold islands are deposited on a graphene coated substrate via the method described in section 2.2.2. For this work, we use a film thickness of 5nm, and an anneal of 350 C for 90 minutes. The resulting islands are 50 to 200 nm across. SEM images of the gold islands on graphene are shown in Figure 2.8 and Figure 2.9. In most cases, the substrate is chosen to be glass or quartz.

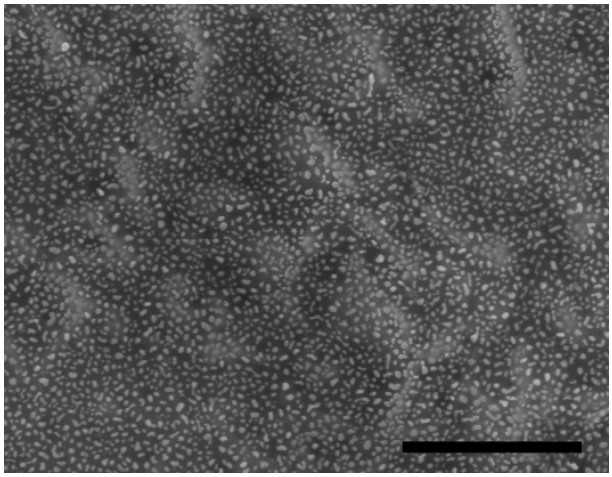

Figure 2.8: *Scanning electron microscope image of self-assembled gold nanoparticles grown on graphene. The nanoparticles are formed by evaporating a 5nm thick film of gold, followed by annealing at 350C. Sandwich structures are formed by transferring an additional layer of graphene over graphene/gold nanoparticle assemblies. Large area coverage is facile with this method. Scale bar is 2 μ m.*

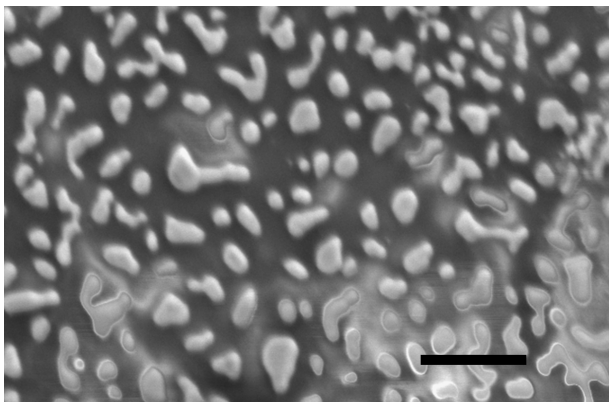

Figure 2.9: *Larger magnification image of the self-assembled gold nanoparticles. The gold nanoparticles are hundreds of nanometers across and within a micron of each other. The scale bar is 1 μm.*

We then add an additional layer of graphene using the same transfer method as for the first layer. A photograph showing a sample in three stages of the process (glass with

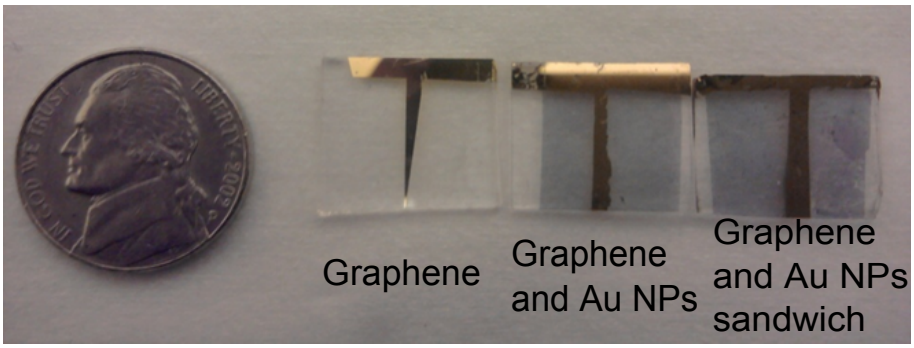

Figure 2.10: *Photograph of graphene, graphene and gold nanoparticles, and a graphene-gold nanoparticle-graphene sandwich on glass. The gold T is for contacting the graphene after constructing a solar cell on top of this glass/graphene substrate.*

graphene, glass with graphene and gold nanoparticles, and glass with the final sandwich) is shown in Figure 2.10. The change in optical properties of graphene with gold nanoparticles, and in the sandwich structure, are visible to the naked eye.

2.4 Optical Measurements of Graphene Sandwich Structures

Figure 2.11 shows the extinction (absorption and scattering) spectrum of a gold nanoparticle-graphene sandwich structure and a single layer of graphene with gold nanoparticles for comparison. The presence of a single sheet of graphene moderately redshifts the plasmon resonance peak, in agreement with prior literature[81]. The sandwich structure, however, shows a dramatically altered optical response. The extinction spectra is greatly red-shifted and broadened. This is likely due to enhanced coupling of the collective electron excitation within the gold nanoparticles to the graphene.

2.4.1 Comparison with Mie Theory

To investigate this hybridization effect in the case of graphene and gold nanoparticles, we use Mie theory [58] to compute the scattering cross section for a set of spherical gold nanoparticles with an average radius of 100 nm and a standard deviation in the radius of 50 nm, to reflect the size dispersion of our nanoparticles. We also perform the calculation including a 10 nm thick shell with graphene's optical constants (n=2.4, k=1.1)[55]. We note that this geometry (shown in the inset of Figure 2.12) differs from the geometry of the experiment, but serves as an interesting analogy.

This approach has the advantage of simplicity, and the effective parameters could be incorporated into other models without computational complications that arise when modeling structures with large variations in geometric length scales (eg, single atom vs 100 nm particles) as occurs with finite element or finite difference time domain approaches. The gold particles are modeled as having a radius of 100nm, with a standard deviation in the radius of 50nm, to approximate the size dispersion of the self-assembled particles.

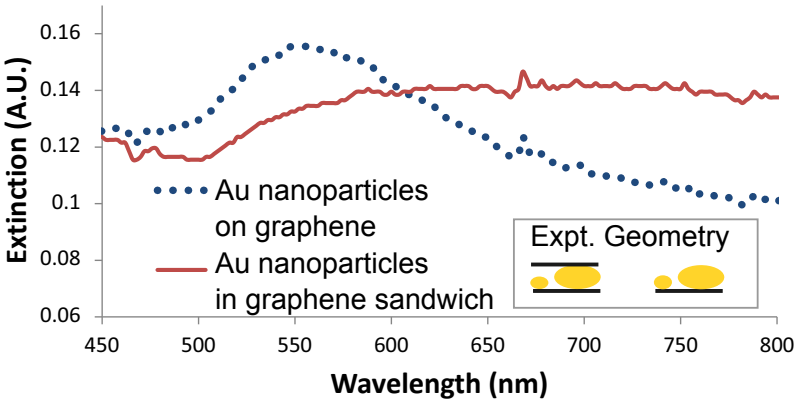

Figure 2.11: *Observed extinction spectrum of gold nanoparticles on a single layer of graphene and embedded in a graphene sandwich. The structures are assembled on a quartz substrate and measured with a UV-Vis spectrometer.*

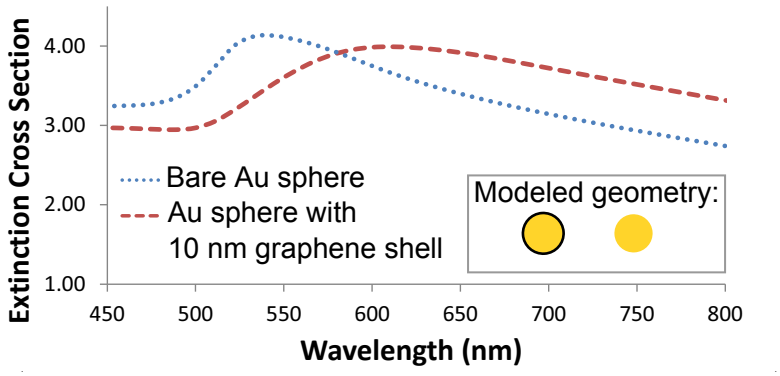

Figure 2.12: *Calculated extinction spectrum of gold spheres (100 nm diameter) with and without a graphene shell using Mie theory. The presence of a graphene shell redshifts and broadens the extinction spectrum, as observed. The extinction cross section values do not correspond to measured values, nor should they, but they show the general trend. Inset:Schematic of the simulated structures. Mie theory assumes spherical particles. In the Mie simulation, the particles had an average radius of 100nm, with a standard deviation in the radius of 50 nm. The calculations are performed for a variety of graphene shell thickness. For the simulation results shown above, the graphene shell thickness is 10 nm*

The results of the model are shown in Figure 2.12, and show that gold nanoparticles embedded in a shell of 10nm of "graphene" have a broadened and red-shifted optical response, which resembles the observed extinction spectra of the sandwich structure. These calculations are performed for a variety of graphene shell thicknesses, and we find that 10

nm thickness fits best to the observed extinction spectrum. For thinner shells, the extinction cross section spectrum is modified to a lesser extent.

These results indicate that the gold nanoparticles interact with a greater volume of graphene when embedded in the sandwich structure than when assembled on a single layer of graphene. The shell of graphene dampens the resonant action of the electron cloud, causing the observed shift in their optical properties.

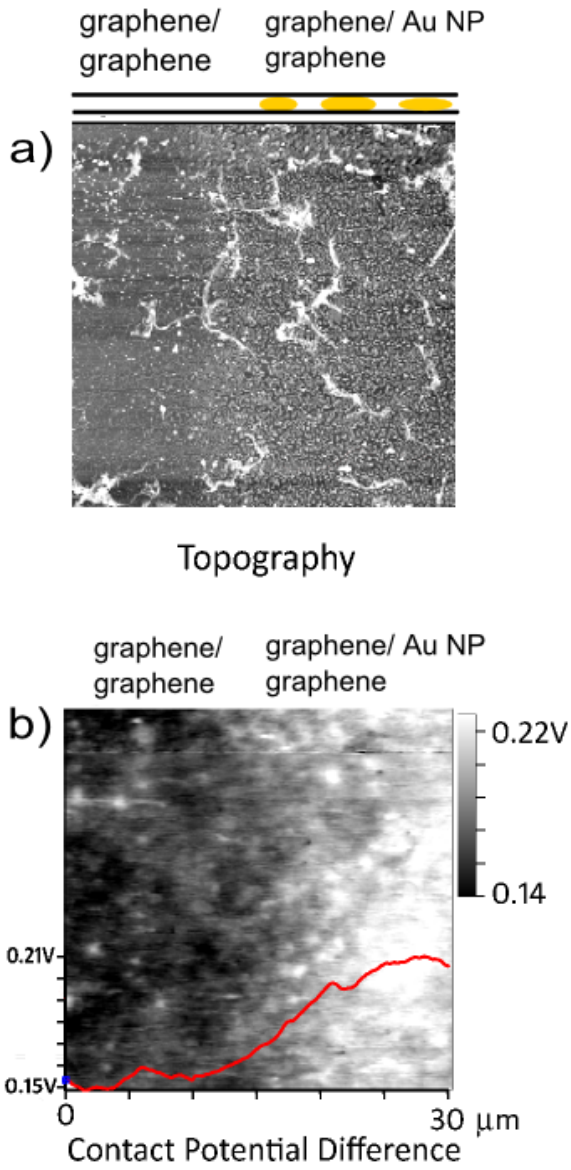

Figure 2.13: *Contact potential difference (CPD) measured with Kelvin Probe Force Microscopy over a 30 µm square scan. The fast scan direction is x, and the slow scan direction is y. A difference of 50mV in the contact potential difference between the regions with and without gold nanoparticles is observed, indicating a shift in work function.*

2.5 Measuring the work function shift due to sandwich filling

We also study the effect of metallic nanoparticles on the work function using Kelvin Probe Force Microscopy, as shown in Figure 2.13. Briefly, a conducting tip is electronically connected to the sample, and rastered at a constant height across the sample. A feedback loop zeros the voltage between the tip and the sample that arises from a difference in work function[64]. In this way, the local variation in surface potential, or the contact potential difference (CPD) can be monitored.

In order to reduce variations in CPD that can arise from variables such as tip wear, we examine the border region between an area containing gold nanoparticles embedded in graphene and a region with unfilled bilayer graphene, so that the two regions are probed in a single line scan. By comparing the average CPD in the two regions, we found that gold nanoparticles resulted in a local CPD of 50 mV over the bilayer graphene-only region. The red line in the bottom of Figure 2.13b shows a section graph averaged over the y- direction shows the trend of the CPD across the border region.

The tip work function is measured to be 4.4 eV, based on CPD measurements on a highly ordered pyrolytic graphite sample. Therefore, the work function of the unfilled bilayer graphene region is 4.55 eV, and the work function of the gold sandwich region is 4.60 eV. However, since KPFM is extremely sensitive to tip contamination or wear, which impacts the effective tip work function, the relative work function shift between the unfilled and filled sandwich, 50 meV, is more reliable than these absolute values.

More detail about the theory of KPFM is discussed in section 1.5.2 and a detailed user's guide is included in appendix B.

Previous studies have shown that single layer graphene doped with gold nanoparticles formed by reduced $AuCl_3$ has a work function shift of up to 500mV[70], and graphene with evaporated gold particles has a work function shift of 170mV [62]. The measured values in this work represent a smaller work function shift than these measurements of metal nanoparticles on single layer graphene. The top layer of graphene screens underlying materials[38], which would reduce the contribution of the nanoparticles to the work function. The local variability of the work function can be understood by considering the morphology: the sandwiches tend to form three-dimensional tent structures[83], producing a non-uniform graphene-nanoparticle separation, and this variability of graphene-metal separation can have a large impact on the work function modification of graphene[24]. Furthermore, due to the nature of the gold nanoparticles, a variation in crystallographic orientation would cause local variations in the surface potential. Despite these complications, a clear trend is evident at the border between regions with and without gold nanoparticles, evidencing a shift in the work function.

2.6 Sheet Resistance

The sheet resistance is also greatly affected by the structure type. The dc sheet resistance of as-grown graphene, graphene with gold nanoparticles, and graphene sandwiches is measured using the van der Pauw method. All samples are assembled on a glass substrate.

The sheet resistance of the as-grown graphene is measured to be 2300 $\Omega/\square$. Two

layers of graphene without a filling have a sheet resistance of 1200 $\Omega/\square$. The presence of gold nanoparticles on single layer graphene results in a sheet resistance of 1300 $\Omega/\square$, and the graphene-gold nanoparticle sandwich has the lowest sheet resistance, 730 $\Omega/\square$. For comparison, previous studies of multiple layers of CVD-grown graphene transferred to glass show that a single layer of graphene has a sheet resistance of 2100 $\Omega/\square$, and two sheets of graphene have a sheet resistance of 1000 $\Omega/\square$ [44].

There could be several mechanisms by which the sheet resistance of the graphene is reduced by the gold nanoparticles. One such mechanism is: the gold nanoparticles could act as parallel conduction channels connected in series with the graphene between the islands. The gold nanoparticles cover a large area of the graphene, and are typically separated by $\leq 1\mu m$, leading to frequent opportunities for parallel conduction. Since the equivalent resistance of any two resistors is always less than the constituent resistances, the overall resistance of the graphene sheet with gold islands would drop. Furthermore, since the gold islands are relatively large, they could bridge any gaps in the graphene common to the CVD growth and transfer process. These two mechanisms also explain the reduced sheet resistance of the sandwich compared to gold nanoparticles on single layer graphene. Finally, gold nanoparticles would shift the Fermi energy of the graphene, potentially introducing a higher charge density to the graphene sheets. These effects would all increase the sheet conductivity.

It is worth noting that the presence of gold nanoparticles on graphene might also have the effect of introducing scattering in the graphene, thereby reducing the electron mobility and hence the sheet conductivity; however, it appears that this is not a dominant mechanism in our samples.

2.7 Incorporation of graphene sandwiches with organic solar cells

2.7.1 Fabrication of control organic solar cells

Control organic solar cells are based on the most common solution-processed solar cell materials used at the present date: a P3HT:PCBM bulk heterojunction active layer with a PEDOT:PSS coated indium tin oxide (ITO) anode and LiF/Al cathode. This solar cell architecture has been extensively studied [26]. The energy level alignment is similar to that shown in Figure 1.9. Figure 2.14 shows the structure of these solar cells, both in the control case, and with the use of a plasmonic graphene sandwich as the transparent electrode.

Organic solar cells have the particular challenge of absorbing enough light in a film thin enough to extract all the charges. For example a film of 60nm thickness can only absorb about 60% of the light, but a thicker film would result in incomplete charge extraction [11]. Thus, increasing the amount of light absorbed in a thin layer would increase the efficiency.

Indium tin oxide (ITO) is a transparent conducting material, commonly used in displays, solar cells, and light emitting diodes. ITO coated glass substrates are purchased from Thin Film Devices, and are cleaned with ultrasonication for 10 minutes in soapy water, pure deionized water, and isoproponal alcohol. They are then dried with compressed

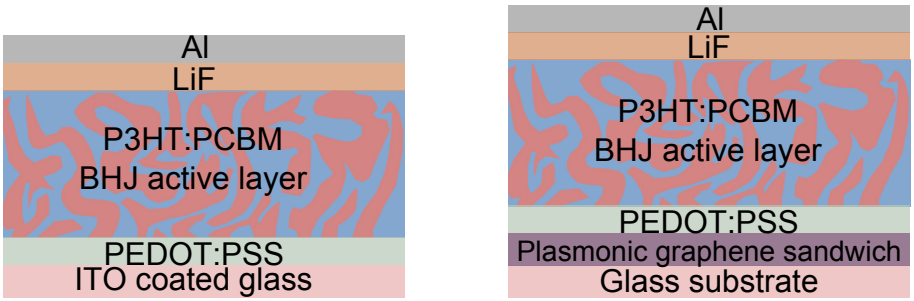

Figure 2.14: *Layers in the control organic solar cell (left) and the organic solar cell produced with the plasmonic graphene sandwich (right). In both cases, the active layer is a bulk heterojunction of P3HT:PCBM blend. Electron blocking layer PEDOT:PSS and hole blocking layer LiF are added to the anode and cathode sides, respectively. In the control device, indium tin oxide(ITO) is used as the transparent electrode. The devices are shown with the glass substrate on the bottom, as constructed. In use, the transparent substrate (ITO coated glass or plasmonic graphene sandwich on glass) would be oriented toward the light source.*

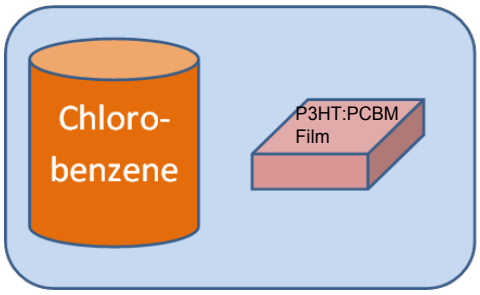

Figure 2.15: *The P3HT:PCBM film is left to dry in a closed vessel with an open source of chlorobenzene, creating an atmosphere with chlorobenzene vapor. This "solvent annealing" of the P3HT:PCBM film results in reproducible, high-quality films.*

nitrogen, and inspected for cleanliness.

Poly(3,4-ethylenedioxythiophene) poly(styrenesulfonate) , referred to hereafter as PEDOT:PSS, is conducting polymer blend commonly used in organic solar cell fabrication as an anode buffer layer. The PEDOT:PSS used in this study is purchased from Sigma-Aldrich and is filtered with a .8 μm filter, and spin coated onto the ITO substrates at 4000 RPM. The film is then dried on a hotplate in air at 150C for 10 minutes.

The PEDOT:PSS coated substrates are subsequently moved to an argon filled glove box for deposition of the active layer. 1:1 solutions of P3HT:PCBM are prepared by dissolving P3HT (Rieke metals) and PCBM (Sigma Aldrich) in di-chlorobenzene at 20 mg/ml concentration. Both solutions are left overnight to dissolve before use. The P3HT:PCBM solution is filtered through a .2 μm filter onto the PEDOT:PSS layer, and spun at 700 RPM for 5 minutes. The as-cast films are then dried overnight in the glove box inside a chamber with chlorobenzene vapor, shown schematically in Fig 2.15. Drying the films in this way greatly enhances the reproducibility of the devices, and in particular, the

Figure 2.16: *The effect of an inadvertent layer of AlOx on organic solar cell performance. Both cells are produced using similar fabrication steps, but the aluminum electrode in device (b) is deposited at a higher pressure (5 E -6 Torr vs 8E-7) and a slower evaporation rate (1 A/s vs 6 to 10 A/s) than the device in (a). The evaporation conditions in (b) resulted in an AlOx layer, which has a detrimental effect on electron extraction at the cathode, leading to poor fill factor and current.*

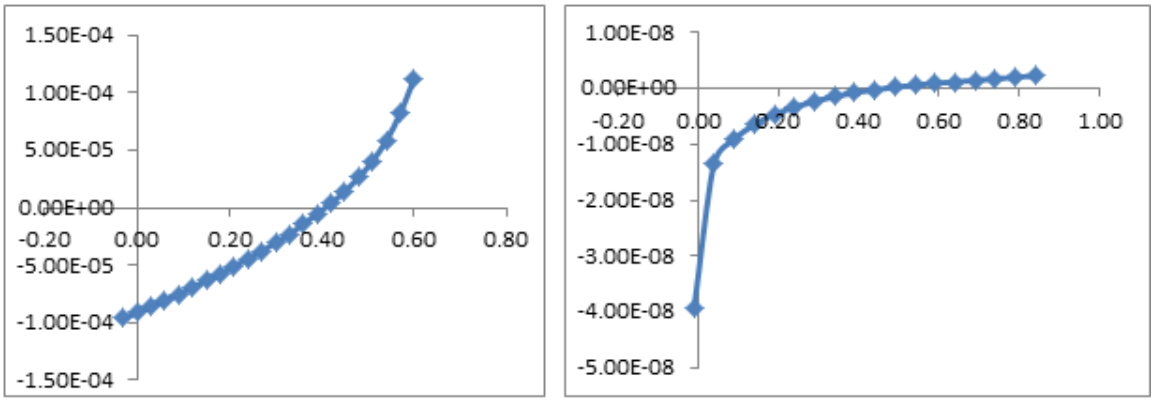

fill factor.[42]

After the active layer is dried, the cathode can be deposited. For the cathode, a thin film of LiF followed by aluminum results in the best devices, though functioning devices can be made without the LiF. The addition of LiF is beneficial for the open circuit voltage, and generally leads to higher efficiencies. To produce a lithium flouride target, LiF powder is compressed into pellets and sintered under a mixture of argon and hydrogen at 150C for 45 minutes. Evaporating LiF is relatively straightforward: it evaporates at very low currents in the e-beam evaporator.

Aluminum is chosen for its favorable energy level alignment.

When evaporating aluminum in the e-beam evaporator, extra care must be taken to prevent forming aluminum oxide. The presence of an AlOx layer has detrimental effects on the performance of the cells, as it results in a solar cell with a high series resistance and a poor fill factor, as shown in Fig 2.16.

To prevent the oxidation of aluminum, it is necessary to evaporate a small quantity of aluminum from the crucible with the shutter covering the crucible, and then wait approximately 2 hours for the vacuum to reach $\leq$ 8E-7 Torr before evaporating the aluminum. Evaporating at relatively high rates of 6-10 A/s results in better performing films than slower evaporation rates. In fact, in one trial of rates below 1 A/s, the film appeared to be largely AlOx. Though the crystal monitor registered 45 nm of Al, the resulting film is transparent. On the contrary, evaporation of 45 nm of Al at a higher rate results in high performing, uniformly shiny films. Evaporation of aluminum is typically unstable, hence a range of values is given. Though 45 nm of aluminum is sufficient to produce a working device, 100nm of aluminum makes a better performing electrode.

2.7.2 Optical absorption of solar cells with and without plasmonic graphene sandwiches

The main goal of the plasmonic graphene layer is to increase the amount of absorption in the solar cell active layer. A P3HT:PCBM layer is deposited on a single layer of graphene, a graphene and gold nanoparticle layer, and a graphene-gold nanoparticle sandwich, all on quartz. Quartz is chosen for its low levels of absorption throughout the visible and near-UV spectrum. The results are shown in Figure 2.17.

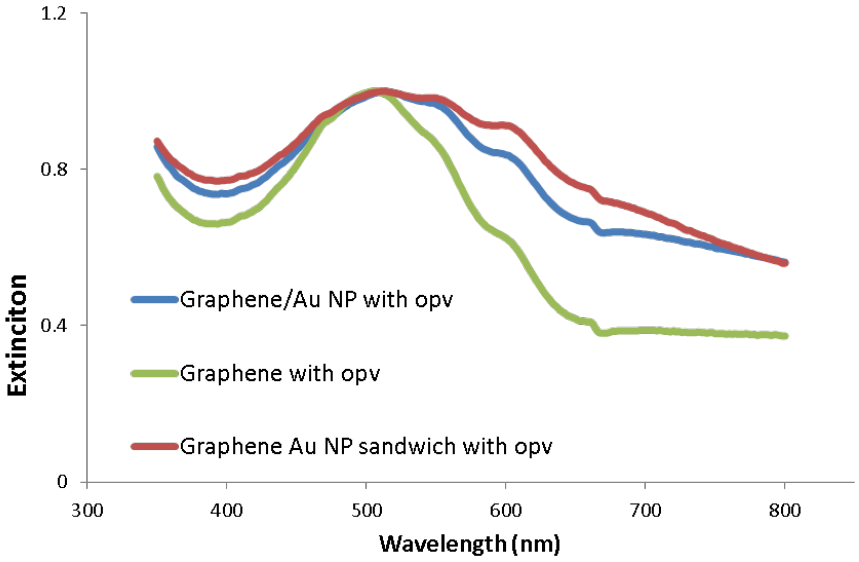

Figure 2.17: *The optical extinction of organic solar cell films with graphene, graphene and gold nanoparticles, and a graphene-gold nanoparticle-graphene sandwich. The films produced with the sandwich had broader absorption than the other films, particularly in the lower energy wavelengths.*

2.7.3 Performance of organic solar cells with graphene sandwich electrode

A current vs voltage test is used to characterize the performance of cells produced with the various graphene structures. An I-V plot of the organic solar cell fabricated with a graphene -gold nanoparticle-graphene sandwich is shown in Figure 2.18. The I-V curve is taken under illumination with an AM1.5 solar simulator lamp with an intensity of 100mW/cm^2. A discussion of I-V curves can be found in section 1.1.

Solar cells constructed with the other graphene geometries are also tested with the same solar simulator set up. Current vs voltage measurements are taken for each cell, and the findings are summarized in table 2.1. Solar cells produced with a single layer of graphene as the electrode suffer from low short circuit currents. This is indicative of poor series resistance of the cell, likely caused by the poor conductivity of a single layer of graphene. Cells produced with a single layer of graphene and gold nanoparticles have slightly improved open circuit voltage and short circuit current. Solar cells produced with

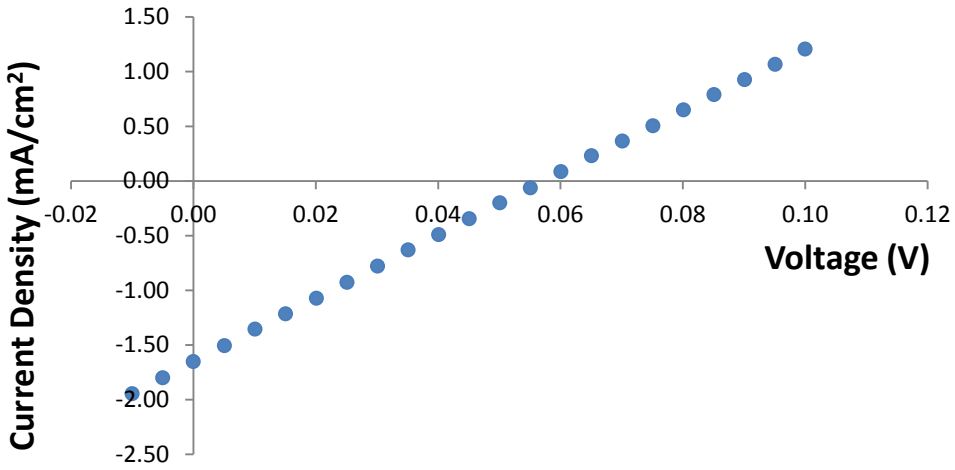

Figure 2.18: *Current vs Voltage (I-V) curve for an organic solar cell fabricated with a graphene-gold nanoparticle-graphene sandwich electrode.*

a graphene sandwich electrode, however, show greater than an order of magnitude increase in their short circuit current, compared to cells produced with single layer graphene. The open circuit voltage, however, suffers from the use of the graphene sandwich.

The source of the poor open circuit voltage is the subject of the next section.

2.7.4 AFM evidence for shorted devices

AFM studies of the graphene sandwich devices are performed to investigate the source of the low open circuit voltages in these devices. The results are shown in Figure 2.19. Simultaneous topography and current maps are obtained of the same area in a graphene sandwich-solar cell over a region without the lithium fluoride/aluminum top contact. A small voltage (0.5V) is used to obtain the current map. The topography map shows regions where the graphene has large folds that penetrate the organic solar cell film. In these same regions in the current map, we find that the current spikes. This explains the low open circuit voltage in these devices: large folds in the graphene act as shunts. The solar cell active layer is roughly 100nm thick. AFM studies of graphene sandwiches without the

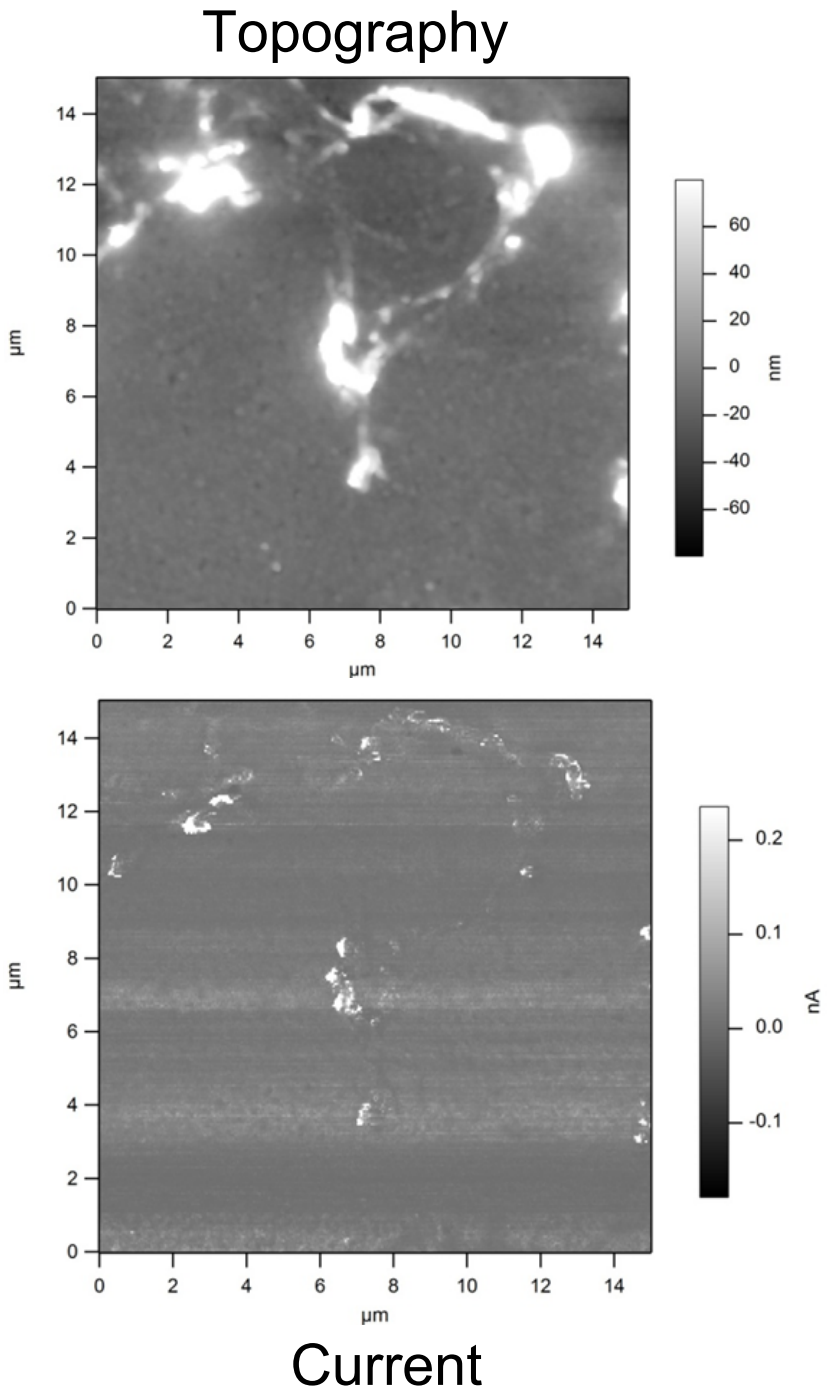

Figure 2.19: *AFM topography (top) and current map (bottom) of an organic solar cell built on a graphene and gold nanoparticle sandwich. The region scanned is an area without the top aluminum contact. These results show the reason for the poor open circuit voltages of the graphene sandwich cells. The folds in the graphene penetrate the active layer, as can be seen in the topography scan. In these locations, the current spikes, indicating that there is a low resistance path to the counter electrode. Thus, the devices are shorted by the graphene.*

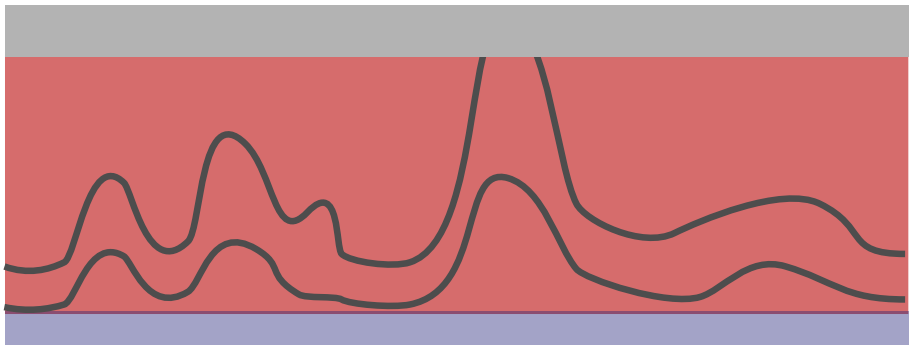

Figure 2.20: *Illustration of inner structure of solar cells built with the graphene sandwiches. Tall features of graphene reach the counter electrode, introducing shunts.*

organic photovoltaic layer show that these folds can regularly be greater than 100nm high. Thus, these folds could penetrate the active layer of the solar cell through to the opposite electrode. An illustration of the proposed inner structure of the graphene sandwich solar cells is shown in Figure 2.20.

Based on AFM studies of transfered graphene, two layers of CVD grown and PMMA transfered graphene produce more folds than single layers. This observation is true especially for graphene transfered using the hotplate-drying technique, discussed in section 2.3.1, although the vacuum drying technique is not sufficient to eliminate this problem. In conclusion, the combination of graphene sandwiches with solution processed solar cells is a difficult combination to fabricate.

2.8 Summary and Future Outlook

In conclusion, plasmonic graphene sandwiches have a number of interesting properties. The electronic properties include modified work function, and reduced sheet resistance compared to stacked double layer graphene. Furthermore, the sandwiches couple strongly to broadband light, in contrast with metal nanoparticles deposited on a single layer or without graphene. This could have important implications for optoelectronic applications requiring

Table 2.1: *Solar cell performance with graphene and gold nanoparticle electrodes and cell constructed on indium tin oxide for comparison.*

Electrode	Graphene	Graphene and Gold Nanoparticles	Graphene and Gold Nanoparticles Sandwich	Indium Tin Oxide
$V_{OC}(mV)$	200	280	50	510
$I_{SC}(mA/cm^2)$	0.028	0.032	1.27	1.9
Fill Factor	0.26	0.25	0.26	0.33

broadband performance, including solar cells.

The graphene and gold nanoparticle combination has proved to be a system with rich physics. One interesting future experiment would be to better characterize the strength of the local field enhancement of a gold nanoparticle in a graphene sandwich. For instance, mapping the local field enhancement shape and intensity in three dimensions could be a very interesting project. For this project, nanoscale scanning optical microscopy (NSOM) would be very useful.

The demonstration of graphene sandwiches as electrodes for solar cells would benefit from using a thin film, not solution processed solar cell material. For instance, the graphene sandwiches could be deposited on thin film copper indium gallium selinide (CIGS) solar cells. This would alleviate the shorting of the solar cells due to large folds in the graphene.

Chapter 3

Direct measurement of the built-in potential of a heterostructured nanorod

3.1 Background

In this work, we study heterostructured nanocrystals which are a candidate material for the active layer of solar cells. Nanocrystals have a number of advantages as a solar cell material. Geometric confinement of nanocrystals tunes the band gap, and so a nanocrystal based solar cell could be made which matches the solar spectrum. Further, nanocrystals are synthesized in solution, a substantially lower cost fabrication method than that which is used for solar cells based on thin films or wafers. However, in order to be a viable candidate as a solar cell material, the crystals would need to show a built-in potential across the length of the crystal. This is the subject of our study.

We measure the built-in potential across individual Cu_2S-CdS heterostructured nanorods using a combination of transmission electron microscopy and electrostatic force microscopy. This work, published in 2010 [87], represents the first experimental determination of the electrostatic potential across an isolated nanostructure. We observe a variation of potentials for different bi-component nanorods, ranging from 100 to 920 mV, with an average of 250 mV. Nanorods of a uniform composition with no heterojunction do not show a built-in potential, as expected. The results are particularly relevant for applications of colloidal nanocrystals in optoelectronic devices such as photovoltaics.

3.1.1 Overview of the experimental method and prior literature

The electronic structure of nanocrystals is an intriguing basic science topic and of great importance for applications. However, few experimental techniques exist to directly characterize on a nanometer scale the electronic properties of structurally well-characterized heterogeneous materials. In fact, one of the most important characteristics of a semiconductor-semiconductor interface, the built-in potential, which determines the suitability of the interface for charge rectifying applications such as photovoltaics, has not pre-

viously been directly measured for an isolated bi-component nanorod. As colloidally grown nanocrystals typically display a distribution of properties, single particle measurements are invaluable for observing individual differences[20]. In the bi-component cuprous sulfide - cadmium sulfide (Cu_2S-CdS) heterojunction nanorods examined in this work, there is significant variability in the relative fraction of the two materials among individual nanorods, even within a given batch. Ideally, one would like to correlate the internal chemical structure of the nanorod with an independent mapping of the electronic structure of the *same* nanorod.

We report such a correlation experiment here. We use high-resolution transmission electron microscopy (TEM) to characterize Cu_2S-CdS nanorods and then employ electrostatic force microscopy (EFM), an adaptation of atomic force microscopy (AFM), to determine the electrostatic potential gradient associated with the same nanorods. This is the first such application of EFM. EFM has previously been successfully employed to characterize semiconductors and nanomaterials including the charging of nanoscale systems [13, 40, 9], polarization in the tip-sample direction[10], and resolving surface potential distributions on thin films [35, 28]. Another technique for classifying nanomaterials, scanning tunneling spectroscopy, has been used to measure the band offsets of heterogeneous nanocrystals [3, 74, 73]. In this study we find that homogeneous, single-component nanorods with no heterojunction display no built-in potential, while bi-component nanorods have a built-in potential ranging from 100mV to 920mV. For comparison, a Cu_2S-CdS thin film has a built-in potential of 840 mV and exhibits photovoltaic behavior [76, 5]. Additionally, the polarity of the built-in voltage for all bi-component nanorods studied is consistent with a Cu_2S-CdS thin film, that is, the CdS side is negative and the Cu_2S side is positive. A historical review of thin film versions of Cu_2S-CdS solar cells is outlined in the next section.

3.1.2 Photovoltaic cells based on Cu_2S-CdS heterostructured thin films

Cadmium sulfide is an earth abundant semiconductor that was one of the first semiconductors characterized. In the most stable form, cadmium sulfide has a hexagonal wurtzite structure. It has a direct bandgap at 2.4 eV, which gives the semiconductor a yellowish hue. Cadmium sulfide has long been used as a pigment, and more recently, as a component of many different solar cell structures. Cadmium sulfide's direct band gap, earth abundance, and compatibility with other materials make it a popular choice for solar cell designs. Solar cells have been made with CdS -CdTe [22], $CuInSe_2$-CdS [34], and Cu_2S-CdS heterostructures. Because of cadmium's toxicity, care must be taken in manufacturing and disposal to avoid environmental contamination.

The photovoltaic effect in Cu_2S-CdS has been known since the 1954 discovery that a thin film of copper on cadmium sulfide acts as a solar cell [63]. This represented one of the first solar cells to be discovered. It has been speculated that the copper film partially converted the cadmium sulfide to form a thin cuprous sulfide layer, forming the cuprous sulfide-cadmium sulfide heterostructure.

Since then, various methods have been used to make the Cu_2S-CdS heterostructure, and many have relied upon conversion of CdS to Cu_2S. These heterostructures were a popular topic of study in the 1960s and 1970s [76, 5, 4]. They typically had the structure shown in figure 3.1. Cadmium sulfide absorbs most of the incident light, and acts as the

n-type material. A thin film of cuprous sulfide acts as the p-type material. Efficiencies greater than 9% were reported [4]. Open circuit voltages for these devices were typically around 0.5 V [4], despite the upper limit of 0.8 V based on the materials' energy levels, shown schematically in figure 3.2.

3.2 Experimental Methods

3.2.1 Synthesis of Nanorods

Cu_2S-CdS nanorods are synthesized using partial cation exchange to substitute Cu^+ for Cd^{2+} ions within CdS nanorods, as described in reference [65]. The exchange reaction leads to separate regions of Cu_2S and CdS connected by well-defined, epitaxial interfaces. The average fraction of Cu_2S depends on the number of Cu^+ cations added to the batch. The relative fraction of Cu_2S varies among individuals within a sample. Because of the nature of the wurtzite crystal structure, the growth of Cu_2S into the CdS nanorods via cation exchange preferentially occurs at the end facets leading to Cu_2S segments at one or both ends. Often, one end facet preferentially converts to Cu_2S, leading to asymmetric nanorods. This conversion is shown schematically in figure 3.3 The interface between the segments, though not apparent in figure , can be studied with high resolution TEM and is discussed in length in reference [65]. The nanorods used in this study have an average length of 29 ± 4 nm and an average diameter of 9 ± 4 nm; there is little change in the nanorod dimensions upon the partial transformation to Cu_2S. A high resolution TEM image of the Cu_2S-CdS synthesized nanorods is shown in figure 3.4. The nanorods for this work were synthesized by the Alivisatos group.

3.2.2 Combining TEM and AFM

Figure 3.5 a shows schematically the experimental sample measurement configuration. Fig. 3.4 shows TEM images for bi-component Cu_2S-CdS nanorods, and the inset shows a high-resolution image of a single nanorod heterostructure. The bi-component nature of this nanorod is dramatically evident, with contrasting lattice planes clearly defining

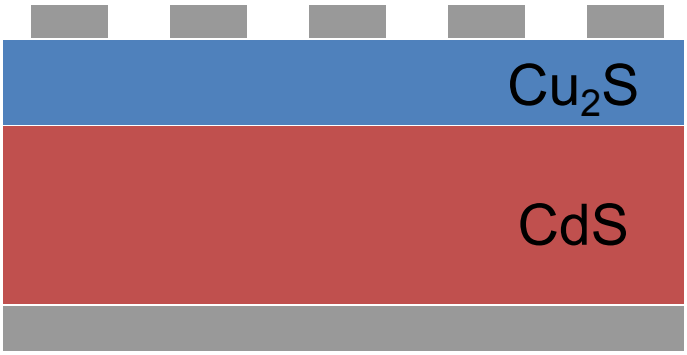

Figure 3.1: *Structure of* Cu_2S*-CdS thin film photovoltaic cells that were studied in the 1960s and 1970s. The same materials are studied in this work, but on the nanoscale.*

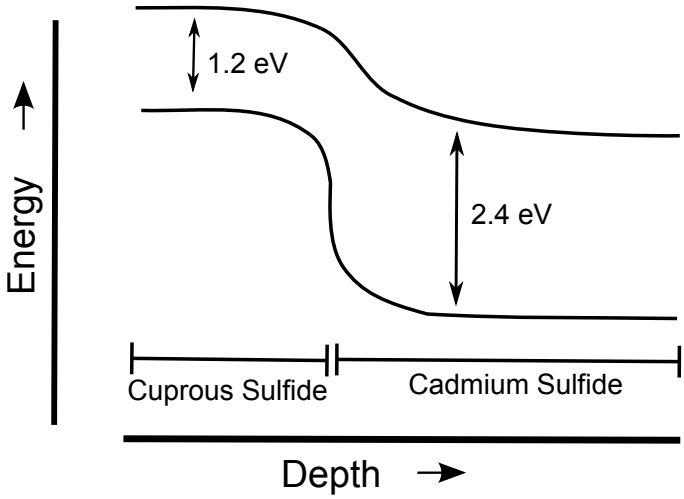

Figure 3.2: *Energy levels of cadmium sulfide and cuprous sulfide when forming a heterostructure. The difference between the valence band of the cuprous sulfide and the conduction band of the cadmium sulfide determines the voltage at which electrons can be extracted from the system. For these materials, with bandgaps of approximately 1.2 eV and 2.4eV, respectively, that voltage is approximately 0.8 V. The measured value of the built-in voltage in reference [5] is 0.85 V.*

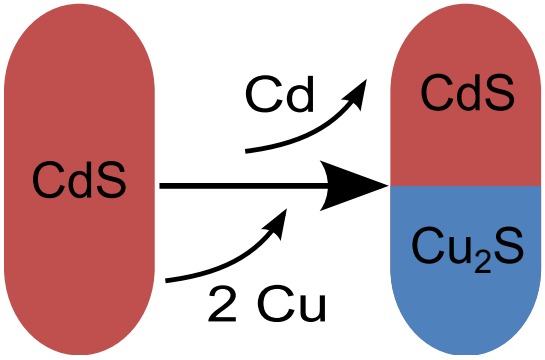

Figure 3.3: *The mechanism for producing* Cu_2S*-CdS heterostructured nanorods. Cadmium sulfide nanorods in solution are exposed to copper ions. The cadmium sulfide partially converts to cuprous sulfide, while the nanorod maintains its original size and shape. This exchange can occur preferentially at one of the facets of the nanorod, producing asymmetric heterostructured nanorods.*

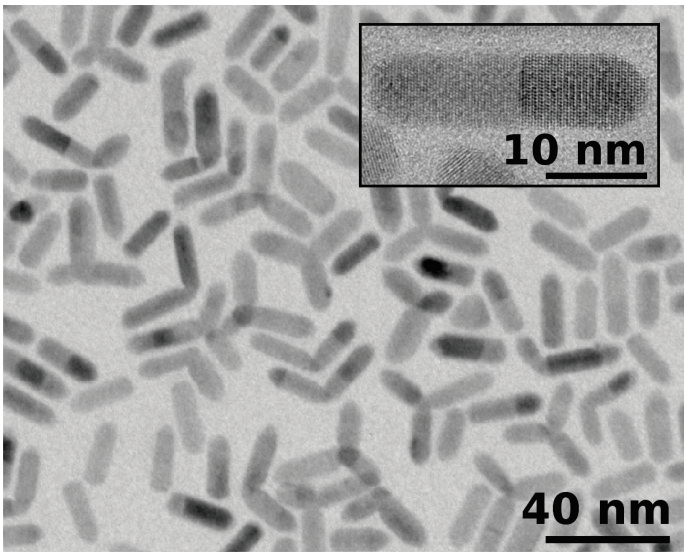

Figure 3.4: *High resolution TEM image of* CdS-Cu_2S *nanorods. Lattice planes of both materials are visible, and the two materials induce a contrast difference over the length of the rod. Note that not all rods display a heterojunction*

a heterojunction approximately halfway across the length of the rod. At lower resolution the bi-component nature of most of the nanorods is still evident, as shown by the TEM contrast differential across the nanorods in the main panel of Fig. 3.5. Importantly, not all of the rods examined display a heterojunciton.

Alignment marks on the sample substrate allow individual nanorods characterized by TEM to be subsequently located and characterized by AFM/EFM.

Fig. 3.6 shows an example of the dual-measurement and correlation method. The lower portion of the figure shows a TEM image of ion-exchanged Cu_2S-CdS nanorods, with the outer perimeters highlighted in red. In the upper portion of figure 3.6, similar TEM data exist, but only the perimeters of the nanorods have been drawn. The upper portion of Fig. 3.6 represents AFM topography data. Because of small thermal drift during the relatively slow AFM scan the AFM topography image is registered by an affine transformation using three landmark points.

The low-resolution AFM topography data shown in figure 3.6 serve only to register the AFM instrument to pre-determined nanorod locations. At specific locations of TEM-characterized nanorods, EFM data are collected. For EFM measurements, a conducting AFM tip is used to scan each line of the sample twice, first near the surface for topography, and then raised 20 nm above the surface with a bias dc voltage applied to the tip. During the raised scan, the electrostatic interaction between the sample and the tip causes a phase shift in the signal [66]:

$$\Delta\Theta = arcsin\left(\frac{Q}{k}\frac{\mathrm{d}F}{\mathrm{d}z}\right) \tag{3.1}$$

where Q is the quality factor of the cantilever, k is the spring constant, and dF/dz is the derivative of the force with respect to the tip-sample distance.

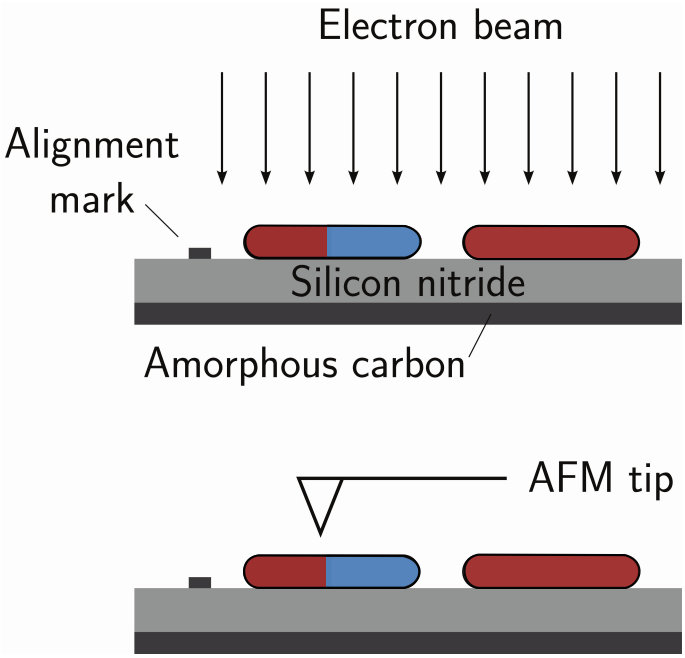

Figure 3.5: *a) A schematic of the experiment. The rods are examined in the TEM on an electron transparent silicon nitride window with a thin rear coating of conducting amorphous carbon. This substrate enables the same rods to be imaged with both the TEM for heterojunction identification and electrostatic force microscopy, which requires a conducting back plane.*

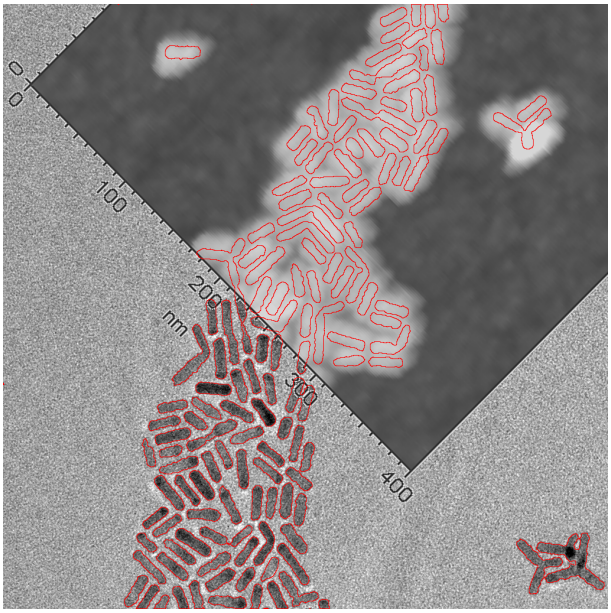

Figure 3.6: *AFM topography image (upper right) overlaid upon a TEM image of the same sample of CdS-*Cu_2S *nanorods. The red lines are outlines of the rods as determined by the TEM image. Each line in the AFM image is consecutively scanned for topography and electrostatic force microscopy (EFM) measurements. The topography scan data are used to determine the boundaries of the rods and the TEM data are used to determine the presence and orientation of a heterostructure for EFM analysis.*

The phase shift in equation 3.1 originates from modeling the AFM cantilever as a harmonic oscillator. This can be understood by considering the Taylor series of the force on the cantilever:

$$F(z + \delta z) \approx F(z) + (dF/dz)\delta z \tag{3.2}$$

The first term would have the effect of a constant displacement on a simple harmonic oscillator. The coefficient of δz in the second term would have the effect of changing the effective spring constant. Since the cantilever is driven at the original resonant frequency of the system, this term produces a phase shift of the cantilever response with respect to the driving force. It is this phase shift which is measured as the EFM signal.

3.3 Results and Analysis

3.3.1 Correlation of EFM data with TEM images

Fig. 3.7 shows, for three independent nanorods, the raw TEM image (upper row images) along with the TEM opacity, obtained by measuring the contrast level along a central axis line scan of the nanorod. The TEM opacity is shown in the second row of Fig. 3.7. The TEM images and opacity line scans clearly indicate a non-homogeneous nature to nanorods 1 and 2. The darker region (on the right side of nanorod 1, and on the left side of nanorod 2) is identified with Cu_2S, while the lighter region is identified with CdS [65]. Hence, nanorods 1 and 2 are bi-component nanorods (though apparently not with 50/50 composition distributions) with expected built-in electrostatic potentials. nanorod 3, on the other hand, has relatively uniform TEM contrast (even though it is a member of the ion-exchanged batch).

For each nanorod, the experimentally determined $\Delta\Theta$ EFM data yield the electrostatic potential difference, $\phi_{left} - \phi_{right}$, across the nanorod heterostructure. We caution that $\Delta\Theta$ and ϕ are related, but not trivially so. Due to the alignment of the Fermi levels at the interface between the two components in the bi-component Cu_2S-CdS nanorods, a space charge region is formed that induces a built-in voltage across the nanorods. Theoretical work has shown that on the scale of tens of nanometers, EFM resolution will be limited and the signal $\Delta\Theta$ does not emulate precisely the shape of the surface potential [69]. In fact, the measured force gradient arises from a convolution of forces in the tip-sample-substrate system. To correctly extract ϕ from the experimental data, three dimensional modeling must be employed. We do not quote a spatial resolution for our EFM measurements since at this scale the phase profile across the nanorod is more meaningful than the measurement at a single point. We demonstrate that we can use this phase profile to extract the built-in potential across the nanorods.

3.3.2 Electrostatic modeling of the nanorod - AFM tip system

To correlate the measured phase shift $\Delta\Theta$ profile with the built-in potential of the nanorods, $\phi_{left} - \phi_{right} = V_{bi}$, we generate a three dimensional finite element model with COMSOL. The AFM tip is modeled as a cone with a spherical apex with dimensions given by the manufacturer and is positioned above a single nanorod. We do not include the

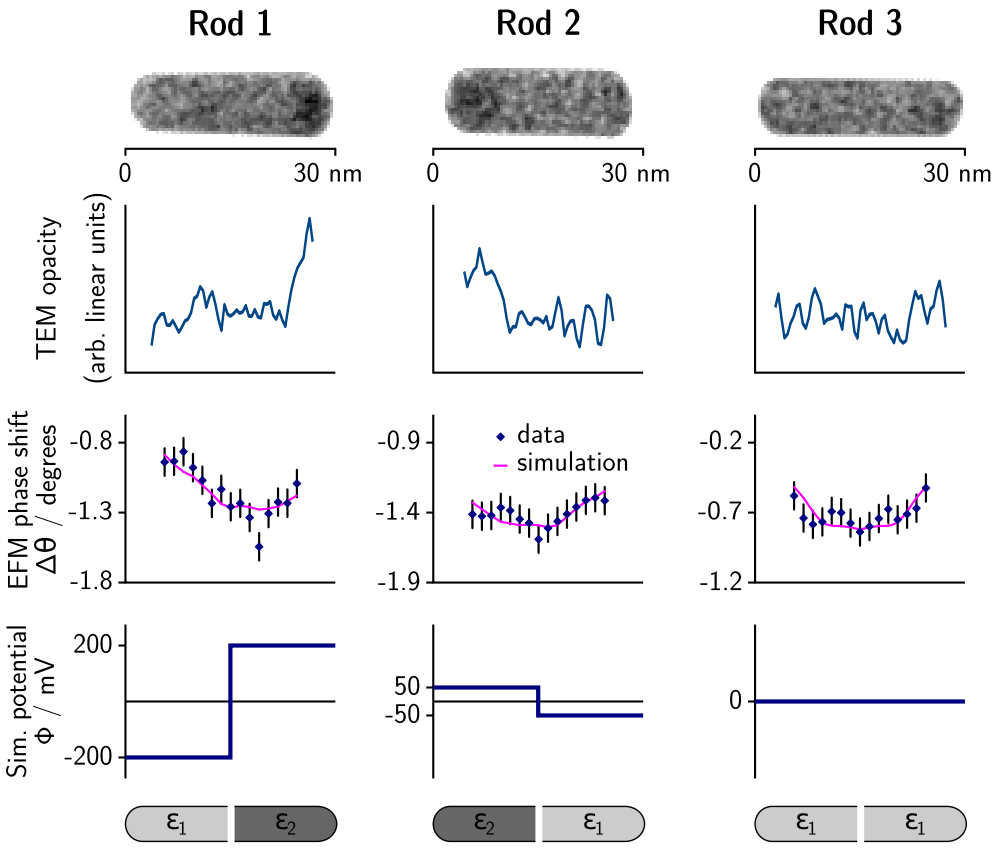

Figure 3.7: *Top: TEM images and opacity profiles of rods (1) and (2) which reveal a heterojunction and rod (3) which does not. Middle: EFM data (phase shift cross sections) which are asymmetric in rods (1) and (2) but not in (3). The lines through the EFM data are the results of a finite element electrostatic calculation modeling the tip/ CdS-Cu2S rod/substrate system. Bottom: In the model, the heterojunction is represented by strips held at* $-V_{bi,sim}/2$ *and* $V_{bi,sim}/2$*, and dielectric constants are set to the bulk values. For (1),* $V_{bi} = 400mV$ *and for (2),* $V_{bi} = 100mV$*. The symmetric rod (3) fits best to* $V_{bi} = 0$ *V with the same dielectric constant for each side.*

Table 3.1: *Statistical analysis of EFM data. Shown are the slope of the phase shift trend over the rod, normalized to the length of the rod, V_{bi} and the reduced χ^2 goodness of fit parameter for this V_{bi}. The first three rows present the results for rods (1) (2) and (3) shown in Figure 3.7. The fourth row gives the averages of the results for all rods. In the fifth row, all phase profiles are averaged before they are analyzed as a single data set. The last row shows the average results for the single material CdS control rods.*

	$\Delta\Theta/\Delta x$(mdegrees/nm)	Best V_{bi} fit	Reduced χ^2
Rod(1)	12	400mV	0.96
Rod(2)	9	100mV	0.5
Rod(3)	1.4	0mV	0.64
Averaged results	14±9	250mV	0.96
Averaged data for each position	15	100mV	1.4
Control CdS rods	3.2 ±2.8	0 mV	1.04

cantilever in the model, as it has been shown to have negligible influence on the phase shift profile [10]. The nanorod on the substrate surface is modeled as two separate, adjoining strips with dielectric constants ϵ_1 and ϵ_2 set to the bulk values for CdS and Cu_2S. The model strips are separated by a 1 nm gap and kept at $-V_{bi,sim}/2$ and $V_{bi,sim}/2$, respectively, where $V_{bi,sim}$ was varied from 0 to 1 V. The gap avoids divergence during computation and is expected to have negligible influence on the result . For simplicity, we model the two component sides as equal in length. We find that this approximation, which is obviously not precisely correct for nanorods 1 and 2, introduces only a modest deviation within an estimated range of ±100 mV in the determination of V_{bi}; the limited EFM resolution on this scale does not justify a more complex component distribution.

Table 3.2: *The number of rods associated with each V_{bi} interval, as determined by a χ^2 analysis of the fit of the measured phase profiles to the model. For three of the twenty nanorods, χ^2 values did not indicate a good fit.*

V_{bi}	Number of Rods
< 200 mV	10
200-400mV	2
400-600mV	2
600-920mV	3
Min χ^2 > 1.6(poor fit)	3

Using the model, the electrostatic force between the tip and the sample is calcu-

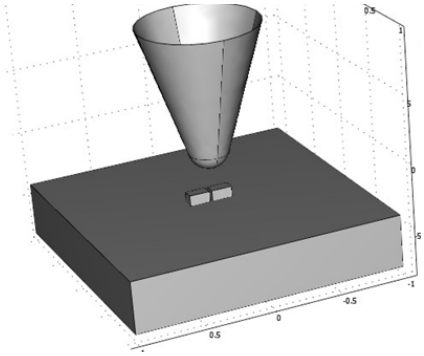

Figure 3.8: *The 3D geometry used in the COMSOL model to calculate the expected EFM response of the AFM tip.*

lated for a series of tip positions along the nanorod axis and at three different tip heights above the sample, at 19, 20, and 21 nm. To obtain the force gradient at each position along the nanorod, we used a finite difference approximation. With the forces from the three different tip heights we calculated two gradients, and ensured that they converge to better than 10%. Using the measured values for Q and k, and Eq. (3.1), we generated the expected phase shift.

Fig. 3.7 shows, in the third row, the experimentally determined EFM $\Delta\Theta$ data for nanorods 1, 2, and 3. The solid lines represent $\Delta\Theta$ as predicted by the model, for the ϕ and dielectric constant distributions shown in the fourth and last rows of Fig. 3.7. Interestingly, we find that nanorods 1 and 2 have different built-in potential magnitudes, 400mV and 100mV, respectively. As expected, the polarity of the built-in potential is correlated to the TEM determined structural composition. In contrast, nanorod 3, which has no TEM visible junction, fits best to a flat electrostatic potential.

3.3.3 Experimental validation of electrostatic modeling

To confirm the reliability of the modeling to extract V_{bi} from $\Delta\Theta$, checks are preformed on an idealized bi-component control nanorod consisting of a 40 nm wide and 30 nm thick gold line with a gap of 20 nm in the center. The line is drawn with electron beam lithography (NPGS) on a similar substrate as used for the nanorods. One side of the line is connected to a tunable voltage source, and the other side is connected to the tip. This allows us to control the potential difference across the structure. We then perform EFM measurements on this system, and verify that our model, adjusted to reflect the geometry of this control system, accurately reproduces the phase shift response to a known potential difference, equivalent to the built-in voltage in a nanorod. The EFM measurements of this system are shown in figure 3.9. As expected, the phase shift for the electrical pad that is

connected to the tip (on the left side of figure 3.9), is approximately zero, whereas the pad that has a voltage with respect to the tip has a phase shift of approximately 6 deg.

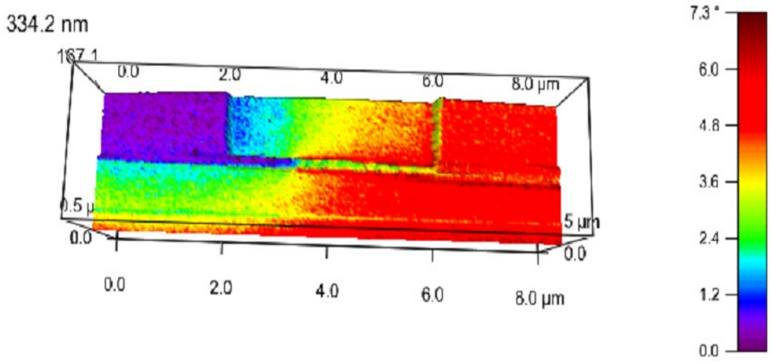

Figure 3.9: *EFM measurement of NPGS defined gold lines. The left and right sides are separated by a small gap (20nm). The left side is electrically connected to the tip, and the right side is connected to an external voltage. The color corresponds to the phase shift of the cantilever due to the electrostatic force. The height corresponds to the height of the surface. This system is modeled in a similar way as the nanorods, to verify that the model could accurately predict a known voltage difference on the nanoscale.*

3.3.4 Statistical analysis of nanorods

Additional nanorods are examined in a manner similar to that described for the three specimens in Fig. 3.7. EFM analysis of a control batch of 27 non-ion-exchanged CdS nanorods results in flat electrostatic potentials, i.e. $V_{bi} = 0$. TEM and EFM measurements are performed on 18 additional bi-component Cu_2S-CdS nanorod specimens which show a single junction in TEM analysis, and have random physical orientations. The results for these additional samples, together with those for nanorods 1, 2, and 3, and the control CdS set, are summarized in Table 3.1.

Table 3.1 shows that the phase gradient $d\phi/dx$ (and thus the built in potential) has the same polarity for all 20 bi-structure nanorods; using TEM opacity measurements, we determine that the phase gradient increases from the CdS side to the Cu_2S side. The average slope is 0.014°/nm with a standard deviation of 0.0097. For comparison, the average of the absolute value of the slope of a control batch of 27 pure CdS rods is 0.003°/nm, indicating that the measured gradients of the bi-component rods are within our measurement resolution.

The average built-in potential for the nanorods is $< V_{bi} >= 250$ mV. Excluded from this set are 3 nanorods which had poor fits to the model (reduced $\chi^2 > 1.6$). The phase profile trends for these rods are similar to the trend in all other rods, but the fits are poor because these nanorods include statistical variations that are larger than average. For normal statistical fluctuations, the probability of measuring 3 or more rods with a χ^2 value greater than 1.6 is 32%, given our sample size of 20. Thus, the presence of three

rods with a poor fit to the model is indicative of expected statistical variations. For the χ^2 analysis, we use the EFM error of 0.1°, based on measurements over the empty substrate. The average goodness of fit for this set is $< \chi^2 >= 0.96$, and the average χ^2 for all 20 rods is 1.1, indicating good consistency between the model and the experiment. We estimate the error of determining the built in voltage with our method to be ± 100 mV, an interval within which the χ^2 goodness of fit values do not clearly favor a specific value for V_{bi}.

In addition to analyzing individual rods, we also analyze the average phase profile of all nanorods, by aligning orientationally all 20 EFM profiles and averaging. Table 3.1 (fifth row) shows the results for this averaged profile, which compares well with taking the average of the individually fitted nanorods: the slopes are similar and V_{bi} is within the expected error margin.

Table 3.2 gives the distribution of built-in potentials associated with the nanorods. Ten of the twenty nanorods have a V_{bi} in the range 100 ± 100 mV, while seven have a larger V_{bi} of up to 920 mV. No nanorod has a potential greater than 920mV. The voltage variation within the set may arise from: the presence of different crystalline phases of Cu_2S (high chalcocite, low chalcocite or djuerlite); lattice plane orientation at the CdS-Cu_2S interface; or the presence of a small Cu_2S cap at the end of the CdS portion of the rod. Despite clearly identifying nanorods with a junction, the TEM images do not reveal these small variations that can cause the observed variability in the phase profile and the resulting built-in potential.

3.4 Summary and Outlook

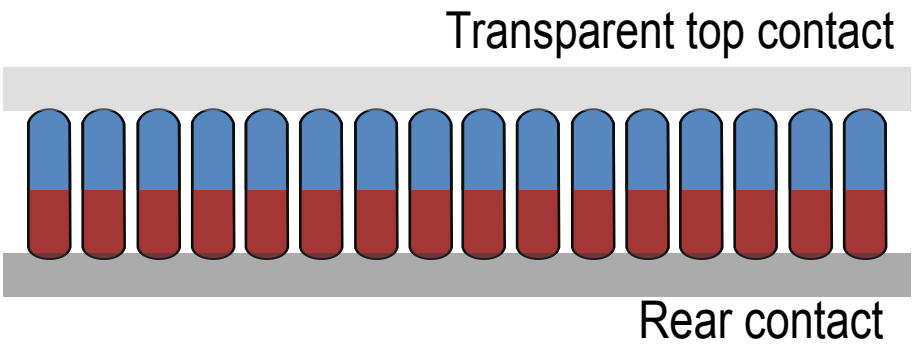

Figure 3.10: *Schematic of a solar cell based on* Cu_2S-*CdS heterostructured nanorods. The nanorods would be vertically aligned between a top transparent contact and a rear contact.*

In summary, we measured electrostatic potential gradients in nanorods, with a technique that is sensitive to the individual variability in the built-in potentials of the rods. Most rods examined showed a built-in potential in the range of 100 to 400mV, with some as high as 920mV ± 100mV, indicating that these rods show promise for applications such as photovoltaics. The characterization technique is generally useful to electronically quantify new nanostructured materials.

The substrate that we developed for this work, while unique at the time, could now in principle be replaced with a graphene-coated substrate or suspended graphene substrate.

Graphene is an excellent material for use as a TEM substrate[61]. Graphene would have the advantage of being more transparent to the electron beam, while having a greater conductivity than the amorphous carbon film, and would be a preferable alternative for future studies to the amorphous carbon film.

Since this work was published in 2010 [87], Cu_2S-CdS nanorods have continued to be a material of interest to the photovoltaics community. Photovoltaic cells produced with single Cu_2S-CdS core-shell nanowires were recently developed in the Peidong Yang lab [78]. The geometry of these devices is markedly different from the geometry of the nanorods studied in this experiment: these rods have long aspect ratios, and the shell of CdS is converted to Cu_2S. These devices were also produced using the cation exchange reaction. They had an energy conversion efficiency of up to 5.4%. Interestingly, V_{OC} values in the range of ~ 0.5 to $0.7V$ were reported. This range is consistent with the range of values measured for the nanorods in this work.

Future use of Cu_2S-CdS nanoscale rods or wires would likely consist of arrays of vertically-aligned structures, forming a forest of independent Cu_2S-CdS structures. Figure 3.10 schematically shows a solar cell design using vertically aligned nanorods. This geometry could result in increased light absorption compared to planar Cu_2S-CdS, due to light trapping within the forest. Some progress has been made on assembling nanorods into vertically aligned forests with areas of up to ~ 1 cm [2]. Further scaling of this technique is necessary before such devices could achieve commercialization. In addition to aligned rods, the Cu_2S and CdS orientation would need to be consistent from one rod to the next, so that the current flows in a single direction.

In order to take advantage of potential spectral mapping by rods of various diameters, multijunction solar cells would need to be fabricated. Such a cell could be made by stacking different sized nanorods. Lattice mis-match is a problem for conventionally produced multijunction cells, as various materials do not have the same lattice structure, and thus, produce strain on the layers. This would not be a problem for nanorod based multijunction cells.

Chapter 4

A one-step process for localized surface texturing and conductivity enhancement in organic solar cells

4.1 Background

Polymer based solar cells rely on a blend of semiconducting materials, such as Poly (3-hexylthiophene) (P3HT) and [6,6]-phenyl-C61 butyric acid methyl ester (PCBM). This combination, though promising, is handicapped by poor charge transport, which limits the thickness of the active layer, in turn reducing light absorption[11]. Of great interest, therefore, are methods by which the charge transport within organic solar cells can be improved, or, equally important, alternate methods by which light absorption can be independently enhanced. To this end, many different organic polymer-based blends have been explored[29] for enhanced charge transport. In addition, surface texturing, which effectively increases the path length of light through the active layer and thus enhances light absorption, has been applied to systems such as P3HT:PCBM via a soft-lithographic, master and stamp approach[53]. See section 1.3 for a more complete introduction to organic solar cells in general, and this blend in particular. This work was published in 2009 [88].

We here describe a method to enhance both charge transport, and light absorption via texturing, in an organic solar cell using a single post-production step. The step involves the local injection of electrical current into the surface of the device. Using small applied voltages and injection current density, the surface profile of the solar cell is unmodified but the local charge transport is significantly enhanced. Using higher applied voltages and injection current density, the local charge transport is again enhanced and the surface of the cell is advantageously textured.

4.1.1 Electrical measurements of organic solar cells with Atomic Force Microscopy

To avoid statistical fluctuations in the often inhomogeneous photoactive layers we have selected conductive atomic force microscopy (C-AFM) as the best tool for the

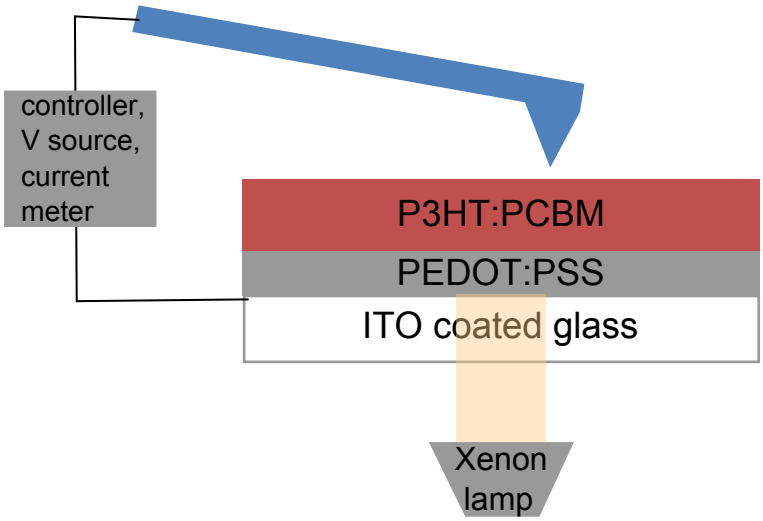

Figure 4.1: *The experimental setup. An organic solar cell, consisting of a P3HT:PCBM blend for the active layer, PEDOT:PSS as the electron blocking layer, and ITO coated glass as a transparent, conducting substrate. The device is illuminated from below with a xenon lamp for photoresponse measurements. A conducting AFM tip is used for topography scans, current mapping, local voltage applications, and local current-voltage measurements.*

application of modifications to, and the subsequent characterization of, the same microscopic area of an organic photovoltaic device. In related C-AFM studies of organic solar cell devices, contact mode has been used to spatially resolve currents, and non-contact mode electrostatic force microscopy (EFM) has been used to map electrostatic interactions with the surface [16] [59] [41][17][80][12]. Polymer films such as polystyrene[48], polymethylmethacrylate (PMMA)[47] and poly(3,4-ethylenedioxythiophene):poly(styrene sulfonate) (PEDOT:PSS)[15] have been shown to react to the proximity of a voltage-biased AFM tip by forming raised features. Unfortunately, in the case of PEDOT:PSS films, these features exhibit decreased conductivity[15].

4.2 Experiment Methods

4.2.1 Organic solar cell fabrication

The solar cells are fabricated in a manner similar to the method described in section 2.7.1, with slight modifications for the purpose of this experiment. In this experiment, solar cell devices are made by spin coating indium tin oxide (ITO) coated glass substrates with successive layers of PEDOT:PSS and P3HT:PCBM. The substrates are first cleaned by sonication in acetone and isopropyl alcohol, and dried on a hot plate. An aqueous solution of PEDOT:PSS is spun on at 3000 RPM and dried on a hotplate at 120C in air. The active layer solution is prepared in an argon atmosphere by dissolving regioregular P3HT (Rieke) in chlorobenze and letting it stir overnight. PCBM is added to make the active layer ratio 1:1 P3HT:PCBM at 1% wt. The layer is then spin coated onto the PEDOT:PSS layer at a

speed of 700 rpm, and annealed under argon at 140C.

4.2.2 AFM setup

An Asylum Research MFP-3D AFM is used in all measurements, with a platinum coated silicon probe (MikroMasch NSC 35 for non-contact and CSC 35 for contact mode images) in an Orca cantilever holder with a built-in current amplifier. The experimental setup is shown in figure 4.1.

All measurements are carried out in a dry argon atmosphere at room temperature and ambient pressure. Though the devices are fabricated and measured under inert argon, they are briefly exposed to the atmosphere during transfer between the glove box in which they are produced and the AFM flow cell.

4.3 Motivation of current injection with AFM tip

Figure 4.2 shows schematically the desired post-production cell processing. The top image shows the as-produced device morphology, prior to post-processing. In the center image, a small injection current density, applied via the C-AFM tip, has locally restructured the polymer blend thereby enhancing local transport characteristics of the film. The bottom image shows the device after a large injection current density has been applied; the polymer blend is locally restructured to improve transport, and, simultaneously, the rear surface has been textured for additional light-absorption capability. Rear surface texturing with a planar front surface has been shown to be effective at encouraging total internal reflection, and thus absorption, within the active layer [82].

4.4 Experimental Results

4.4.1 Local transport enhancement at low applied voltages

We first describe local transport enhancement without texturing in the PEDOT:PSS / P3HT:PCBM devices. Figure 4.3 shows contact mode topographic and current scans made with an applied probe bias of 30mV before and after scanning a 1 μm x 1μm area (indicated in red) at 500mV at the rate of 1 line /second. The results reveal an enhanced region of conductivity in the area that is in contact with the tip biased at 500mV, without significant change in the height profile. The response of the film to this voltage is not uniform, a result of the inhomogeneous nature of the film, composed of a blend of polymers with different thermal and electrical characteristics. As is evident in the figure, the conductivity modification has extended slightly beyond the region of the 500mV scan. This is likely due to film modifications occurring as a result of the probe voltages applied to map the current response of the extended area, and by longer-reach current path and electric field influences of the tip biased at 500mV.

4.4.2 Morphological and electrical modifications resulting from large voltage applications

Figure 4.4 shows the effects of film texturing by applying a large tip bias to a small film region. The area is scanned in AC (non-contact) mode before and after the application of a 10V bias pulse of 1 s duration with the AFM probe to the center of the scanning region. During the voltage application, and the subsequent current-voltage measurements, the tip

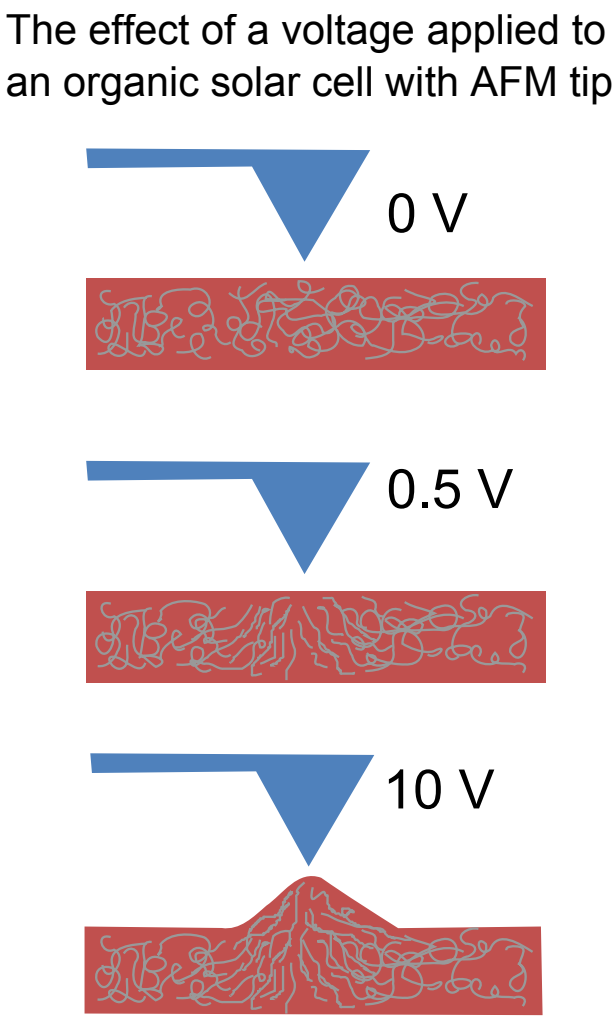

Figure 4.2: *The mechanism for the conductivity enhancement and feature formation by application of a voltage with the AFM tip. In the first case, the polymer strands are randomly tangled, without a particular orientation. After the application of a small voltage, the polymer strands immediately beneath the AFM tip orient with respect to the electric field, causing more efficient charge transfer in this area and increased conductivity in the vertical direction. In the third case, a large voltage is applied with the AFM tip and mass transfer to the site beneath the tip cause a large feature formation.*

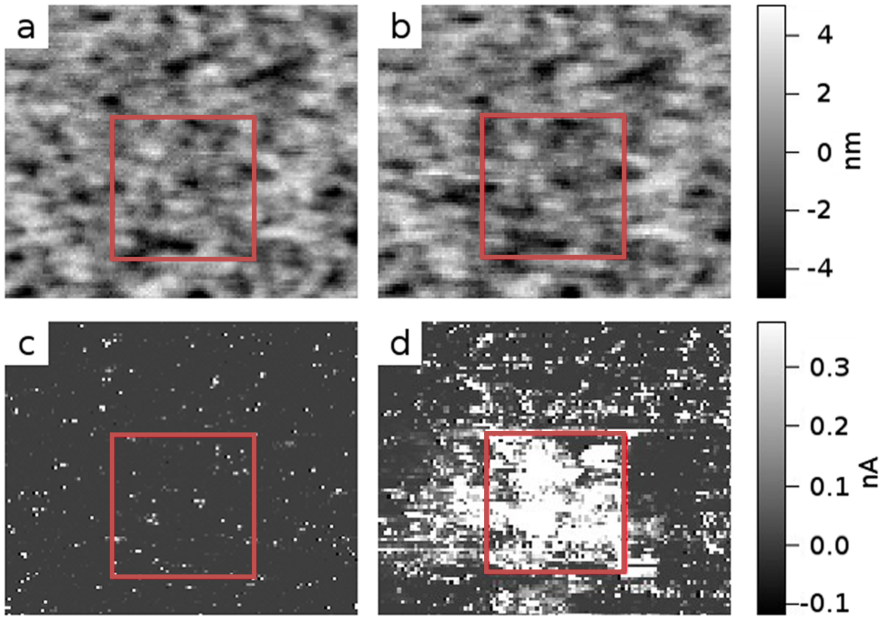

Figure 4.3: *The result of applying a 500mV voltage to the region in the red box to the topography and resistance of the film. The top two images (a and b) are topography scans and the bottom two images (c and d) are current scans. a and c are before the application of the voltage and b and d are after. For this voltage application, there is no visible change in the topography. However, the current scan reveals a lowering of the resistance of the film in the scanned area.*

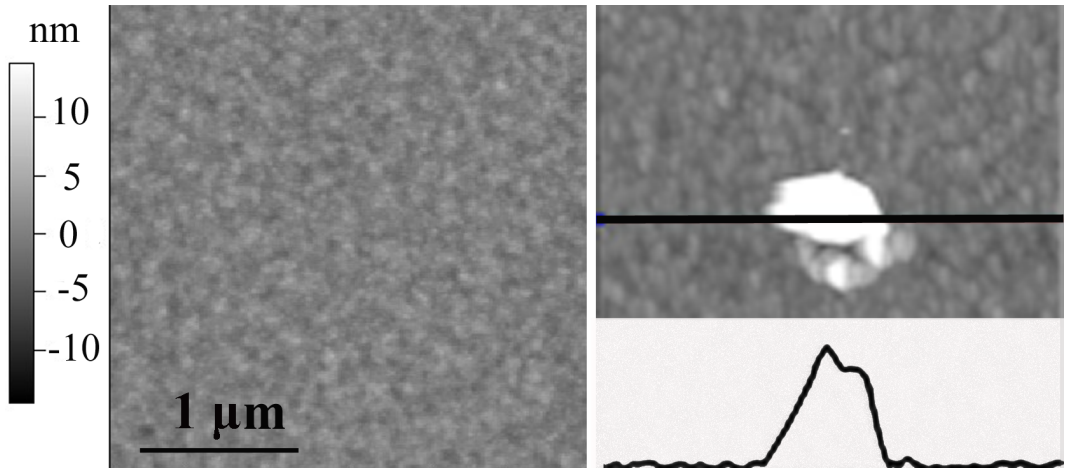

Figure 4.4: *Topographic map of the active layer of an organic solar cell device before (left) and after (right) forming a raised feature via a large voltage application with the AFM tip. The bottom right insert shows the height profile at the black line. The height of the feature is 60nm. In addition to modifying the surface topography, the application of the voltage modified the electronic properties of the film, as shown in figure 4.5*

is held stationary above the surface at a constant deflection in contact mode, i.e. the height of the tip remained constant with respect to the surface. The large applied bias results in the formation of an elevated feature with a height of 60 nm at the contact point and a diameter of 1μm.

In addition to modifying the surface geometry, the local application of a large conditioning voltage and injected current density improves the electrical characteristics of the layer. Figure 4.5 shows the current-voltage (I-V) characteristics of a raised spot in a PEDOT:PSS/P3HT:PCBM blend under dark and illuminated conditions before and after the application of the 10 V conditioning pulse. The probe voltage is increased linearly over 1 second from -1V to 1V for the current response measurements. A dramatic increase in film conductivity is observed, evident by a doubling of the short circuit current, from 7.6pA to 15 pA. The shape of the IV curve transforms from a linear curve, dominated by the series resistance of the device, to one with a more diode-like characteristic, suggesting a decrease in series resistance. The open circuit voltage shifted from 0.29 V to 0.33 V. This low value for Voc may be related to the non-ideal work function of platinum for this system. Normally, the electron extracting electrode would be of a lower work function material, such as aluminum, as discussed in section 2.7.1.

The surface-modification experiment has been repeated at different locations on the film, as well as on multiple films to confirm reproducibility. For the same film, the voltage required for feature formation is generally uniform, although some regions are found that required a higher or lower voltage, likely a result of the inhomogeneous nature of the bulk heterojunction.

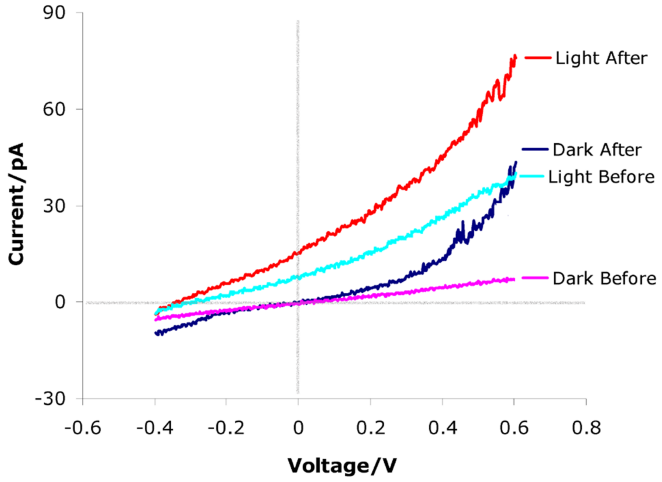

Figure 4.5: *Current vs voltage response of the spot from figure 4.4 in dark and illuminated conditions before and after feature formation. Note that after the film has been locally current-injection treated, it exhibited much higher conductivity than before. The open circuit voltage increases from 0.29V to 0.33 V, and the short circuit current doubles from 7.6 pA before to 15 pA after.*

4.5 Discussion of physical mechanism for polymer film restructuring

We briefly examine the mechanism of voltage-pulse induced transport enhancement and texturing in the devices. The small distance between the AFM tip and the conducting electrode beneath the polymer layers (100 nm), results in large fields (5x10^6 to 10^8 V/m) for an applied 0.5 to 10V. Furthermore, the sharp shape of the AFM tip results in large gradients in the electric field, and an electrostatic force on the surrounding area. While applying the voltage pulse, currents of $\geq$ 1 nA are typical, indicating a large current density in the area underneath the tip, making local heating above the glass transition temperature likely. The mobility of the polymer chains and PCBM molecules combined with the strong electric field under such conditions result in a significantly modified film morphology. Polarized polymer chains that align with the electric field are better aligned with each other and are more perpendicular to the substrate surface, providing more direct routes for the charge carriers to the electrode. The raised features are most likely due to mass transport towards the tip, occurring in tandem with polymer chain alignment.

We now check the above explanation with a calculation of the energy required to effect such a change in the polymer film. The total energy deposited into the film is:

$$U = Pt = \frac{V^2 t}{R} \tag{4.1}$$

So the local change in temperature of the film is:

$$\Delta T = \frac{\Delta U}{C} \tag{4.2}$$

Where C is the heat capacity of the polymer.

From the current measurements, the resistance of a column of polymer from the tip to the counter electrode is $\sim$ 3 x 10^{10} Ω. The voltage is applied at 0.5 V for 0.01 s. The heat capacity of the P3HT/PCBM blend is 0.5 J/gK [90]. With these inputs, the raise in temperature due to the local heating is $\sim$ 10 K. The glass transition temperature of the polymer blend is 40 C, and the melting temperature 200 to 300 C [90]. Thus, there is sufficient energy in the applied electrical current to warm the polymer film from room temperature to above the glass transition temperature, and enable the observed mass transport.

This physical explanation, of current induced heating which favorably reforms the local morphology, is consistent with the well established observation that the morphology of polymer based solar cells is critical to charge extraction[49]. Our results are also consistent with the observation that the post-treatment of solar cells with simultaneous annealing and applying an external electric field to a macroscopic device moderately increases charge extraction[57]. In the present case, the electric field gradients are much higher, given the geometry of the AFM tip, and we observe more significant gains in conductivity enhancement. Our technique also provides a valuable method for texturing the solar cell surface to enable better light absorption.

4.6 Summary and Future Outlook

We have observed significant morphological and electrical changes in response to large electric fields applied using an AFM tip in organic solar cell devices. This opens up new routes to better performance by combining surface texturing for improved light capturing with enhanced charge extraction capabilities of the photoactive polymer-fullerene blend. The scale-up of this technique could allow the improvement of macroscopic organic solar cell devices in the future. Though the concept of using a single AFM tip for the modification of a large solar cell is not practical, an array of sharp electrodes could be utilized for the treatment of large areas.

In addition to applications in organic solar cells, this technique could be used for direct-write nanolithography of organic circuits. More work should be done to characterize the use of an AFM tip for modifying various organic molecules.

Chapter 5

Star Shaped Carbon Microtubes

5.1 Background

In this section, we describe a discovery of a candidate quasicrystal, a microtube built of C_{60} with a five fold symmetric cross section, resembling a star. C_{60} is a large molecule formed of sp2 bonded carbon, and as such is related to carbon nanotubes and graphene. C_{60} has been used to form other micro structures, including thin whisker-like rods [77] and hexagonal tubes [32].

5.1.1 C_{60} structures

The C_{60} molecule is shown in figure 5.1. C_{60} is approximately 1 nm in diameter, and is shaped like a soccer ball. C_{60} is highly electronegative. C_{60} is usually synthesized via arc-discharge between graphite rods [14].

Crystals built of C_{60} can be the result of van der Waals bonding between the molecules. C_{60} crystals typically have a brownish appearance, and arrange in simple cubic

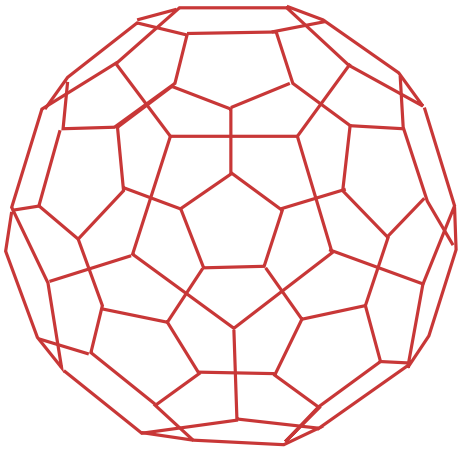

Figure 5.1: *The C_{60} molecule. A combination of 20 hexagons and 12 pentagons form the ball-like structure.*

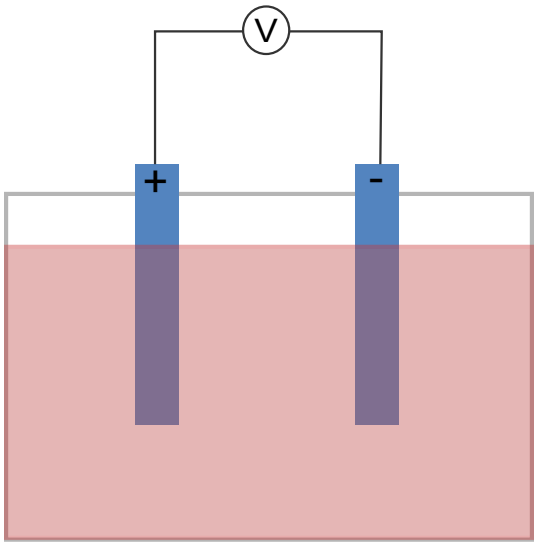

Figure 5.2: *A schematic of the experimental setup. Indium tin oxide coated glass are held 2.5 mm apart in a solution consisting of C_{60} dissolved in toluene and diluted with isopropanol alcohol. Voltages up to 200 V are applied between the electrodes.*

structure at low temperatures, and face centered cubic at temperatures above -20 C [14]. C_{60} crystals intercalated with alkali metals become superconducting at temperatures of up to 120K[8]. C_{60} molecules can also diamerize or polymerize. The polymerization of C_{60} is aided by oxidation, light exposure, and pressure [51].

5.2 Star-tube synthesis

5.2.1 Experimental setup

The star-shaped microtubes of this work are fabricated with electrophoretic deposition. A schematic of the setup is shown in figure 5.2. A Teflon trough is used in all experiments to hold the electrodes and solution. 1 mg of C_{60} is dissolved in 1 mL of toluene. Next, 10 mL of isopropanol alcohol is added to the solution. Indium tin oxide coated glass (16 mm x 14 mm) is used for the electrodes. The electrodes are then connected to a voltage source. Voltages of up to 200 V are applied between the electrodes for times ranging from one minute to two hours. When the samples are removed from the bath, a brown film is visible. The film coverage and opacity increases with deposition time.

5.2.2 Varying synthesis parameters

The yield of star microtubes is $\sim$ 5 %, estimated by SEM analysis. However, due to the small number of structures which are face-on, this number may be an underestimate, as only crystals which appeared to definitively be star rods are counted. This is the best yield obtained after optimizing the synthesis along the variables of temperature, light levels, deposition voltage, and concentration. The number yield of star tubes is not affected by

light levels, unlike some other forms of C_{60} based microstructures. The star tubes also grow on other conducting substrates. We use indium tin oxide coated glass for the optical contrast; on the ITO, the brown films of microstructures are more visible. The most star rods are observed for voltages of 160V.

To determine the necessity of a voltage for the formation of star rods, a solution with the same solvents and weight percentage of C_{60} which did not undergo electrophoretic deposition is dried using a rotovap. Crystals obtained from this solution include hollow six-sided tubes, filled rods, and shorter crystals. Less than 1 % of the crystals in this batch have a star-shaped cross section.

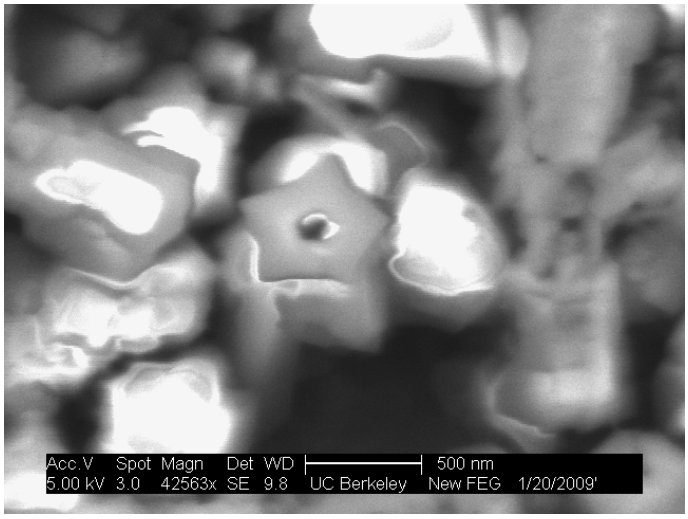

Figure 5.3: *Face-on SEM image of a star shaped microrod. The five pointed star is an unusual shape in microcrystals, as five-fold symmetric materials are extremely rare in nature.*

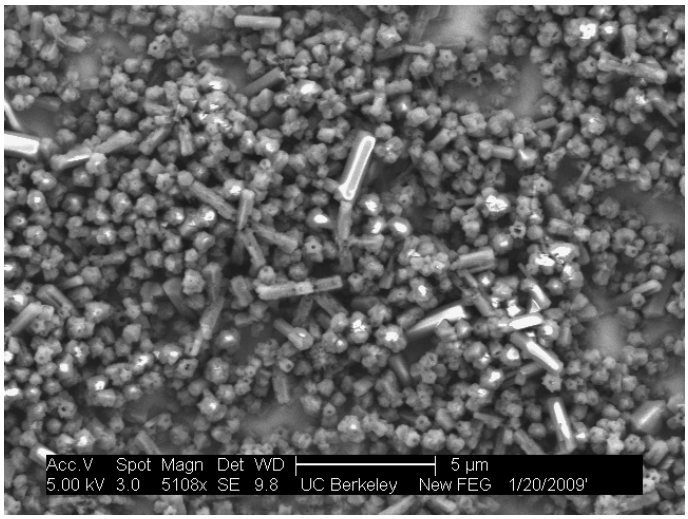

Figure 5.4: *A large area SEM scan of the C_{60} based microstructures.*

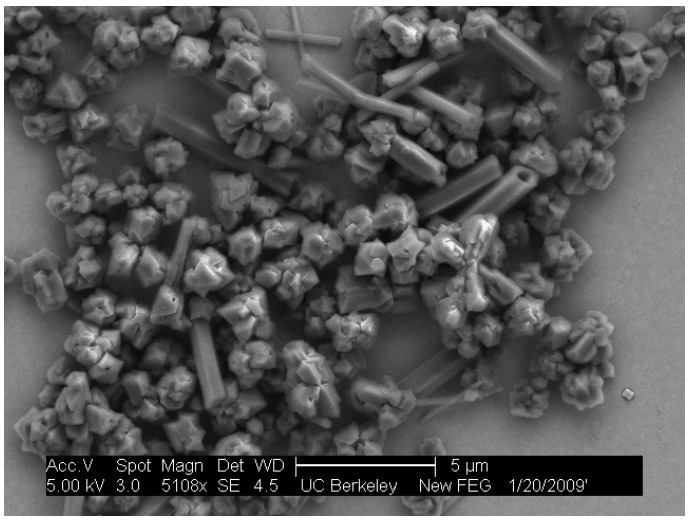

Figure 5.5: *A batch of C_{60} structures formed with the application of 200V. Various geometries are observed, including a small number of star-shaped structures.*

Figure 5.6: *Many of the microstructures had hexagonal geometries, such as the tube shown here. On the left side of the image, one can also see a star shaped structure.*

We observe that star shapes also form at lower applied voltages. In all of the samples, the cross sectional shape of the rods vary; however, with the higher voltages, more star tubes form, and a greater area of the electrode is covered for the same amount of time. Longer deposition times affect the area of the electrode covered, and the average length of the structures, but not the cross-sectional shape.

5.3 Characterization

Because of the low yield of star-shaped structures, we are unable to isolate the star tubes to perform diffraction to obtain the crystal structure. SEM imaging and Raman spectroscopy are used to characterize the shape, size, and composition of the tubes. Figure 5.3 shows an SEM image of a fabricated star rod as seen edge-on. The star tubes are $\sim$ 500 nm to 1 μm in width and are several microns to tens of microns long. They typically have a hollow center of $\sim$ 100 nm in diameter. A wider field of view image of a batch of C60 tubes is shown in figure 5.4. The tubes cover a large area of the sample, and have a variety of shapes. The edges of the tubes are faceted. The electron beam quickly charges the microtubes, indicating that the tubes are electrically insulating.

Raman spectroscopy, with a 488 nm laser, shows peaks at 1429 and 1529 cm^{-}1, which is consistent with the presence of C_{60} [51]. This result is difficult to interpret, however, due to the low yield of star tubes. To perform the measurements, the Raman laser is directed at a spot which is known from SEM imaging to have a high number of star tubes, but the star tubes are not isolated from other morphologies of C_{60} crystals.

5.4 Possible mechanisms for structure formation

The choice of solvents is crucial to the formation of the microstructures. Toluene and isopropanol alcohol, the solvents used in this study, are miscible solvents. However, C_{60} has very different solubility in toluene and isopropanol; C_{60} is highly soluble in toluene, and has a low solubility in isopropanol. Ethanol used in place of isopropanol resulted in structures with a hexagonal cross section,$\sim$ 1μm x 1μm, and the star shapes are not found.

Because of the large difference in the solubility of C_{60} in isopropanol alcohol and toluene, a large pressure at the interface between the two liquids may contribute to the microtube formation, as has been shown in the case of nanowhiskers fabricated from C_{60} in a blend of two solvents (carbon disulfide and isopropanol)[67]. That study showed that the pressure from the solubility difference polymerized the C_{60} molecules without the addition of UV light or other inputs. The crystal structure of the nanowires was determined to be triclinic. This study shares the high/low solubility feature of the solvents; thus, such a pressure could be at work here. We cannot determine if the star shaped microtubes consist of pristine or polymerized C_{60} , but we note that polymerization is a possibility in this system. The low yield of star shaped tubes could be a result of a very particular microenvironment that is necessary for the lattice formation.

5.4.1 Discussion of structure

The five-fold symmetric nature of these microrods is intriguing, since five-fold symmetric materials are rare in nature. Since a true crystal cannot be formed with five-fold lattice symmetry, such structures are called quasi-crystals. However, 10-fold symmetric C_{60} crystals discovered in the Zettl lab in 1992 [89] when analyzed were found to not be true quasi-crystals, and were composed of C_{60} and residual toluene. Furthermore, C_{60} crystal structures with various cross sectional shapes, including a five-sided prismatic shape, have been shown to have twinned crystal structures with domains of hexagonal close packed and face centered cubic structures[52]. Thus, the five-fold symmetric morphology of the microrods may be a result of a complicated, though not quasi-crystal structure.

Bibliography

[1] S. Bae, H. Kim, Y. Lee, X. Xu, J.-S. Park, Y. Zheng, J. Balakrishnan, T. Lei, H. R. Kim, Y. I. Song, Y.-J. Kim, K. S. Kim, B. zyilmaz, J.-H. Ahn, B. H. Hong, and S. Iijima. Roll-to-roll production of 30-inch graphene films for transparent electrodes. *Nature Nanotechnology*, 5:574578, 2010.

[2] J. L. Baker, A. Widmer-Cooper, M. F. Toney, P. L. Geissler, and A. P. Alivisatos. Device-scale perpendicular alignment of colloidal nanorods. *Nano Letters*, 10(1):195–201, 2010. PMID: 19961233.

[3] U. Banin, Y.W. Cao, D. Katz, and O. Millo. Identification of atomic-like states in InAs nanocrystal quantum dots. *Nature*, 400:542, 1999.

[4] J. A. Bragagnolo, A. M. Barnett, J. E. Phillips, R. B. Hall, A. Rothwarf, and J. D. Meakin. The design and fabrication of thin-film CdS/Cu_2S cells of 9.1 5-percent conversion efficiency. *IEEE Trans. on Electr. Dev.*, 27(4), 1980.

[5] H. W. Brandhorst. Technical Report D-5079, NASA, 1969.

[6] K. Branker, M.J.M. Pathak, and J.M. Pearce. A review of solar photovoltaic levelized cost of electricity. *Renewable and Sustainable Energy Reviews*, 15(9):4470 – 4482, 2011.

[7] L. Brey and H.A. Fertig. Electronic states of graphene nanoribbons. *Phys. Rev. B*, 73:235411, 2006.

[8] W. Buckel and R. Kleiner. *Superconductivity.* John Wiley and Sons, 2008.

[9] O. Cherniavskaya, L. Chen, M. A. Islam, and L. Brus. Photoionization of individual CdSe/CdS core/shell nanocrystals on silicon with 2-nm oxide depends on surface band bending. *Nano Lett.*, 3:497, 2003.

[10] O. Cherniavskaya, L. Chen, V. Weng, L. Yuditsky, and L. E. Brus. Quantitative noncontact electrostatic force imaging of nanocrystal polarizability. *J. Phys. Chem. B* ., 107:1525, 2003.

[11] K. M. Coakley and M. D. McGehee. Conjugated polymer photovoltaic cells. *Chem. Mater.*, 16:4533, 2004.

[12] D. C. Coffey, O. G. Reid, D. B. Rodovsky, G. P. Bartholomew, and D.S. Ginger. Mapping local photocurrents in polymer/fullerene solar cells with photoconductive atomic force microscopy. *Nano Lett.*, 7:738, 2007.

[13] R. Costi, G. Cohen, A. Salant, E. Rabani, and U. Banin. Electrostatic force microscopy study of single Au-CdSe hybrid nanodumbbells: Evidence for light induced charge separation. *Nano Lett.*, 9:2031, 2009.

[14] L. Dai. *Carbon Nanotechnology: Recent Developments in Chemistry, Physics, Materials.* Elsevier, 2006.

[15] X-D Dang, M. Dante, and T-Q Nguyen. Morphology and conductivity modification of poly(3,4-ethylenedioxythiophene):poly(styrene sulfonate) films induced by conductive atomic force microscopy measurements. *Appl. Phys. Lett.*, 93:241911, 2008.

[16] O. Douhret, L. Lutsen, A. Swinnen, M. Breselge, K. Vandewal, L. Goris, and J. Manca. Nanoscale electrical characterization of organic photovoltaic blends by conductive atomic force microscopy. *Appl. Phys. Lett.*, 89:032107, 2006.

[17] O. Douhret, A. Swinnen, S. Bertho, I. Haeldermans, J. D'Haen, M. D'Olieslaeger, D. Vanderzande, and J. V. Manca. *Prog. Photovoltaics Res. Appl.*, 15:713, 2007.

[18] M.S. Dresselhaus and G. Dresselhaus. Intercalation compounds of graphite. *Adv. Phys.*, 51:1–186, 2002.

[19] N. K. Emani, T.-F. Chung, X. Ni, A. V. Kildishev, Y. P. Chen, and A. Boltasseva. Electrically tunable damping of plasmonic resonances with graphene. *Nano Letters*, 12:5202, 2012.

[20] S. Empedocles and M. Bawendi. Spectroscopy of single CdSe nanocrystallites. *Accts. Chem. Res.*, 32:389, 1999.

[21] Z. Fang, Z. Liu, P. M. Wang, Y.and Ajayan, P. Nordlander, and N. J. Halas. Graphene-antenna sandwich photodetector. *Nano Letters*, 12(7):3808–3813, 2012.

[22] Z. Fang, X. C. Wang, H. C. Wu, and C. Z. Zhao. Achievements and challenges of CdS/CdTe solar cells. *International Journal of Photoenergy*, 2011.

[23] A.K. Geim and K.S. Novoselov. The rise of graphene. *Nature Materials*, 6:183, 2007.

[24] G. Giovannetti, P. A. Khomyakov, G. Brocks, V. M. Karpan, J. van den Brink, and P. J. Kelly. Doping graphene with metal contacts. *Phys. Rev. L.*, 101:026803, 2008.

[25] Shaojun Guo, Dan Wen, Yueming Zhai, Shaojun Dong, and Erkang Wang. Platinum nanoparticle ensemble-on-graphene hybrid nanosheet: One-pot, rapid synthesis, and used as new electrode material for electrochemical sensing. *ACS Nano*, 4:39593968, 2010.

[26] S. Gnes, H. Neugebauer, and N.S. Sariciftci. Conjugated polymer-based organic solar cells. *Chemical Reviews*, 107(4):1324–1338, 2007. PMID: 17428026.

[27] C. L. Haynes and R. P. Van Duyne. Nanosphere lithography: a versatile nanofabrication tool for studies of size-dependent nanoparticle optics. *The Journal of Physical Chemistry B*, 105(24):5599–5611, 2001.

[28] H. Hoppe, T. Glatzel, M. Niggemann, A. Hinsch, M. C. Lux-Steiner, and N. S. Sariciftci. Kelvin probe force microscopy study on conjugated polymer/fullerene bulk heterojunction organic solar cells. *Nano Lett.*, 5:269, 2005.

[29] H. Hoppe and N. S. Sariciftci. Organic solar cells: An overview. *J. Mater. Res.*, 19, 2004.

[30] C. N. Hoth, P. Schilinsky, S. A. Choulis, and C. J. Brabec. Printing highly efficient organic solar cells. *Nano Letters*, 8(9):2806–2813, 2008. PMID: 18683989.

[31] J. D. Jackson. *Classical Electrodynamics*. Wiley, 3rd edition, 1998.

[32] Heng-Xing Ji, Jin-Song Hu, Qing-Xin Tang, Wei-Guo Song, Chun-Ru Wang, Wen-Ping Hu, Li-Jun Wan, and Shuit-Tong Lee. Controllable preparation of submicrometer single-crystal C_{60} rods and tubes trough concentration depletion at the surfaces of seeds. *The Journal of Physical Chemistry C*, 111(28):10498–10502, 2007.

[33] Liwen Ji, Zhongkui Tan, Tevye Kuykendall, Eun Ji An, Yanbao Fu, Vincent Battaglia, and Yuegang Zhang. Multilayer nanoassembly of sn-nanopillar arrays sandwiched between graphene layers for high-capacity lithium storage. *Energy Environ. Sci*, 4:3611–3616, 2011.

[34] L. L. Kazmerski, F. R. White, and G. K. Morgan. Thin film $CuInSe_2$/CdS heterojunction solar cells. *Applied Physics Letters*, 1976.

[35] A. Kikukawa, S. Hosaka, and R. Imura. Silicon pn junction imaging and characterizations using sensitivity enhanced kelvin probe force microscopy. *Appl. Phys. Lett.*, 66:3510, 1995.

[36] K. Kim, W. Lee, Z.and Regan, C. Kisielowski, M. F. Crommie, and A. Zettl. Grain boundary mapping in polycrystalline graphene. *ACS Nano*, 5(3):2142–2146, 2011.

[37] R. R. King, D. C. Law, K. M. Edmondson, C. M. Fetzer, G. S. Kinsey, H. Yoon, R. A. Sherif, and N. H. Karam. 40% efficient metamorphic GaInP/GaInAs/Ge multijunction solar cells. *Applied Physics Letters*, 90(18):183516, 2007.

[38] M. Koshino. Interlayer screening effect in graphene multilayers with *aba* and *abc* stacking. *Phys. Rev. B*, 81:125304, Mar 2010.

[39] V. G. Kravets, F. Schedin, R. Jalil, L. Britnell, K. S. Novoselov, and A. N. Grigorenko. Surface hydrogenation and optics of a graphene sheet transferred onto a plasmonic nanoarray. *J. Phys. Chem. C*, 116:3882–3887, 2012.

[40] R. Krishnan, M. A. Hahn, Z. Yu, J. Silcox, P. M. Fauchet, and T. D. Krauss. Polarization surface-charge density of single semiconductor quantum rods. physical review letters. *Phys. Rev. Lett.*, 92:216803, 2004.

[41] B. J. Leever, M. F. Durstock, M. D. Irwin, A. W. Hains, T. J. Marks, L. S. C. Pingree, and M. C. Hersam. Spatially resolved photocurrent mapping of operating organic photovoltaic devices using atomic force photovoltaic microscopy. *Appl. Phys. Lett.*, 92:013302, 2008.

[42] G. Li, Y. Yao, H. Yang, V. Shrotriya, G. Yang, and Y. Yang. Solvent annealing effect in polymer solar cells based on poly(3-hexylthiophene) and methanofullerenes. *Adv. Funct. Mater*, 17:16361644, 2007.

[43] X. Li, W. Cai, J. An, S. Kim, J. Nah, D. Yang, R. Piner, A. Velamakanni, I. Jung, E. Tutuc, S. K. Banerjee, L. Colombo, and R. S. Ruoff. Large-area synthesis of high-quality and uniform graphene films on copper foils. *Science*, 324:1312–1314, 2009.

[44] X. Li, Y. Zhu, W. Cai, M. Borysiak, B. Han, D. Chen, R. D. Piner, L. Colombo, and R.S. Ruoff. Transfer of large-area graphene films for high-performance transparent conductive electrodes. *Nano Letters*, 9:4359–4363, 2009.

[45] H. Liu, Yunqi Liu, and Daoben Zhu. Chemical doping of graphene. *J. Mater. Chem.*, 21:3335–3345, 2011.

[46] A. Luque and S. Hegedus. *Handbook of Photovoltaic Science and Engineering.* John Wiley and Sons, Ltd., 2003.

[47] S. F. Lyuksyutov, P. B. Paramonov, S. Juhl, and R. A. Vaia. Amplitude-modulated electrostatic nanolithography in polymers based on atomic force microscopy. *Appl. Phys. Lett.*, 83:4405, 2003.

[48] S. F. Lyuksyutov, R. A. Vaia, P. B. Paramonov, S. Juhl, G. Sigalov L. Waterhouse, R. M. Ralich, and E. Sancaktar. Electrostatic nanolithography in polymers using atomic force microscopy. *Nat. Mater.*, 2:468, 2003.

[49] W. Ma, C. Yang, X. Gong, K. Lee, and A.J. Heeger. Thermally stable, efficient polymer solar cells with nanoscale control of the interpenetrating network morphology. *Advanced Functional Materials*, 15(10):1617–1622, 2005.

[50] S. A. Maie. *Plasmonics: Fundamentals and Applications.* Springer, 2007.

[51] N. Martn and F. Giacalone. *Fullerene Polymers: Synthesis, Properties and Applications.* John Wiley and Sons, 2009.

[52] B. Morosin, X.D. Xiang, M. Fuhrer, and A. Zettl. Structural properties of vapor-grown c60 crystals. *Applied Physics A*, 57:171–174, 1993.

[53] S.-I. Na, S.-S. Kim, S.-S. Kwon, J. Jo, J. Kim, T. Lee, and D.-Y. Kim. Surface relief gratings on poly(3-hexylthiophene) and fullerene blends for efficient organic solar cells. *Appl. Phys. Lett.*, 91, 2007.

[54] K. Nakada, M. Fujita, G. Dresselhaus, and M.S. Dresselhaus. Edge state in graphene ribbons: Nanometer size effect and edge shape dependence. *Phys. Rev. B*, 54(24):1795417961, 1996.

[55] Z. H. Ni, H. M. Wang, J. Kasim, H. M. Fan, T. Yu, Y. H. Wu, Y. P. Feng, and Z. X. Shen. Graphene thickness determination using reflection and contrast spectroscopy. *Nano Lett.*, 7(9):2758–2763, 2007.

[56] F. Padinger, C.J. Brabec, T. Fromherz, J.C. Hummelen, and N.S. Sariciftci. Fabrication of large area photovoltaic devices containing various blends of polymer and fullerene derivatives by using the doctor blade technique. *Opto-Electronics Review*, 8(4):280–283, 2000.

[57] F. Padinger, R.S. Rittberger, and N.S. Sariciftci. Effects of postproduction treatment on plastic solar cells. *Advanced Functional Materials*, 13(1):85–88, 2003.

[58] O. Pea-Rodrguez, P. Pablo Gonzlez Prez, and U. Pal. Mielab: A software tool to perform calculations on the scattering of electromagnetic waves by multilayered spheres. *International Journal of Spectroscopy*, 2011, 2011.

[59] L. S. C. Pingree, O. G. Reid, and D. S. Ginger. *Adv. Mater.*, 21:19, 2009.

[60] J. C Reed, Hai Zhu, A. Y. Zhu, C. Li, and E. Cubukcu. Graphene-enabled silver nanoantenna sensors. *Nano Letters*, 12(8):4090–4094, 2012.

[61] W. Regan, N. Alem, B. Aleman, C. Geng, B.and Girit, L. Maserati, F. Wang, M. Crommie, and A. Zettl. A direct transfer of layer-area graphene. *Applied Physics Letters*, 96(11):113102 –113102–3, mar 2010.

[62] Y. Ren, S. Chen, W. Cai, Y. Zhu, C. Zhu, and R. S. Ruoff. Controlling the electrical transport properties of graphene by in situ metal deposition. *Applied Physics Letters*, 97:053107, 2010.

[63] D. C. Reynolds, G. Leies, L. L. Antes, and R. E. Marburger. Photovoltaic effect in cadmium sulfide. *Physical Review*, 96(2):533–534, 1954.

[64] S. Sadewasser and T. Glatzel. *Kelvin Probe Force Microscopy.* Springer, 2011.

[65] B. Sadtler, D. O. Demchenko, H. Zheng, S. M. Hughes, M. G. Merkle, U. Dahmen, L.-W. Wang, and A. P. Alivisatos. Selective facet reactivity during cation exchange in cadmium sulfide nanorods. *J. Am. Chem. Soc.*, 131(14):5285, 2009.

[66] P. Samori. *Scanning Probe Microscopies Beyond Imaging.* Wiley-VCH, 2006.

[67] M. Sathish and K. Miyazawa. Synthesis and characterization of fullerene nanowhiskers by liquid-liquid interfacial precipitation: Influence of C_{60} solubility. *Molecules*, 17:3858–3865, 2012.

[68] S. E. Shaheen, R. Radspinner, N. Peyghambarian, and G. E. Jabbour. Fabrication of bulk heterojunction plastic solar cells by screen printing. *Applied Physics Letters*, 79(18):2996, 2001.

[69] Y. Shen, M. Lee, W. Lee, D. M. Barnett, P. M. Pinsky, and F. B. Prinz. A resolution study for electrostatic force microscopy on bimetallic samples using the boundary element method. *Nanotechnology*, 19:035710, 2008.

[70] Y. Shi, K. K. Kim, A. Reina, M. Hofmann, L.-J. Li, and J. Kong. Work function engineering of graphene electrode via chemical doping. *ACS Nano*, 4(5):2689–2694, 2010. PMID: 20433163.

[71] W. Shockley and H. J. Queisser. Detailed balance limit of efficiency of p-n junction solar cells. *Journal of Applied Physics*, 32(3), 1961.

[72] Y. Si and E. T. Samulski. Exfoliated graphene separated by platinum nanoparticles. *Chem. Mater.*, 20:6792–6797, 2008.

[73] D. Steiner, D. Dorfs, U. Banin, F. Della Sala, L. Manna, and O. Millo. Photoconductivity in aligned CdSe nanorod arrays. *Nano Lett.*, 8:2954, 2008.

[74] D. Steiner, T. Mokari, U. Banin, and O. Millo. Electronic structure of metal-semiconductor nanojunctions in gold CdSe nanodumbbells. *Phys. Rev. Lett.*, 95:056805, 2005.

[75] Ji Won Suk, Alexander Kitt, Carl W. Magnuson, Yufeng Hao, Samir Ahmed, Jinho An, Anna K. Swan, Bennett B. Goldberg, and Rodney S. Ruoff. Transfer of cvd-grown monolayer graphene onto arbitrary substrates. *ACS Nano*, 5(9):6916–6924, 2011.

[76] S. M. Sze. *Physics of Semiconductor Devices*. John Wiley and Sons, 1981.

[77] M. Tachibana, K. Kobayashi, T. Uchida, K. Kojima, M. Tanimura, and K. Miyazawa. Photo-assisted growth and polymerization of C_{60} nanowhiskers. *Chemical Physics Letters*, 374(34):279 – 285, 2003.

[78] J. Tang, Z. Huo, S. Brittman, H. Gao, and P. Yang. Solution-processed coreshell nanowires for efficient photovoltaic cells. *Nature Nanotechnology*, 6:568572, 2011.

[79] S. Tongay, T. Schumann, B.R.Appleton X.Miao, and A.F. Hebard. Tuning schottky diodes at the many-layer-graphene/semiconductor interface by doping. *Carbon*, 49:2033–2038, 2011.

[80] S. C. Veenstra, J. Loos, and J. M. Kroon. Nanoscale structure of solar cells based on pure conjugated polymer blends. *Prog. Photovoltaics Res. Appl.*, 15:727, 2007.

[81] G. Xu, J. Liu, Q. Wang, R. Hui, Z. Chen, V.A. Maroni, and J. Wu. Plasmonic graphene transparent conductors. *Advanced Optical Materials*, 24:OP71–OP76, 2012.

[82] E. Yablonovitch. Statistical ray optics. *J. Opt. Soc. Am.*, 72(7), 1982.

[83] Jong Min Yuk, Kwanpyo Kim, Benjamin Aleman, William Rega, Ji Hoon Ryu, Jungwon Park, Peter Ercius, Hyuck Mo Lee, A. Paul Alivisatos, Michael F. Crommie, Jeong Yong Lee, and Alex Zettl. Graphene veils and sandwiches. *Nano Lett*, 11:32903294, 2011.

[84] Y.W.Son, M.L.Cohen, and S. G. Louie. Energy gaps in graphene nanoribbons. *Phys. Rev. Lett.*, 97:216803, 2006.

[85] H. Zabel and S. A Solin. *Graphite Intercalation Compounds I.* Springer: Berlin, Germany, 1990.

[86] H. Zabel and S. A Solin. *Graphite Intercalation Compounds II.* Springer: Berlin, Germany, 1992.

[87] A. M. Zaniewski, M. Loster, B. Sadtler, A. P. Alivisatos, and A. Zettl. Direct measurement of the built-in potential in a nanoscale heterostructure. *Phys. Rev. B*, 82:155311, 2010.

[88] A. M. Zaniewski, M. Loster, and A. Zettl. A one-step process for localized surface texturing and conductivity enhancement in organic solar cells. *Applied Physics Letters*, 2009.

[89] A. Zettl. private communication, 2012.

[90] Jun Zhao, Ann Swinnen, Guy Van Assche, Jean Manca, Dirk Vanderzande, and Bruno Van Mele. Phase diagram of P3HT/PCBM blends and its implication for the stability of morphology. *The Journal of Physical Chemistry B*, 113(6):1587–1591, 2009. PMID: 19159197.

Appendix A

Atomic Force Microscopy with the Asylum MFP3D Instrument

This is a brief overview of using the Asylum MFP3D Atomic Force Microscope. Potential users should check with the superuser for training.

Before beginning, select a probe. A quick guide to probes is provided on the probe box. Make sure you are using a probe that is most appropriate to your experiment. Generally, conducting probes should be used for EFM, KPFM, c-AFM. Probes with a CoCr coating are for MFM experiments. Use low k values for contact mode. In most cases, for simple imaging, non-contact mode is best, with a cantilever such as NSC 35. Before using a new probe, try using an old one. Tips are generally robust, and by rinsing them in an acetone bath followed by an IPA bath, you can use an old tip without loss of resolution. Cantilevers cost at least $30/each

Load the tip into the tip holder by loosening the screw on the tip holder, aligning the cantilever to be parallel to the lines of the cantilever holder, and making sure the end of the cantilever is halfway between the cantilever holder and the top of the polished portion of the prism. Gently tighten the cantilever holder. Over tightening will strip the threads and make the cantilever holder unusable.

Load the tip holder onto the AFM head by pressing down the release button and snapping the tip holder into place, gently rocking the tip holder from front to back.

Next, load your sample onto a sample holder and hold it into place on the stage with magnets. Make sure the stage is not fully extended in the x or y direction. If the stage is fully extended, the AFM cannot scan, as during a scan it is actually the stage that moves.

Raise the AFM head to its highest position before placing it over the sample. The danger is that if the tip holder is too low, the cantilever can crash into the prism and scratch it; if this happens, the laser light that is used to track the cantilever position will be scattered. This will damage the microscope's ability to track the cantilever position, which every AFM experiment is based upon.

Turn on the laser, the lamp, and the monitor screen, and open MFP3D software. The software should recognize that the AFM is connected and the sum and deflection meter should appear. Align the laser on the probe by moving the laser in the x and y

directions with the LDX and LDY knobs. Once it looks like the laser is on the probe, look at the sum and deflection meter, and optimize the sum value. It should typically be 4.5-7 when optimized. Also, when the laser is on the probe, a small deflection in x or y should dramatically change the sum. If this is not the case, then the laser may actually be on the large part of the cantilever.

Zero the deflection with the deflection knob (PD). This centers the reflected laser light on the photodetector.

Find the resonant frequency of the cantilever by tuning. In the Master Panel window, switch to the Tune tab, set the target percent to -10% and the target amplitude to 1V. Auto tune.

Now it's time to find the surface! This is probably the hardest part for new users. Put the circular level on the AFM head and make sure the head is roughly level. Lower the head by turning the front and two rear legs in the direction opposite to the 'up' direction (that is, up is clockwise and down is counterclockwise). When lowering the head, do it slowly and watch the microscope focus and defVolts value to establish when you are close to the surface. As you approach the surface, withdraw the tip, lower the head slightly, engage, repeat. In other words: once you know you're close to the surface, do not bring the tip down to the surface manually, but let the AFM find the surface with the piezoelectric crystal. This also ensures that you will not crash the tip, and damage your probe, sample, and more importantly, the prism.

Now you can start your scan. Go to the Master Panel, and adjust the scan area, if desired. Start a scan with the Do Scan button.

Look at the red and blue lines below the live height scan. The red and blue lines should track; they represent the trace and retrace of a single line of the surface. If the red and blue lines do not track, try lowering the setpoint to 700 mV. If they still do not track, lower by 50 mV at a time. Also increase the Integral feedback value. You can raise this value until the cantilever begins to wildly oscillate- the oscillations will be noticeable in the height scan.

The same area will be scanned continuously until you select Last Scan or Stop.

To save images, select the checkbox save images and set the directory for your session.

To achieve better images, reduce the scan speed/rate and increase the scan lines and scan points.

When removing the head from the stage, always turn the tip holder up- withdrawing the tip is not sufficient

Remember: Before placing the head on the stage, turn the tip holder up to its highest position. Review the quick guide to probes before selecting a probe. Make sure you are using a probe that is most appropriate to your experiment. Don't losen the screw on the cantilever holder to the point where it may fall out. This screw is easy to lose and hard to replace!

Appendix B

Surface Potential Measurements

Section 1.5.2 introduced the theoretical background for using Kelvin probe force microscopy (KPFM) to measure the surface potential of samples. This section gives a detailed description of implementing KPFM.

Figure B.1 shows a schematic of the measurement set up for surface potential measurements with KPFM with the Asylum MFP3D AFM in the Zettl lab. The cantilever clip on the cantilever holder is electrically connected to the direct digital synthesizer(DDS), which can apply a voltage to the conducting cantilever. The measurement alternates between a topography scan and a KPFM scan. The KPFM scan makes use of the 'nap' scan feature, which uses the recorded height profile of the sample to maintain the tip at a fixed height above the sample. Thus, during the nap scan, deflections of the cantilever are assumed to be due to electrostatic forces between the cantilever and the surface, and the DDS generates a voltage to zero these forces. The potential image is the DC offset of the DDS, since this represents the contact potential difference between the cantilever and sample. PogoOut is the name given to the connection on the middle screw on the underside of the cantilever holder. A wire attached to this screw can be connected to the sample, for grounding or biasing the sample. The crosspoint panel can be opened in the software to monitor the use of PogoOut. The PogoOut ouput goes through an opamp and current buffer in the controller.

The deflection of the cantilever is monitored with the laser and photodiode. A DC bias is applied in addition to the AC voltage to zero the cantilever motion. Because of the nature of this technique, it will not work for insulating samples.

B.1 KPFM instructions

KFPM is a useful tool for mapping changes in the surface potential. If absolute work function values are needed, then the tip should be calibrated. A calibration can be done by performing a CPD measurement on a known surface, such as highly ordered pyrolytic graphite (HOPG).

Prepare the materials needed for a KPFM experiment: a conducting sample, a calibration material such as HOPG, a conducting probe (such as TiPt coated silicon), the flow cell, and a wire for connecting the sample to the cantilever holder.

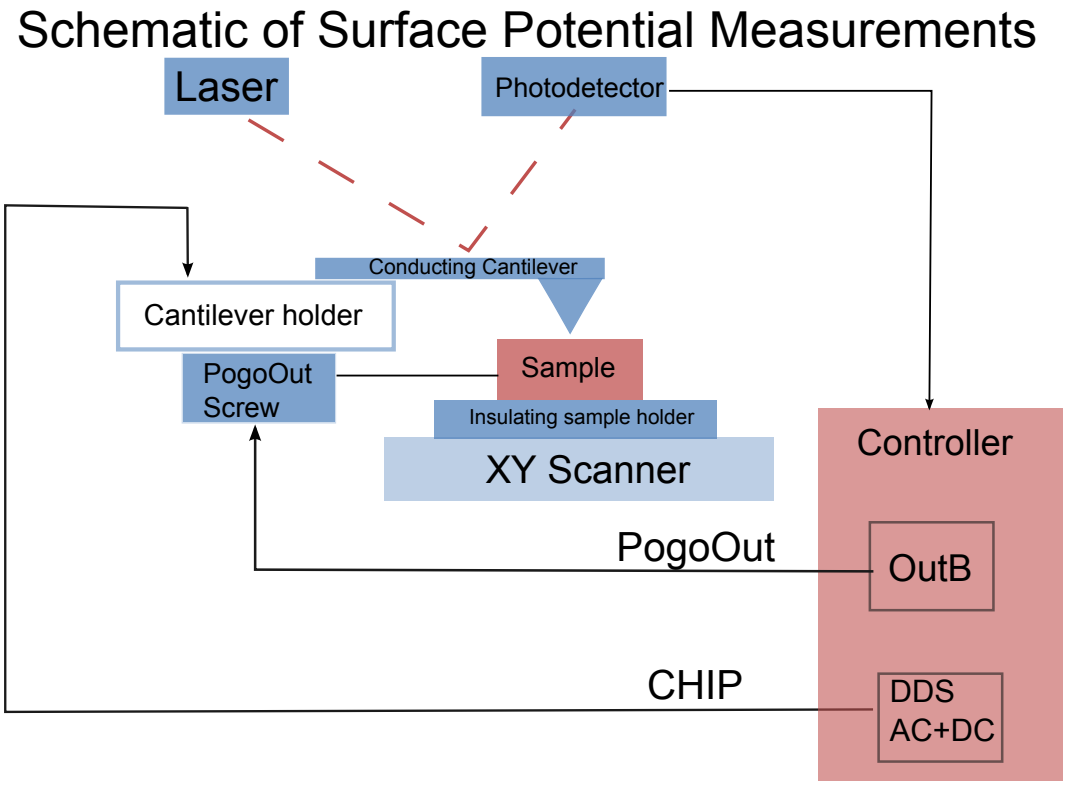

Figure B.1: *Schematic of the Asylum MFP3D setup for KPFM measurements.*

B.1.1 Flow cell

Contact potential difference measurements are more reliable when carried out in a dry atmosphere. Moisture in the atmosphere can cause a film of water to form on the surface. This will screen the true surface potential of the sample. For this reason, it is recommended to use an enclosed cell with flowing dry nitrogen. B219 has a nitrogen line that extends from the corner to the AFM setup, and includes moisture traps for this purpose. Attach the flow cell to the cantilever holder and load the sample on the bottom of the flow cell. Check the o-rings and tighten the screws for a secure fit.

B.1.2 Loading the cantilever

Load a conducting cantilever into the cantilever holder. Do not use the ORCA cantilever holder, because it does not connect to the CHIP line. The ORCA holder is designed for current mapping, and has an opamp built into the cantilever holder. This opamp on the ORCA holder is visible on the underside of the cantilever holder, so the two cantilever holders can be differentiated by looking for the opamp. Attach a wire to the PogoOut screw on the underside of the cantilever holder.

Load the cantilever holder onto the AFM. Launch the MFP3D software. By clicking on the blue swirl in the lower left corner, the software will scan the cantilever holder, and report the holder type, as a further check that the non-ORCA cantilever holder is being used.

B.1.3 Loading the sample

Load the sample using a mount that will allow for good electrical connection to the sample. If not using the flow cell, the black sample holder with the gold clips works well for this. The black coating is insulating. Clip the sample in place, and connect the gold clip to the PogoOut wire protruding from the cantilever holder.

When using the flow cell, attach a wire to the sample, and thread the wire out of the sides of the flow cell. Alternately, electrically connect the sample to the aluminum plate on the inside and attach a wire to the outside of the aluminum plate. Then attach to the PogoOut wire from the cantilever holder.

As per a normal scan, tune the cantilever with a 1 V target amplitude, set the target percent to -10% of the resonant frequency. In the main panel, set the imaging mode to AC mode and the set point to 800mV. Lower the AFM head, as per normal operation. Engage on the surface.

B.1.4 Electric Tuning

Open the electric tune panel, in the MFPcontrols menu, shown in figure B.2.

In the electric tune panel, do a force curve. Set the tip sample distance to 200nm. Set the trigger voltage to the same voltage used to engage the surface, usually 800mV. Next, click the arrow in the middle of the panel to copy the mechanical frequency to the electrically driven frequency. This is a good first guess for the tune. Do an electric tune of

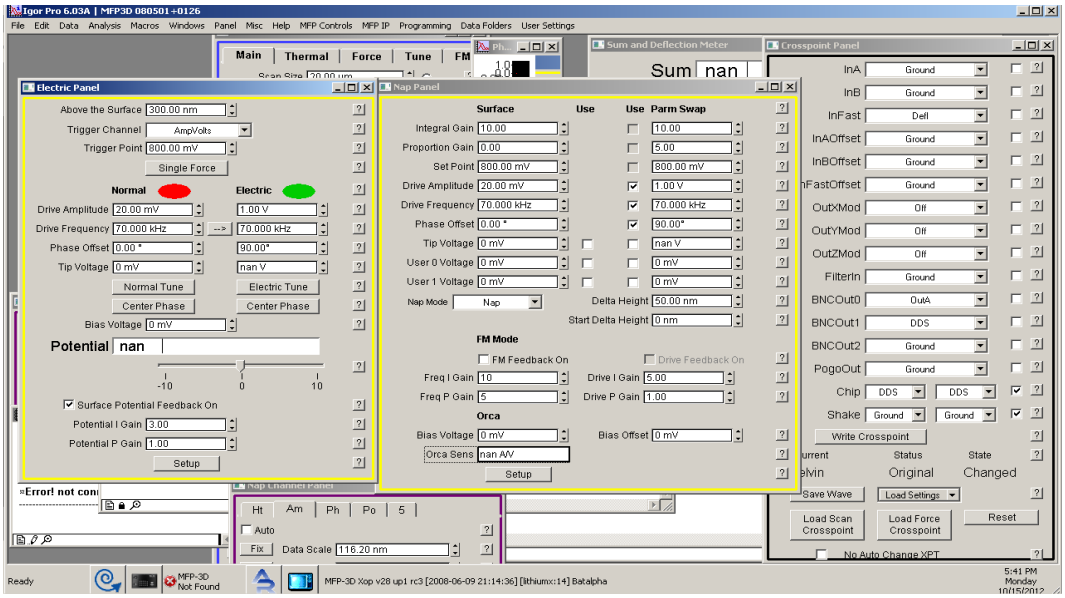

Figure B.2: *Screenshot of MFP3D software.*

the cantilever, with 1 V as the tip voltage and 1 V drive amplitude. The electrostatic tune frequency will be slightly higher than the mechanically tuned frequency.

Next, center the phase. The phase vs frequency graph will appear- check that it has a positive slope.

The surface potential feedback checkbox should be checked. The I gain should be in the range of 2-8.

If you wish to bias the sample, open the crosspoint panel under the Programming menu. Set the PogoOut to OutB and change the sample bias (bias voltage in the electric tune panel).

B.1.5 Imaging

In the master channel panel (one of the windows that automatically opens upon starting the program), there are the following tabs: Ht, Am, and Ph, 4, 5 standing for Height, Amplitude, and Phase, respectively. These represent the recorded channels of data. The tabs 4 and 5 represent blank channels. Click on tab 4, and select "Potential" from the drop down menu.

Next, the nap scan needs to be setup. Open the nap panel under the MFPControls menu. set the delta height: this can be as low as $\sim$ -10 nm, and up to 50 nm. This is the distance from the equilibrium distance of the tip when driven mechanically. Because the tip is driven electrostatically, values such as -10nm are possible without touching the surface. The distance does not change the value of the CPD signal, however, a too large distance may be the cause of no CPD signal.

As a check on the setup, you can vary the surface bias voltage (make sure that PogoOut is written to OutB in the crosspoint panel) and monitor the Potential data in

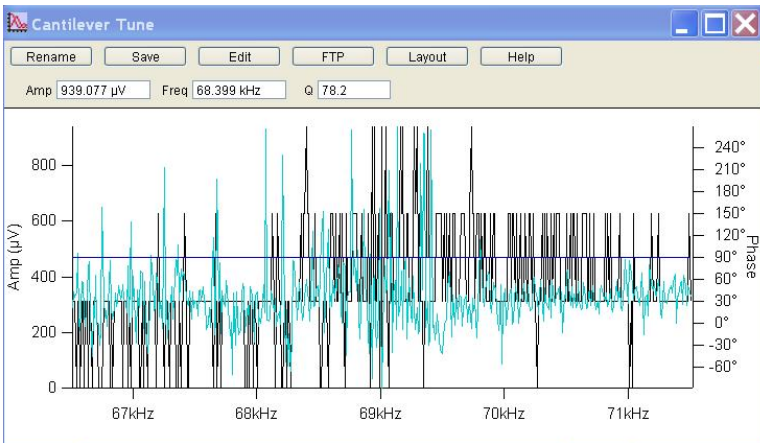

Figure B.3: *A noisy electric tune signal. The amplitude is the black line and the phase is the green line.*

the nap scan. In general for imaging, however, the sample should be grounded (PogoOut written to Ground in crosspoint panel).

In the nap panel, select the 'use' checkbox for the drive amplitude, phase offset, tip voltage, and drive frequency. In the drop down menu, select "Nap" for the nap mode.

Start a scan by clicking 'Do Scan'. The height, amplitude, phase and potential windows will pop up for both nap and the normal scan.

B.2 Troubleshooting

B.2.1 Noisy Electric Tune

Under normal circumstances, the electric tune should look similar to the mechanical tune. The amplitude signal should look like a Gaussian curve, and the phase signal should smoothly transition from the below the resonant frequency value to the above resonant value (typically a 90 degree shift). However, for beginning users, the electric tune often appears noisy, as in figure B.3. This can be due to the following issues:

1. The cantilever is not seated properly in the cantilever holder. Sometimes, a cantilever is sitting well enough in the holder for mechanical oscillation with the piezo driver, but is not well connected electrically. Repositioning the cantilever may help.

2. The tip is not close enough to the sample. Make sure that the probe is engaged. A lower setpoint will lower the tip closer to the sample, which may help.

3. The tip is touching the sample. Try raising the height above the surface setting.

4. The metal coating has worn off the tip. Try a new tip.

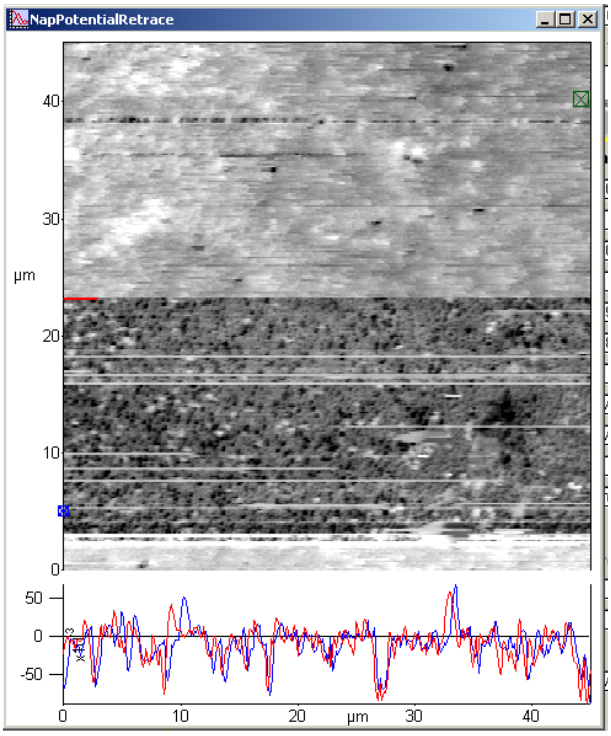

Figure B.4: *The potential signal from the nap scan of a graphene on silicon sample, showing a scan halfway finished. The top half is the new scan, and the bottom half is the old scan, of the same area. Though the scan is of the same area, the potential signal shows significant drift. The potential signal can sometimes drift from one measurement to the next due to tip contamination, wear, humidity fluctuations, and other effects.*

B.2.2 Potential Signal not Trustworthy

If the nap potential signal is noisy, not correlated with surface features, or has extremely low values for V, then the likely culprit is a bad connection between the probe and sample.

Large fluctuations in the measured surface potential can be due to tip wear, contamination, or humidity. An example of two consecutive scans with a drifting potential measurement is shown in figure B.4. Try the experiment in the flow cell with flowing dry nitrogen to reduce the effects of humidity.

To test the reliability of the measurements, you can measure an electrode with a variable external voltage. Then bias the sample with an external voltage supply or using the sample bias abilities of the instrument. Then do a KPFM scan and see if the nap potential tracks with the bias voltage on the sample.

As with height scans, the trace and retrace of the nap potential scan should track.

If there is still an issue with the potential tracking with the sample, try the following:

1. Try a new tip. The tip coating may be worn.
2. Lower the delta height in the nap panel.
3. Try adjusting the parameters in the electric tune window. In particular, raise the potential I gain.
4. Redo the electric tune, and be sure to center the phase. Check that the parameters in the electric tune panel correspond to the parameters in the nap window.
5. Check that the nap panel drive amplitude, drive frequency, and phase offset are selected to be used in the parameter swap for the nap scan.
6. You could also be wearing the sample. Try a larger scan size, and verify that the scanned area is not damaged.
7. Verify that you are not using the ORCA cantilever holder, which cannot be used for KPFM measurements.
8. Verify the connection from the sample to PogoOut is intact and continuous.
9. Open the crosspoint panel under the Programming menu. Check the crosspoint settings.
10. Consider the cleanliness of the sample. This can have a large effect on the surface potential, and be a source of contamination of the probe.

B.2.3 Further issues

The Asylum forum is a good resource for learning about KPFM and finding help for specific issues. It is located at support.asylumresearch.com/forum.

Appendix C

AFM Current Mapping

C.1 Background and Uses

Current mapping is a useful tool in atomic force microscopy. It was used in chapter 2 to spatially resolve currents from a solar cell built on a graphene electrode, and to diagnose the origin of shorting in that device. In chapter 4 the current mapping capabilities of the AFM was used for two purposes: controlled injection of current into an organic solar cell over single spots and larger areas, and mapping of the conductivity change of the film as a result of the current injection.

These experiments were carried out by using a conductive AFM probe to apply a bias to the sample, and measure the resulting currents. Hereafter, this technique will be referred to as c-AFM.

Figure C.1 shows schematically the c-AFM setup. The controller is used to apply a bias between the tip and the sample. Both the probe and the sample must be conducting. This schematic is simplified. Elements not shown here have the same set-up as in figure B.1.

c-AFM can be used for both mapping the current at a given voltage, and measuring the current for a voltage sweep, for instance, when performing I-V measurements. Current measurements can be made over a single point or over a larger area.

C.2 Experimental Steps

To make c-AFM measurements, you need to use the ORCA cantilever holder. This cantilever holder has a built-in preamp which enables measurements of picoamps of current. The op-amp is visible on the backside of the cantilever holder. The ORCA can also be identified using the MFP3D controller to perform a hardware scan. To do this, load the cantilever holder into the AFM. Click the blue spiral button in the bottom left corner of the software window (you do not need to load the tip first). Open the Do- IV panel, and look for the ORCA sensitivity. NaN will indicate that you are not using the ORCA holder.

Once you are confident that you have located the ORCA cantilever holder, remove it from the AFM. Attach a wire to the PogoOut screw on the underside of the cantilever holder. At this point, load the conductive cantilever. Then, attach the other end of the

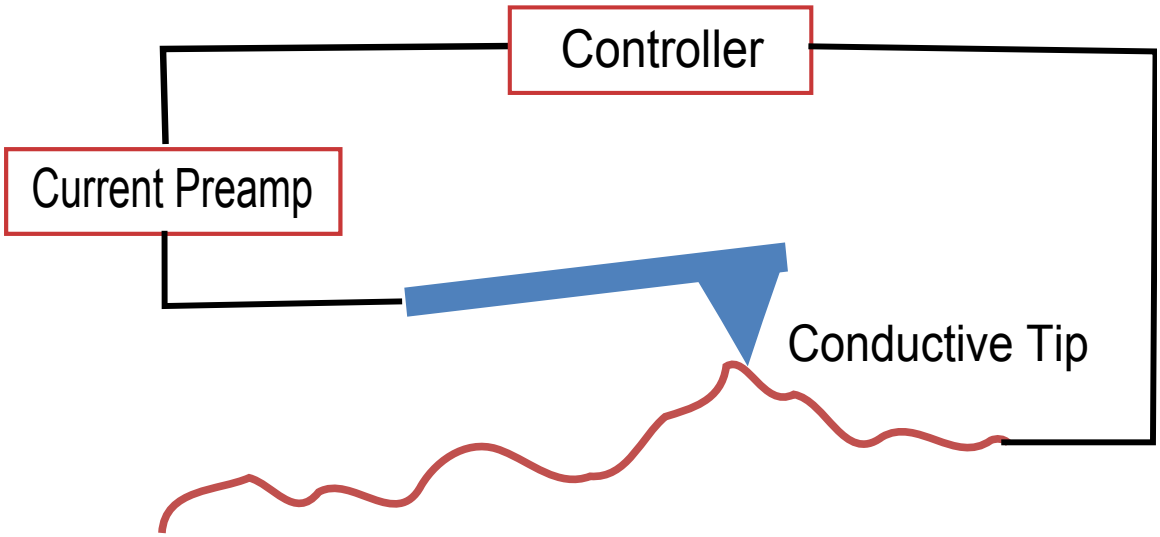

Figure C.1: Schematic of conducting atomic force microscopy. A conducting tip is scanned across a sample. The controller is used to apply a bias between the sample and the tip. A current pre-amp enables the measurement of picoamps of current.

wire to the sample. An easy way of doing this is to utilize the black cantilever holder with gold coated magnetic block connectors and gold coated clips. Attach the clip to the sample and wire the clip to the magnetic block. Attach the PogoOut wire to the magnetic block.

Tune the cantilever and approach the sample as you would for normal imaging. Do an AC scan of the surface to verify that the surface is clean and relatively flat. The current scan will be in contact mode, but doing an AC scan first will allow you to limit tip damage and contamination by avoiding large debris.

Next, set the imaging type to Contact in the Master Panel. In the Channel Panel, select current as a channel type. Open the nap panel (under MFP controls).

Begin imaging. Adjust the ORCA bias in the nap panel, and monitor the current in the current channel. You can adjust the bias mid-scan as required. The contact force has a large impact on the current measurement. Adjust the contact force by slosly increasing the tip deflection until the current levels off. At this point, the contact resistance is negligible. The necessary contact force will depend on the spring constant of the cantilever. If the spring constant is high ($\sim$ 50 N/m), use a small deflection, such as .1V. If the spring constant is low ($\sim$ .1N/m) use a larger deflection, such as 1V.

I-V measurements can be performed in the Do I-V panel. More information on this process can be found in Asylum's technical note on Conductive AFM.

C.3 Troubleshooting

If repeatability or artifacts are an issue with c-AFM scans, check the following:

1. Humidity. Humidity in the air can cause a water film to develop on the surface of the sample. A water meniscus can form between the tip and sample, altering the conduc-

tivity. To overcome this issue, c-AFM can be carried out in the fluid cell for a controlled atmospheric environment.

2. Tip damage. Metal coated tips are not very durable, and the metal coating may wear off.

3. Tip contamination. Debris on the surface can be picked up by the tip. For instance, polymer residue picked up by the tip will reduce the conductivity.

4. Contact resistance. Large features in a sample will cause drift in the sample-tip distance, resulting in variable contact resistance. Slowing the scan rate will allow for better tracking of the surface.

5. Surface modification. As in chapter 4, applying sample-tip voltages can alter the sample. Check a larger scan size to verify that the sample is uniform across scanned and unscanned regions.

6. Verify that the sample is well connected to the PogoOut wire. For instance, when scanning on a silicon substrate, the surface oxide will need to be etched or scratched away to achieve good contact with the wafer. A drop of silver paint on the sample will add a good contact area for the sample clip.